Arctic Sea Ice Classification and Soil Moisture Estimation Using Microwave Sensors

David Brian Lindell

A thesis submitted to the faculty of
Brigham Young University
in partial fulfillment of the requirements for the degree of

Master of Science

David G. Long, Chair
Brian A. Mazzeo
Wood Chiang

Department of Electrical and Computer Engineering

Brigham Young University

February 2016

ABSTRACT

Arctic Sea Ice Classification and Soil Moisture Estimation
Using Microwave Sensors

David Brian Lindell
Department of Electrical and Computer Engineering, BYU
Master of Science

Spaceborne microwave sensors are capable of estimating various properties of many geophysical phenomena, including the age and extent of Arctic sea ice and the relative soil moisture over land. The measurement and classification of such geophysical phenomena are used to refine climate models, localize and predict drought, and better understand the water cycle. Data from the active Ku-band scatterometers, the Quick Scatterometer (QuikSCAT), and the Oceansat-2 Scatterometer (OSCAT), are here used to classify areas of first-year and multiyear Arctic sea ice using a temporally adaptive threshold on reported radar backscatter values. The result is a 15-year data record of daily ice classification images. An additional ice age data record is produced using the C-band Advanced Scatterometer (ASCAT) and the Special Sensor Microwave Imager Sounder (SSMIS) with an alternate classification methodology based on Bayesian decision theory. The ASCAT/SSMIS classification methodology results in a record which is generally consistent with the QuikSCAT and OSCAT classifications, which conclude in 2014. With multiple ASCAT and SSMIS sensors still operational, the ASCAT/SSMIS ice classifications can continue to be produced into the future. In addition to ice classification, ASCAT is used to estimate the relative surface soil moisture at high-resolution (4.45×4.45 km per pixel). The soil moisture estimates are obtained using enhanced resolution image reconstruction techniques and an altered version of the Water Retrieval Package (WARP) algorithm. The high-resolution soil moisture estimates are shown to agree well with the existing lower resolution WARP products while also revealing finer details.

Keywords: QuikSCAT, ASCAT, OSCAT, sea ice classification, Arctic, microwave remote sensing, soil moisture

ACKNOWLEDGMENTS

Many thanks to my wife, Becca, for her patience, support, and love. I am also grateful to my advisor, Dr. Long, for his excellent mentorship and many wonderful puns. Without his guidance, this thesis would not be quite as long.

Table of Contents

List of Tables

List of Figures

Chapter 1

Introduction

Satellite microwave sensors can be used to measure or estimate many geophysical properties, including properties of sea ice and soil moisture [1, 2, 3]. Classification of Arctic sea ice type is of particular interest to climate researchers because of the insular properties of Arctic ice and its effect on ocean currents and dynamics [4]. Estimates of soil moisture using satellite microwave sensors can help to improve understanding of the water cycle, aid in modeling drought and rain precipitation, and can be used to monitor crop yield and predict floods and landslides [5, 6, 7, 8, 9].

1.1 Remote Sensing of Sea Ice

Arctic sea ice can be broadly classified as first-year (FY) or multiyear (MY) by spaceborne microwave sensors. The different physical properties of first-year ice and ice that has persisted beyond a melt season (MY ice) result in different backscatter signatures and differences in microwave emissivity. Using active and passive microwave sensors on a spaceborne platform enables classification of the spatial extent of FY and MY ice in the Arctic.

Using a spaceborne sensor to monitor ice in the Arctic has several advantages compared to traditional monitoring from plane, boat, or buoy. The spaceborne sensor enables large spatial coverage with a high revisit frequency. In practice, images of the entire Arctic can be observed at relatively fine resolution ($\approx 4.45 \times 4.45$ km/pixel) using image reconstruction techniques on scatterometer data. Since most scatterometers are placed in near-polar orbits, such sensors have high revisit frequencies over the poles, enabling many observations over the Arctic. Passive sensors likewise benefit from broad spatial coverage and high revisit frequencies over the Arctic.

As sea ice classification algorithms using only passive data have been shown to be unreliable due to sensitivity to snow cover depth and the wide variation in emissivity from

different areas of MY ice [10, 11, 12], alternative techniques using active sensors have been developed. In particular, NASA's Ku-band Quick Scatterometer (QuikSCAT) has been used to classify the area of FY and MY ice using a temporally varying threshold on reported backscatter values [2, 13].

1.2 Soil Moisture

The National Research Council's Decadal Survey emphasizes the importance of soil moisture measurements, citing their significance in predicting natural hazards and the role of soil moisture levels in the water and carbon cycles [5]. Various algorithms have been devised to use active and passive spaceborne sensors to estimate soil moisture levels [3, 14, 15, 16], and interest in soil moisture retrieval has prompted the development of new satellite sensors designed primarily for soil moisture monitoring. For example, the ESA's Soil Moisture and Ocean Salinity sensor, and NASA's Soil Moisture Active Passive sensor are specifically designed to provide accurate soil moisture estimates [17, 16]. Although ground based in-situ measurements of soil moisture are available in many locations, spaceborne sensors provide the advantage of a wide range of spatial coverage, especially in remote or inaccessible areas.

1.3 Research Problem Statement

Using spaceborne scatterometers and passive microwave sensors, many different geophysical phenomena can be observed and quantified. Two applications of satellite microwave sensor data include classification of Arctic sea ice and soil moisture estimation.

Classifications of sea ice have previously been completed with the QuikSCAT sensor; unfortunately, a failure of the spin mechanism of the QuikSCAT sensor in 2009 halted the rotation of its dish antenna and resulted in a significantly reduced coverage pattern, hampering its effectiveness for ice classification. To continue the ice classification record, another sensor must be employed in the absence of QuikSCAT. The resulting record needs to be calibrated to the QuikSCAT record.

Fortunately, the Ku-band Oceansat-2 Scatterometer (OSCAT), launched by the Indian Space Research Organization in 2009 is very similar to the QuikSCAT scatterometer and is a viable candidate for continuing the ice classification data record. Certain differences

between OSCAT and QuikSCAT, however, must be accounted for in order to create a consistent ice classification data record spanning from the beginning of the QuikSCAT record in 1999 to the failure of the OSCAT sensor in 2014.

Since the failure of the OSCAT sensor, there exist no Ku-band scatterometers suitable for ice classification with readily available data. Instead, C-band data from the currently operational Advanced Scatterometer (ASCAT) can be used to continue ice classification. As C-band scatterometers are less sensitive to differences between FY and MY ice, additional data from passive microwave sensors could be use to augment data from ASCAT and improve the classifications.

Data from the ASCAT sensor have also been used for soil moisture estimation. Current ASCAT soil moisture retrieval algorithms, however, do not take advantage of enhanced resolution image reconstruction techniques. By applying such techniques to current soil moisture estimation methodologies, finer-detailed images of soil moisture can be produced.

By extending the QuikSCAT ice classification data record and developing a high-resolution soil moisture estimation technique, extended data records can be constructed which capture information on earth's geophysical phenomena. A long, consistent data record of ice in the Arctic could enable a better understanding of the effect of climate change on the properties of Arctic sea ice. Likewise, a high-resolution time series of observations of soil moisture over the globe could improve understanding of the earth's water cycle and weather systems.

1.4 Thesis Statement

The purpose of this thesis is to extend the QuikSCAT ice classification data record using OSCAT and to develop techniques for ice classification and high-resolution soil moisture estimation using ASCAT. To extend the QuikSCAT ice classifications, an adjusted ice classification method is developed and applied to QuikSCAT and OSCAT data; the resulting ice classification data record extends from 1999 to 2014. To continue ice classification beyond 2014, a new algorithm for ice classification is developed using ASCAT data. Additionally, enhanced-resolution ASCAT data are incorporated into a modified version of an existing soil moisture algorithm to produce high-resolution soil moisture estimates.

The thesis is divided in three main parts. In the first part, the combined QuikSCAT/ OSCAT ice classification methodology is described. Then, an ice classification methodology with ASCAT is detailed. In the third section, the enhanced resolution soil moisture retrieval technique is described.

The combined QuikSCAT/OSCAT classification methodology builds on the previously completed QuikSCAT classifications [2]. In the previous QuikSCAT classifications, brightness temperature data from the Advanced Microwave Scanning Radiometer - Earth Observing System (AMSR-E) are employed to restrict the area of classification to within the sea ice extent. Then, a temporally varying threshold on backscatter values from QuikSCAT is applied to classify the ice as FY or MY. In the QuikSCAT/OSCAT classifications, an ice concentration product which spans the length of the data record is used to restrict the area of classification to within the sea ice extent. Then, adjustments are made to the OSCAT data to compensate for anomalies caused by power fluctuations in the sensor. Classifications are completed using temporally varying thresholds, and a correction algorithm is developed and applied to reduce areas which appear to be incorrectly classified MY ice. Daily ice classification images are produced for years 1999 to 2014.

The failure of the OSCAT sensor motivates the continuation of the ice classification record using another sensor. In the absence of a Ku-band sensor with readily available data, the C-band ASCAT sensor is selected to complete the classification. Due to the relative insensitivity of C-band backscatter measurements to FY and MY ice differences, brightness temperature measurements from the passive microwave sensor, the Special Sensor Microwave Imager Sounder (SSMIS) are used to augment the ASCAT data. Using a Bayesian classifier, areas of FY and MY ice are classified.

The enhanced resolution soil moisture retrieval technique is developed by building on an existing soil moisture algorithm developed at the Vienna University of Technology (TU-Wien). Presently, both 12.5 $\times$ 12.5 and 25 $\times$ 25 km/pixel resolution global soil moisture products are being produced using this algorithm [18]. The products are processed using the Water Retrieval Package (WARP) algorithm with data from the C-band Advanced Scatterometer (ASCAT) sensors aboard the Metop-A and Metop-B satellites [3]. To produce an improved resolution product, the AVE algorithm [19] is used to create higher resolu-

tion images (4.45 × 4.45 km/pixel) of the radar backscatter coefficient (σ^0). Exploiting ASCAT's high-resolution image capability enables higher resolution images of soil moisture than are currently available. By resolving finer soil moisture features, the higher resolution soil moisture images could complement soil moisture-related studies in such areas as crop yield prediction, drought prediction and localization, and modeling of the water table and water cycle [5].

1.5 Research Contributions

The research presented in this thesis results in new algorithms for ice classification and enhanced resolution soil moisture retrieval. The specific contributions are (1) an ice classification data record using the QuikSCAT and OSCAT sensors which spans 15 years, (2) a new technique for classifying FY and MY ice using ASCAT and SSMIS, and (3) a novel technique for high-resolution soil moisture retrieval using the AVE algorithm and the WARP soil moisture retrieval technique. In addition, the ASCAT/SSMIS classification technique can potentially be used to continue ice classifications far into the future as multiple iterations of the ASCAT sensor are currently operational and yet another iteration is planned; the SSMIS sensor also flies on multiple platforms and should continue to be operational for years to come. The results of the QuikSCAT/OSCAT classification record are contained in [13] and a description of the ASCAT/SSMIS classification methodology has been submitted for publication. A description of the enhanced resolution soil moisture algorithm has also been submitted for publication.

1.6 Thesis Organization

The thesis is divided into three major topics: a description of the QuikSCAT/OSCAT ice classification methodology, documentation of the ASCAT/SSMIS ice classification algorithm, and a description of the enhanced resolution soil moisture retrieval technique. A brief description of each chapter follows.

Chapter 2 provides background on the remote sensing properties of Arctic Sea ice and classification of MY and FY ice using QuikSCAT. It continues by detailing the improved classification methodology using QuikSCAT and OSCAT and provides results.

Chapter 3 provides an overview of the ASCAT and SSMIS sensors and details the ASCAT/SSMIS ice classification methodology. The classification results are compared to the OSCAT ice classifications and another ice age classification product from the National Snow and Ice Data Center.

Chapter 4 outlines the Tu-Wien algorithm for soil moisture retrieval and discusses enhanced resolution image reconstruction techniques for scatterometers. The enhanced resolution soil moisture estimation algorithm is detailed and results are provided.

Chapter 5 concludes the thesis and summarizes the results of the research. Major contributions are detailed as well as potential paths for future work.

Chapter 2

Ice Classification Using QuikSCAT and OSCAT

This chapter reviews the physical and scattering properties of FY and MY sea ice and discusses previous work on classifying FY and MY ice with QuikSCAT. A revised ice classification methodology is introduced which extends the QuikSCAT ice classifications using the Oceansat-2 scatterometer (OSCAT). Results of the revised classification methodology are also provided.

2.1 Remote Sensing of Sea Ice

Classification of Arctic sea ice age using scatterometers is possible because of physical changes in ice composition that naturally result over time. As sea ice ages, its structure transforms, resulting in differing backscatter signatures from young and old ice. Such differing backscatter signatures enable remote classification of ice type using satellite scatterometers.

Arctic sea ice can be broadly classified into two major categories: FY and MY. FY Arctic sea ice consists of ice formed after the most recent melt season. It is typically characterized by rough surface features, thickness of less than 1.5 m, and a high brine content[20]. During the summer melt season, a process of desalination occurs, leading to significant changes in the physical properties of the ice. Warming temperatures cause pockets of brine existing in the FY ice to coalesce and drain, creating in vertical drainage channels and air pockets. Melting surface ice also leads to desalination by creating a layer of freshwater which filters through the existing layers of ice. As the ice melt seeps through the top layers of the ice, the brine content is further reduced [20]. Changes in the physical properties of FY ice caused by the melt season result in MY ice, which is typically characterized by smoother surface features, thickness greater than 1.5 m, greater porosity, and a lower brine content [20].

Various physical properties of sea ice, including thickness, porosity, salinity, and surface roughness, contribute to differences in the observed backscatter. The rough surface features characteristic of FY ice result in increased backscatter, though the greater salinity of FY ice makes it a higher-loss medium than MY ice. Typically, volume scattering resulting from the porosity of MY ice causes MY ice to exhibit greater radar backscatter than FY ice.

FY and MY ice also exhibit differing passive microwave signatures. Observations from passive microwave sensors show that at frequencies greater than approximately 20 GHz, FY ice has a greater emissivity than MY ice [21]. The differing passive microwave signatures of FY and MY sea ice result from the different physical properties of the ice types and other factors. Brine content of the ice, the ice crystalline structure, snow accumulation, and recrystallization of ice at the interface between snow and ice each contribute to the observed differences in emissivity between FY and MY ice [21].

Near the sea ice edge, the area of ice cover can become fragmented by the incursion of ocean waves and swells. Such areas are part of the marginal ice zone (MIZ) [22]. Surface roughness can cause backscatter measurements from areas of the MIZ and from open water to appear similar to backscatter from MY sea ice.

2.2 Ice Classification

A record of daily Arctic sea ice classification images was produced by Swan and Long (hereafter SL) using data from NASA's Quick Scatterometer (QuikSCAT)[2]. The SL ice classification record extends from 2002 to 2009 and is concluded by the failure of the spin mechanism of the QuikSCAT sensor in 2009. The Oceansat-2 Ku-band Scatterometer (OSCAT) was launched in 2009 by the Indian Space Research Organization (ISRO) and is similar to NASA's Quick Scatterometer (QuikSCAT), motivating the use of OSCAT to extend the SL record. OSCAT is here used with a modified ice classification algorithm based on the one created by SL. The QuikSCAT classifications are reprocessed using the modified algorithm for 1999 to 2009 and OSCAT is used to extend this record through 2014.

The SL algorithm classifies FY and MY Arctic sea ice for a given day by generating a high-resolution (4.45×4.45-km/pixel) image of the Ku-band radar backscatter coefficient (σ^0) using the SIR algorithm [23, 24], identifying the sea ice extent, and applying a threshold

on backscatter values in the high-resolution image to classify FY and MY ice within the sea ice extent [2].

Ice classification using QuikSCAT is restricted to within the sea ice extent in order to avoid misclassification of the marginal ice zone and areas of open water. In the QuikSCAT ice classifications completed by SL, a threshold on reported brightness temperatures from the Advanced Microwave Sensor-Earth Observing System (AMSR-E) is used to determine the sea ice extent. As data from AMSR-E is only available from 2002, when it became operational, the SL classifications are produced from 2002 until the malfunction of the QuikSCAT sensor in 2009. Data from QuikSCAT is available as early as 1999, however, so ice classifications from 1999 to 2001 could potentially also be produced.

To produce ice classifications for the full length of the QuikSCAT mission and extend the QuikSCAT classifications using OSCAT, an alternative method is used to identify the sea ice extent. The ice extent is identified by applying a threshold to a NASA Team ice concentration product produced using passive microwave sensors [1]. Using the NASA Team ice concentration data, ice classifications are reprocessed for QuikSCAT from 1999 to 2009 and OSCAT is used to extend these classifications through 2014.

After the classifications are completed for QuikSCAT and OSCAT, transient areas of classified MY ice appear near the ice edge in some regions. Where true MY ice persists until a melt, these areas of classified MY ice near the ice edge appear and disappear over the course of a few days. Such transient areas appear to be misclassifications caused by high backscatter from the MIZ and are suppressed by applying a correction algorithm to the initial classifications.

2.3 Sensor Information

The consistency of the Arctic ice age classification data record is related to the similarity of the OSCAT and QuikSCAT sensors. A comparative summary of OSCAT and QuikSCAT is found in Table 2.1. The sensors have similar features including antenna dimension, frequency, polarization, and orbital characteristics.

Both OSCAT and QuikSCAT operate at Ku-band using a 1 m dual-feed parabolic antenna with a horizontally polarized (HH) inner beam inner and a vertically polarized (VV)

outer beam. Backscatter from VV is used in this study for ice classification, and the VV incidence angles vary slightly between the two sensors. For QuikSCAT, the VV incidence angle is a constant 54°, and for OSCAT it is 57°. The difference in incidence angle is especially relevant to ice classification because σ^0 is partially dependent on incidence angle, and a threshold on σ^0 is used to distinguish between FY and MY ice. The relationship between σ^0 and incidence angle can be linearly approximated with σ^0 decreasing as the incidence angle increases. The difference in incidence angle between OSCAT and QuikSCAT and its effect on backscatter is relevant to selecting a consistent classification threshold on σ^0.

The scatterometers share a similar sun-synchronous near-polar orbit with similar orbital inclinations of 98.6° and 98.28° for QuikSCAT and OSCAT, respectively. QuikSCAT operates at a slightly greater orbital altitude of 803 km compared to OSCAT's 720 km, but the coverage patterns of the sensors are similar enough that Arctic σ^0 images used for classification can be created at the same temporal resolution. The similarities between the OSCAT and QuikSCAT sensors motivate the use of OSCAT to continue the classification data record in the absence of QuikSCAT data.

2.4 Ice Classification with QuikSCAT and OSCAT

In the modified SL algorithm, the NASA Team ice concentrations are adapted as a replacement for AMSR-E in defining the ice extent to enable classification with QuikSCAT and OSCAT. The use of one ice extent product across the entire QuikSCAT/OSCAT classification record improves the consistency of the record. Differences between the OSCAT and QuikSCAT sensors are analyzed in order to identify potential sources of inconsistency, and classification thresholds for processing ice classifications with OSCAT and QuikSCAT are also determined.

2.4.1 NASA Team Ice Extent

In the first step of the modified SL algorithm, areas of sea ice in high-resolution images of σ^0 over the Arctic are isolated using a NASA Team ice concentration product [26, 1]. The NASA Team product was selected because of its availability and the relative insensitivity of

Table 2.1: Characteristics of QuikSCAT and OSCAT [25]

Parameter	QuikSCAT		OSCAT	
Organization	National Aeronautics and Space Administration (NASA)		Indian Space Research Organization (ISRO)	
Antenna Type	1 m dual-feed parabolic		1 m dual-feed parabolic	
Frequency	13.402 GHz		13.515 GHz	
Orbital Period	101 min (14.25 orbits/day)		99.31 min (14.5 orbits/day)	
Orbital Inclination	98.6°		98.28°	
Equator Crossing	6 A.M/6 P.M.		12 A.M/12 P.M.	
Satellite Altitude	803 km at equator		720 km at equator	
Scan Rate	18 rpm		20.5 rpm	
PRF (per beam)	92.5 Hz		96.5 Hz	
Start Date	June 19, 1999		Sept. 23, 2009	
End Date	Nov. 23, 2009		Feb. 20, 2014	
SIR Image Resolution	4.45- × 4.45-km/pixel		4.45 × 4.45 km/pixel	
	Inner Beam	Outer Beam	Inner Beam	Outer Beam
Polarization	HH	VV	HH	VV
Incidence Angle	46°	54°	49°	57°
Slant Range	1100 km	1245 km	1031 km	1208 km
Swath Width	1400 km	1800 km	1400 km	1836 km
One-way Beamwidth (Az x El)	1.8° x 1.6°	1.7° x 1.4°	1.47° x 1.62°	1.39° x 1.72°

the classification results to the ice extent used. Following SL, we use the threshold of 40% ice concentration to delineate the sea ice extent. The subjective choice of threshold is motivated by the general insensitivity of the ice extent to the threshold chosen and by demonstrated use of the 40% threshold in other ice classification studies [2, 27]. Isolating the area of the sea ice extent targets the classification algorithm to the relevant area of Arctic sea ice.

2.4.2 OSCAT Incidence Angle Considerations

Continuing the ice classification data record using data from OSCAT requires dealing with the disparity in incidence angles between QuikSCAT and OSCAT. Fortunately, although the reported σ^0 values from QuikSCAT and OSCAT differ because of the unequal incidence angles, a corrective factor for σ^0 is unnecessary. To determine the separation line between MY and FY ice, a separate histogram series of daily σ^0 values is produced for each year.

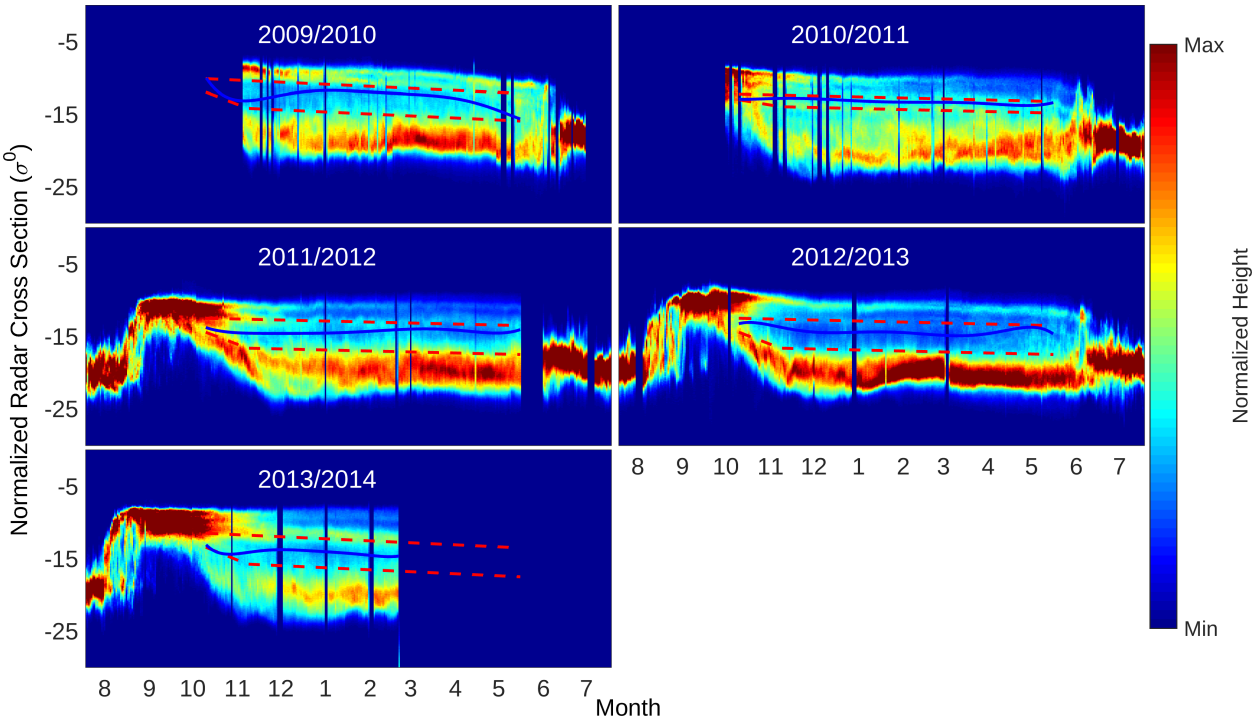

Figure 2.1: Time series of corrected OSCAT daily σ^0 histograms for the winter seasons from 2009 to 2014. A blue curve is fitted to minimum points and used as a threshold for FY and MY ice classification. The red, dashed lines are subjective bounds used constrain the threshold to the area between peak distributions corresponding to FY and MY ice.

Borders are placed subjectively to roughly isolate the area of the minimum bin count, then minimum points within the borders are identified, and a MY ice threshold curve is fitted to these points. The OSCAT time series histograms and thresholds are shown in Fig. 2.1. The thresholds effectively ignore any constant shift in σ^0 values because they are calculated relative to the distribution of σ^0 values in the annual histograms. The MY ice thresholds thus self-adjust to the slightly lower σ^0 values of the OSCAT data, and this alleviates the need for an explicit incidence angle correction factor.

2.4.3 Ice Classification Thresholding

After the area of the sea ice extent is identified using the NASA Team ice concentration product, ice within the extent is classified with OSCAT or QuikSCAT. Classifying ice age for OSCAT requires certain modifications to the SL classification algorithm. While a classification threshold is determined for QuikSCAT using a multiyear average of time se-

ries backscatter histograms, calibration inconsistencies with OSCAT across the instrument lifetime motivate the adoption of a piecewise threshold calculated independently for each year.

Unfortunately, the original OSCAT σ^0 dataset demonstrates small jumps and shifts in reported σ^0 values that appear to be caused by noise and power calibration fluctuations [28]. These shifts appear in a daily series of histograms in Fig. 2.1 and Fig. 2.2. Some years have consistently higher or lower σ^0 values, and intra-annual variability is especially apparent in the winter of 2009/2010 where σ^0 values for several days' data jumps up and down throughout the year.

The jumps in reported σ^0 that occur during the winter of 2009/2010 require that a correction be applied to the data. For this purpose, the 2009/2010 series of daily histograms is re-processed using an algorithm which identifies areas of shifted σ^0 values, determines the magnitude of the shift, and applies a correction. The correction is intended to align the data and eliminate shifts in σ^0 values. Uncorrected and corrected versions of the 2009/2010 annual histogram are shown in Fig. 2.2. With the removal of the shifts, the corrected version shows significantly improved continuity.

Although SL use a multiyear average of the QuikSCAT σ^0 time series histograms to calculate a MY ice threshold, averaging OSCAT data across years yields an undesirable threshold curve because of the instrument anomalies. Instead of using the multiyear average for OSCAT, a piecewise threshold model is determined for each year separately. Bounds are set subjectively for each histogram of winter σ^0 values (DOY 284 to DOY 134) by attempting to isolate the area of minimum bin counts that persists for most of the winter.

The minimum points between the bounds are identified for each day, and a fifth-degree polynomial is fitted to the minimum points in time. The order of polynomial is selected to smooth the noisy day to day variation in the minimum points while also allowing a flexible fit to the time series. As the ice classifications are not extremely sensitive to small changes in the threshold, the order of the polynomial is relatively unimportant. Days that do not occur between DOY 284 and DOY 134 are considered to be part of the summer melt, and ice is not classified during this period. This classification scheme results in a piecewise function which is used as a MY ice threshold. MY ice threshold curves for each year are shown in Fig. 2.1.

The threshold curves vary from about -12 dB to -15 dB and the bounds fluctuate between -10 dB and -17 dB, depending on the year. The variation in the curves and bounds is due in part to the inter-annual shifts in reported σ^0 values which skew the datasets. Application of these thresholds to OSCAT produces a consistent dataset for the years 2009 to 2014.

QuikSCAT ice age classifications are reprocessed using an average time series of QuikSCAT daily σ^0 histograms to determine the classification threshold. To produce the average histogram time series, an average histogram for each DOY is computed using daily σ^0 histograms from 1999 to 2009. The resulting average daily histograms are arranged in a time series and reveal the average temporal progression of backscatter distributions throughout the year. The threshold is determined by fitting a fifth degree polynomial to bin count minima in the average histogram series between peak distributions representing FY and MY ice. As with the OSCAT threshold, the order of the QuikSCAT threshold polynomial is selected to smooth noisy day to day variations in the bin minima locations while preserving flexibility in the fit. The average time series histogram, minimum bin points, and classification threshold are shown in Fig. 2.3. The resulting classifications extend the previous SL ice age classifications backwards for the years 1999 to 2002. These years were not classified by SL because AMSR-E had not yet become operational. The full QuikSCAT dataset extends from 1999 to 2009.

2.5 The MIZ Correction Algorithm

The MIZ is characterized by fragmented ice floes near the ice edge which are broken up by incoming waves. This slurry of ice near the ice edge is a transition zone between a thicker continuous ice sheet and the ocean. The rough surface properties of the MIZ can result in high radar backscatter which exceeds the classification threshold used to distinguish between FY and MY ice. When the classification threshold is applied, certain areas of the MIZ can be erroneously classified as MY ice.

MIZ ice which is incorrectly classified as MY ice must be distinguished from true areas of MY ice that occur near the ice edge. One such area of MY ice near the ice edge is off the east coast of Greenland. In this region, a significant part of the main body of Arctic MY ice advects south and is ejected into the Atlantic ocean. A correction algorithm

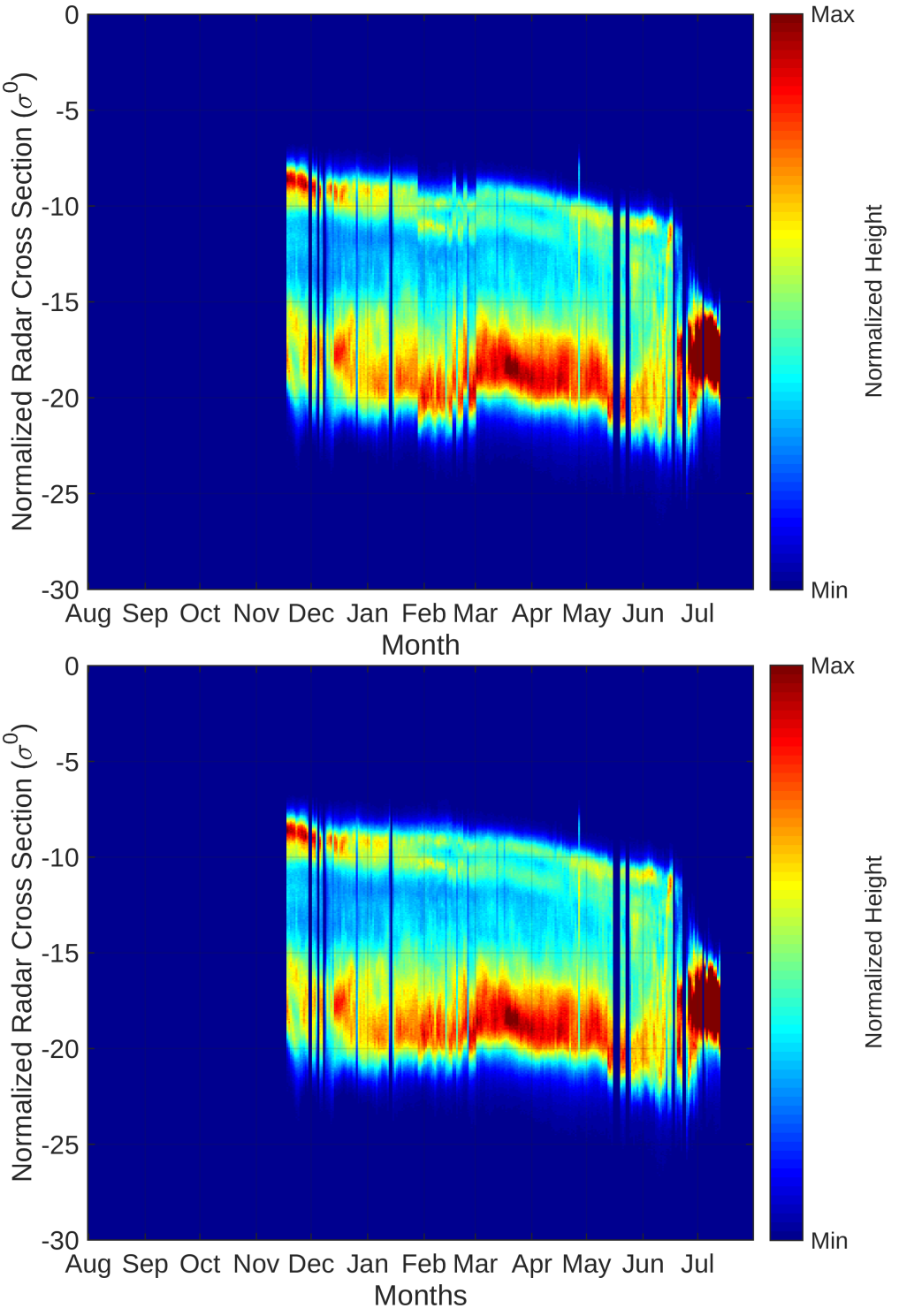

Figure 2.2: The uncorrected OSCAT data (top) and corrected data (bottom) for the winter of 2009/2010 shown in a collection of daily histograms.

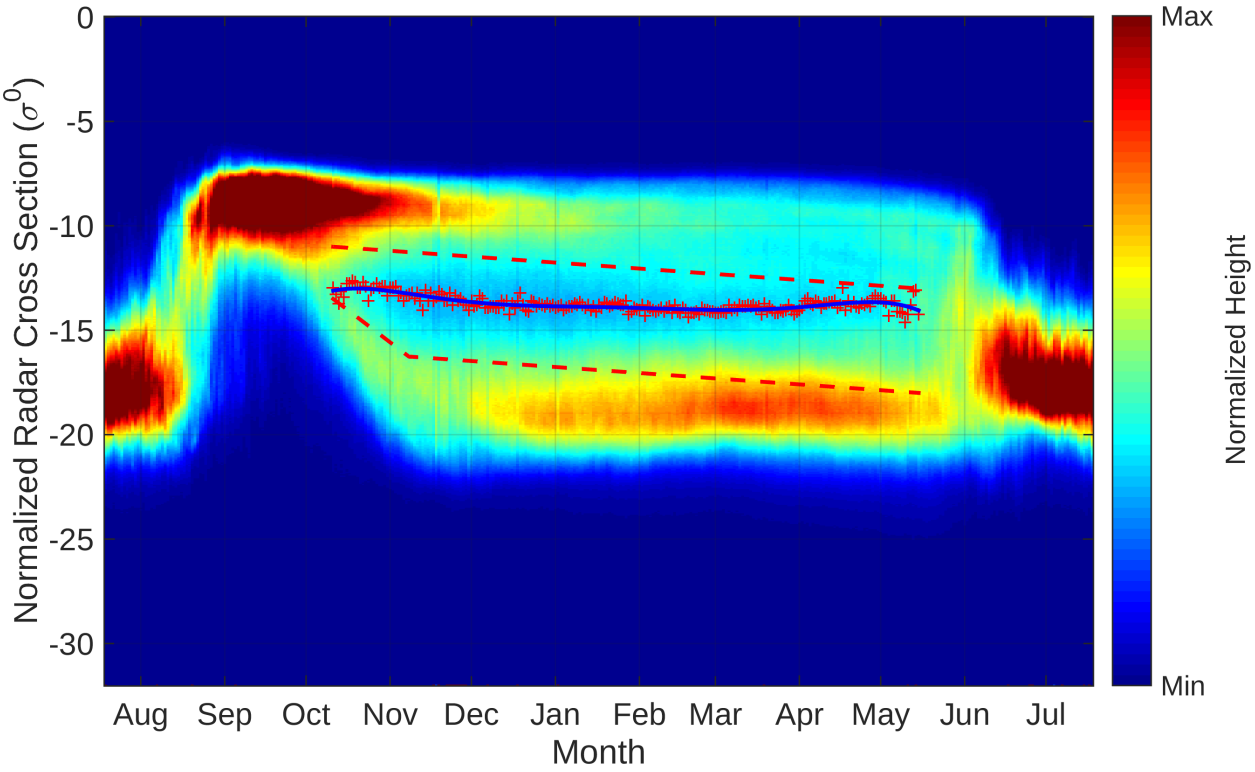

Figure 2.3: Average time series of QuikSCAT daily σ^0 histograms. An average histogram of backscatter values for each DOY is created by averaging daily backscatter histograms from 1999 to 2009. The resulting averaged daily histograms are concatenated into this time series image. A blue curve is fitted to minimum points and used as a threshold for FY and MY ice classification. The red, dashed lines are subjective bounds used constrain the threshold to the area between peak distributions corresponding to FY and MY ice.

is described which distinguishes between MY ice and misclassified areas of the MIZ, and is sensitive to true areas of MY ice near the ice edge.

2.5.1 Correcting MY Ice Misclassifications

Areas in the MIZ where where FY ice is initially misclassified as MY ice can be distinguished from other areas of MY ice based on the temporal transience of the backscatter from the MIZ. High backscatter values throughout the MIZ typically persist for only one to two days, whereas backscatter from MY ice areas remains high as long as melt does not occur. By observing classification patterns over multiple days, misclassification errors can be reduced. The goal of the correction algorithm is to reduce the misclassified MY ice.

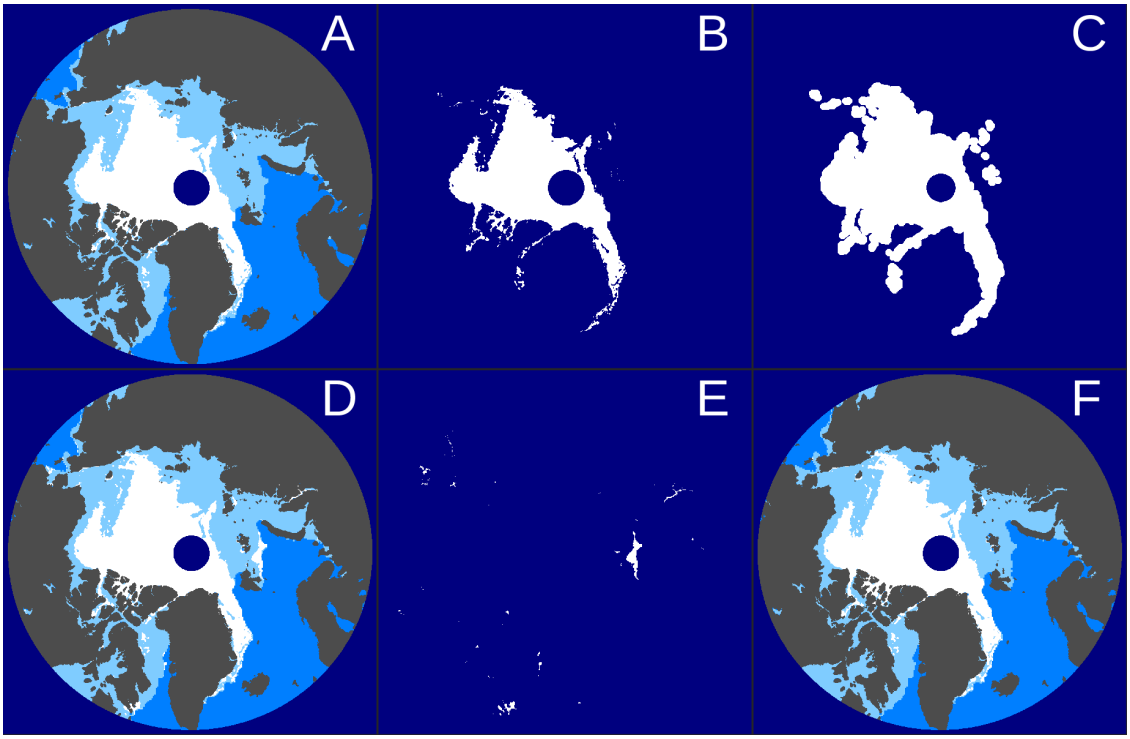

Figure 2.4: Image series showing the application of the MIZ correction algorithm for DOY 1-2, 2001. MY ice is shown in white with FY ice in pale blue. Image A shows classifications from DOY 1, 2001 after the MIZ correction algorithm has been applied. A mask of the area of MY ice from image A is created (image B) and dilated (image C). The initial classifications for DOY 2, 2001 (image D) are compared with the dilated area of MY ice from the previous day (image C). Areas of initially classified MY ice which fall outside of the dilated mask (image E) are removed from the initial classifications. The corrected classifications for DOY 2, 2001 are shown in image F.

The algorithm to mitigate MIZ errors in ice classification uses images of the Arctic where FY and MY ice have already been initially classified. All pixels classified as MY ice are identified and used to create a mask. The mask is then dilated and compared to the area of classified MY ice in the image for the subsequent day. All MY ice which appears outside of the dilated mask is reclassified as FY ice. The process then repeats with a new mask of MY ice being created from the newly adjusted classification image. Fig. 2.4 provides a visual example of the steps of the MIZ correction process. The figure shows that areas of misclassified MY ice in the outside of the derived MY ice mask are reclassified as FY ice.

2.5.2 Correction Algorithm Performance

The performance of the correction algorithm is evaluated using a quantitative measure of the amount of ice that it reclassifies as FY. An area south and east of the island of Svalbard where misclassified MY ice appears frequently and another area near the east side of Greenland are analyzed.

The area near the island of Svalbard extends from 72.6° N latitude to 79.2° N latitude and from 19.4° E longitude to 71.26° E longitude. The ice edge typically falls within this area during the winter and the regions of misclassified MY ice generally appear within 90 km of the ice edge. For each day in which ice is classified, pixels located within 90 km of the ice edge are identified and analyzed. Fig. 2.5 shows an example image of the area near the ice edge and identifies regions where the ice classification was changed from MY to FY.

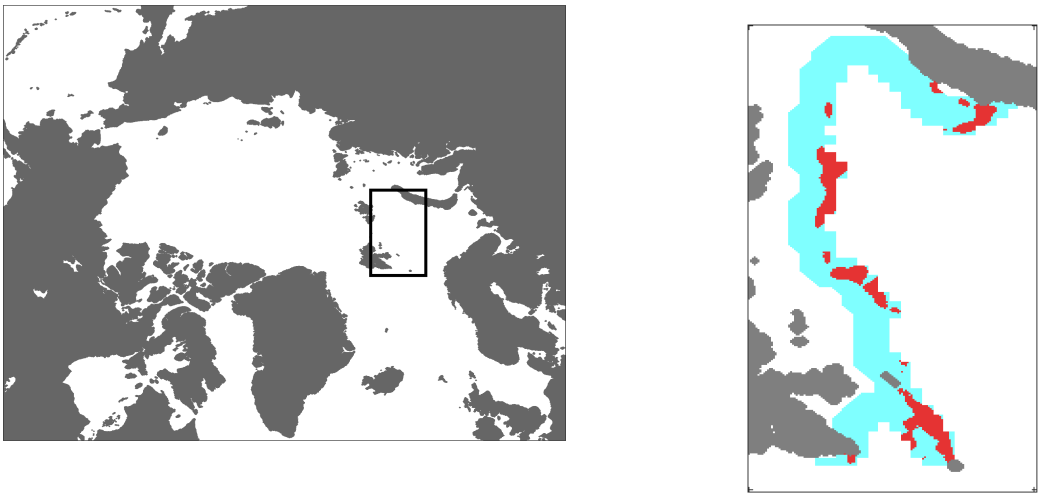

Figure 2.5: Map delineating the study region south and east of the island of Svalbard (left) and a closer perspective (right) showing the effect of the MIZ correction algorithm. Blue pixels in the right image represent FY ice within 90 km of the ice edge. Red pixels represent ice which was reclassified as FY from MY by the MIZ correction algorithm. White pixels represent ice or open ocean outside the MIZ study region.

Much of the ice initially classified as MY near the ice edge is transient and characteristic of misclassifications caused by the MIZ. Fig. 2.6 shows a plot of the area of MY

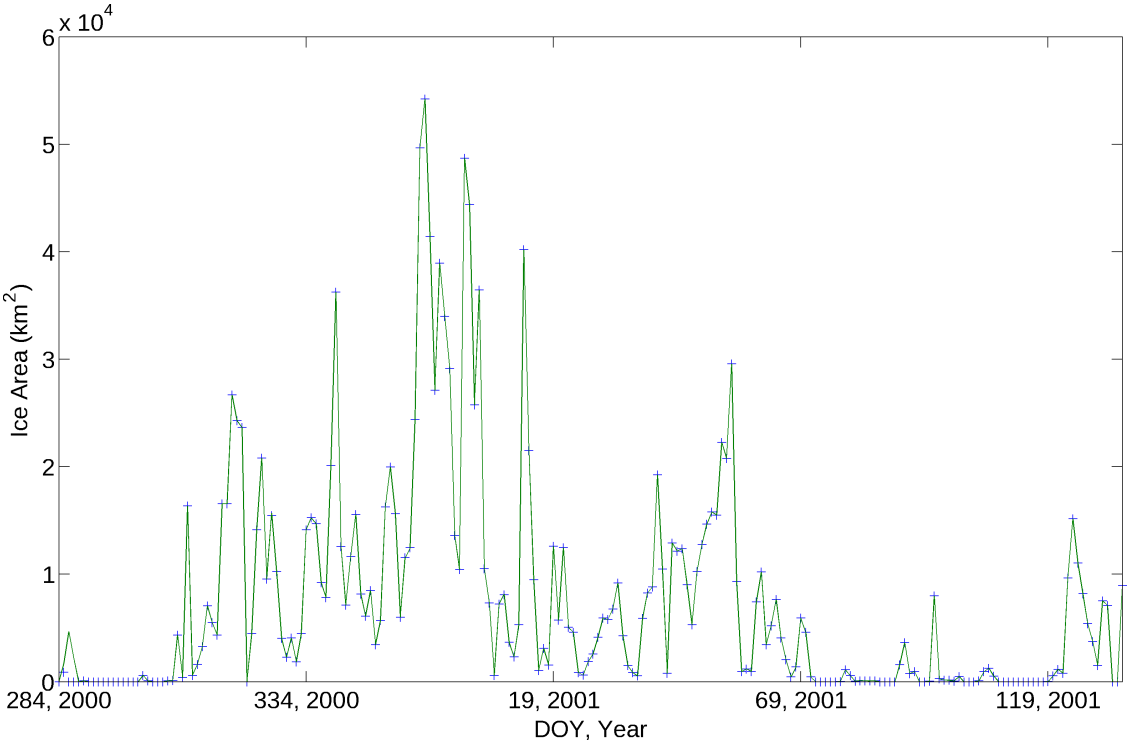

Figure 2.6: Plot of classified MY ice near the ice edge south and east of the island of Svalbard for the winter of 2000/2001. The solid line indicates the total area of classified MY in the area near the ice edge before the correction algorithm is applied. The cross markers indicate the area of classified MY ice which was reclassified as FY ice. Data points from the plots are almost always the same because nearly all of the classified MY ice is reclassified as FY ice.

ice and the area of reclassified MY ice within the region near the ice edge for the winter of 2000/2001. At the beginning and end of the winter, the area of initially classified MY ice near the ice edge is minimal, though the amount increases during the middle of the winter, varying from around 10,000 to 50,000 km^2 within the study region. The high variability of the levels of initially classified MY ice is not characteristic of true MY ice, which persists until a melt occurs. We postulate that high backscatter from the MIZ has resulted in incorrect initial MY ice classifications. The correction algorithm consistently reclassifies these transient areas of MY ice as FY ice.

Near the east coast of Greenland, some areas of MY ice exist near the ice edge. A study area is defined to explore the effects of the MIZ correction in this area and extends from 64.2° N latitude to 79.6° N latitude and from 23.2° W longitude to 23.5° W longitude. Fig. 2.7 shows an image of the region and identifies pixels classified as MY and FY ice within

the region. Since much of the ice in this area appears to be true MY ice, the MIZ correction algorithm should not typically reclassify any MY ice to FY ice.

The performance of the MIZ correction algorithm is shown for the winter of 2000/2001 in Fig. 2.8. The area of MY ice near the coast of Greenland increases throughout the winter before decreasing prior to the summer melt. The MIZ correction algorithm reclassifies a minimal amount of MY ice to FY ice. This is consistent with the SL results and is the desired performance because the initial classifications of MY ice near the east coast of Greenland appear to correctly identify areas of true MY ice. Jumps in the MY ice area in Fig. 2.8 result from movement of the sea ice edge and from areas of classified FY ice which occasionally appear within the area of MY ice due to changes in backscatter from the region. The correction algorithm does not reclassify such areas of classified FY ice to MY ice.

Different parameters of the MIZ correction algorithm could be adjusted to alter performance. The lag time, or time difference between the classification day used to produce the MY ice mask and the classification day to which the MY ice mask is compared, could be adjusted. Also, a different method of producing the MY ice mask could be implemented using averaging or another technique. The described correction method is selected because of its reasonable performance; however, future work could be done to explore the effect of adjustments to the correction algorithm parameters.

The MIZ correction algorithm appears to correctly identify and correct areas of erroneously classified MY ice near the ice edge. A time series of corrections applied in 2001 is shown in Fig. 2.9. Throughout the time series, areas of MY ice which have been reclassified as FY ice are shown in red. The time series demonstrates that the algorithm can effectively reclassify ice in multiple areas near the ice edge while leaving consistent areas of true MY ice unperturbed. The correction algorithm is applied to the initial QuikSCAT and OSCAT ice classifications in order to remove misclassified MY ice.

2.6 Results

Ice classifications completed using OSCAT and QuikSCAT result in a nearly continuous record from 1999 to 2014 that can be analyzed to determine trends in Arctic ice levels. Plots of MY ice area and ice extent area throughout the time series are shown in Fig. 2.10.

MY ice levels are derived from the ice classifications created from the MY ice threshold curves and data from QuikSCAT and OSCAT. The total ice area is calculated by applying a 40% threshold to the NASA Team ice concentration product to determine ice extent. The area of the pole hole is a no-data region and is not added to the ice extent or MY ice areas. Jumps or increases in the area of MY ice during winter seasons throughout the time series are due to areas near the ice edge which demonstrate high backscatter for several days before decreasing. In these cases, the ice is classified as MY despite the correction algorithm because of the persistence of the high backscatter values. Larger shifts in MY ice area occur at a few instances in the time series when such areas of high backscatter appear near the ice edge close to the east coast of Greenland or near the Davis Strait.

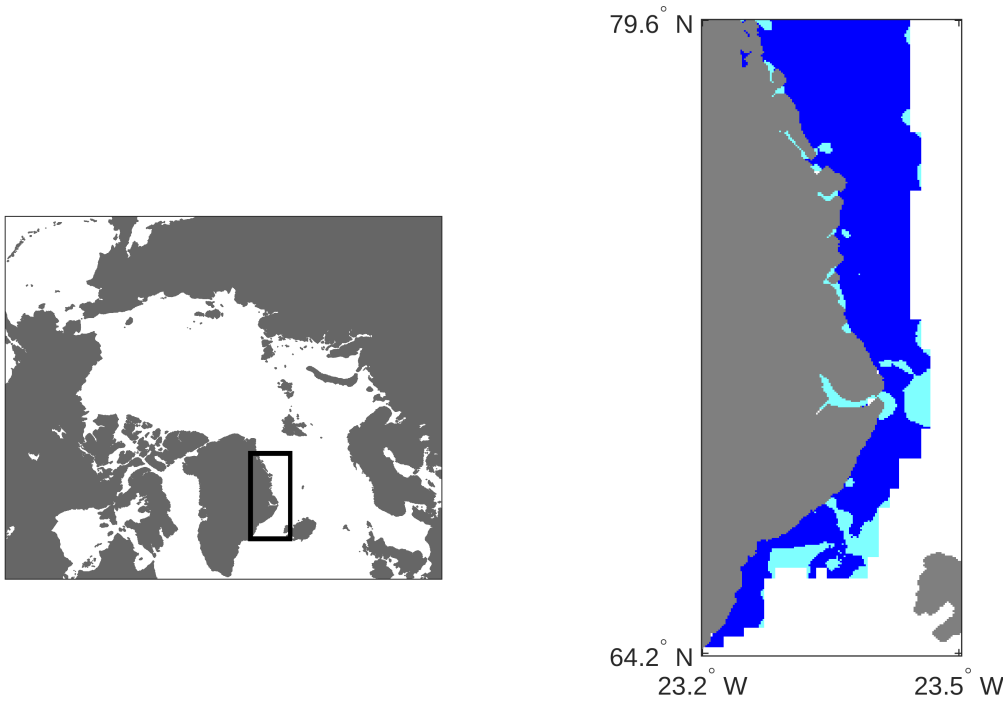

Figure 2.7: Map delineating the study region on the east coast of Greenland (left) and a closer perspective (right) showing ice classifications after applying the MIZ correction algorithm. White pixels in the right image represent ocean areas outside the MIZ. Dark blue and turquoise pixels represent areas classified as MY and FY ice respectively. In this case, the initial classifications were not changed by the correction algorithm.

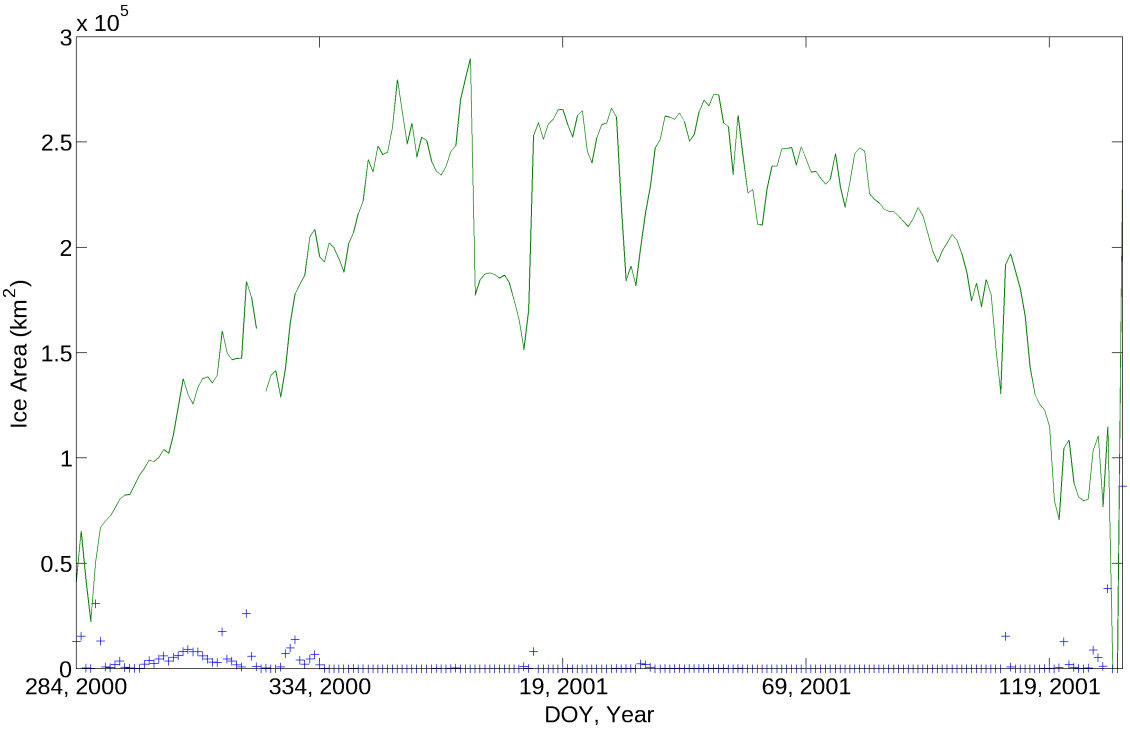

Figure 2.8: Plot of classified MY ice near the east coast of Greenland for 2000 to 2001. The solid line indicates the total area of classified MY in the area near the ice edge before the correction algorithm is applied. The cross markers indicate the area of classified MY ice which was reclassified as FY ice. Days with missing data produce gaps in the plot.

The greatest area of MY ice appears to occur in 2003, and the area of MY ice declines in the following years, reaching a low in 2013. For winter seasons during the time series (from October to May), the average change in MY ice area is a decrease of approximately 846,000 km^2. The greatest decrease in winter averaged MY ice area is roughly 853,000 km^2 between the winters of 2006/2007 and 2007/2008; the greatest increase is roughly 1.24 million km^2 between the winters of 2012/2013 and 2013/2014.

General trends in FY and MY ice area can be seen in Fig. 2.12, which shows classification images from DOY 45 for each year of the time series. The decrease in MY ice appears to be influenced by the advection of ice into the Atlantic Ocean occurring on the east coast of Greenland and through the Davis Strait. In 2014, the MY ice area appears to recover somewhat and is comparable to levels observed in 2005 or 2006. The total area of the ice extent is seasonally dependent, though the peak extent area in winters throughout the time series is relatively consistent (around 11 million km^2). The lowest ice extent area is

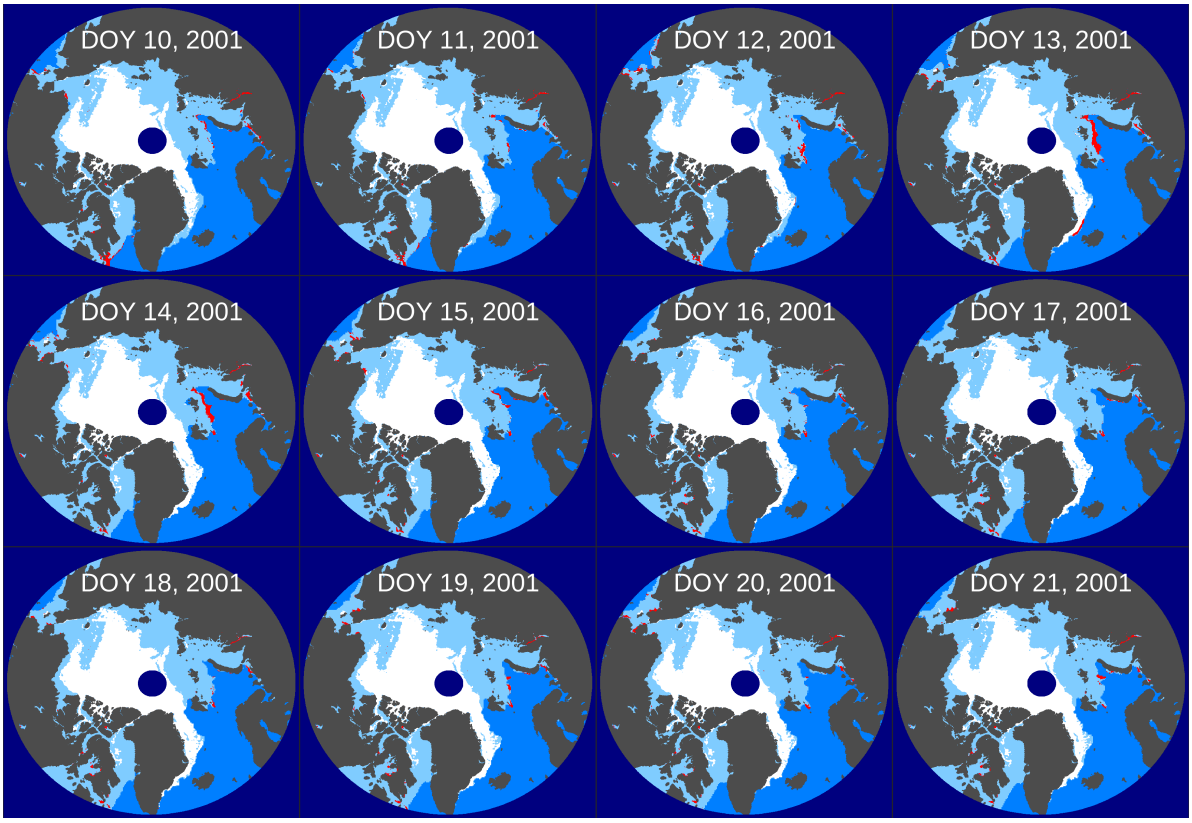

Figure 2.9: Time series of images from DOY 10 through DOY 21, 2001 where the correction has been applied. MY ice is shown in white, FY ice is pale blue, and ocean is medium blue. Areas of initially classified MY ice which have been reclassified as FY ice are shown in red.

observed in the summer of 2012, though in 2013 the summer ice extent increases and is also comparable to levels observed in 2005 or 2006. Overall the results indicate a general decline in the area of MY ice with a possible recovery of ice area in 2014.

The QuikSCAT classifications reprocessed with the modified algorithm demonstrate similar results to those processed by SL, though slight differences in reported ice extent area and MY ice area can be observed. As shown in Fig. 2.10, the ice extent calculated with a threshold on AMSR-E brightness temperature images corresponds well to the ice extent calculated using a 40% ice concentration threshold on the NASA Team ice product. The NASA Team-derived ice extent is an average of 164,800 km^2 greater than the AMSR-E extent during winter days in which ice age is classified from 2002 to 2009.

The MY ice area of the reprocessed QuikSCAT classifications, shown in Fig. 2.10 and with more detail in Fig. 2.11, is on an average of 127,000 km^2 lower than the SL

classifications. This difference is small relative to the total MY ice extent, which ranges between approximately 2 to 5 million km^2 between 2002 and 2009. The lower MY ice area of the reprocessed classifications is partly due to the MIZ correction algorithm, which removes some erroneously classified areas of MY ice that are present in the SL classifications. Before the correction algorithm is applied, the average area of MY ice in the reprocessed classifications is only 29,400 km^2 lower than the SL classifications. The results from the reprocessed data thus correspond well to the previous SL results.

2.7 Conclusion

Ice age classifications processed with OSCAT data extend the QuikSCAT classification record resulting in a 15-year record that extends from 1999 to 2014. Classifications completed with QuikSCAT agree well with classifications previously completed by SL and demonstrate a marked decrease in the amount of Arctic MY ice across the dataset. The classification data are distributed publicly as part of the NASA Scatterometer Climate Record Pathfinder project (http://www.scp.byu.edu).

Due to the failure of OSCAT in 2014, work to continue ice classification requires a different sensor. There are currently no fully operational Ku-band sensors which could be used; however, the C-band ASCAT-A and ASCAT-B sensors (launched by the European Space Agency in 2006 and 2012) are currently operational. To adapt the ice classification algorithm to the ASCAT sensors, the differences in sensitivity to FY and MY ice at C-band compared to Ku-band would need to be addressed. The longer wavelength of the ASCAT sensors compared to QuikSCAT or OSCAT results in decreased sensitivity to volume scattering from porous MY ice and increased responsiveness to backscatter from the MIZ [29]. In Chapter 3, an alternate classification algorithm is proposed that uses ASCAT data combined with passive microwave data to synergistically classify ice.

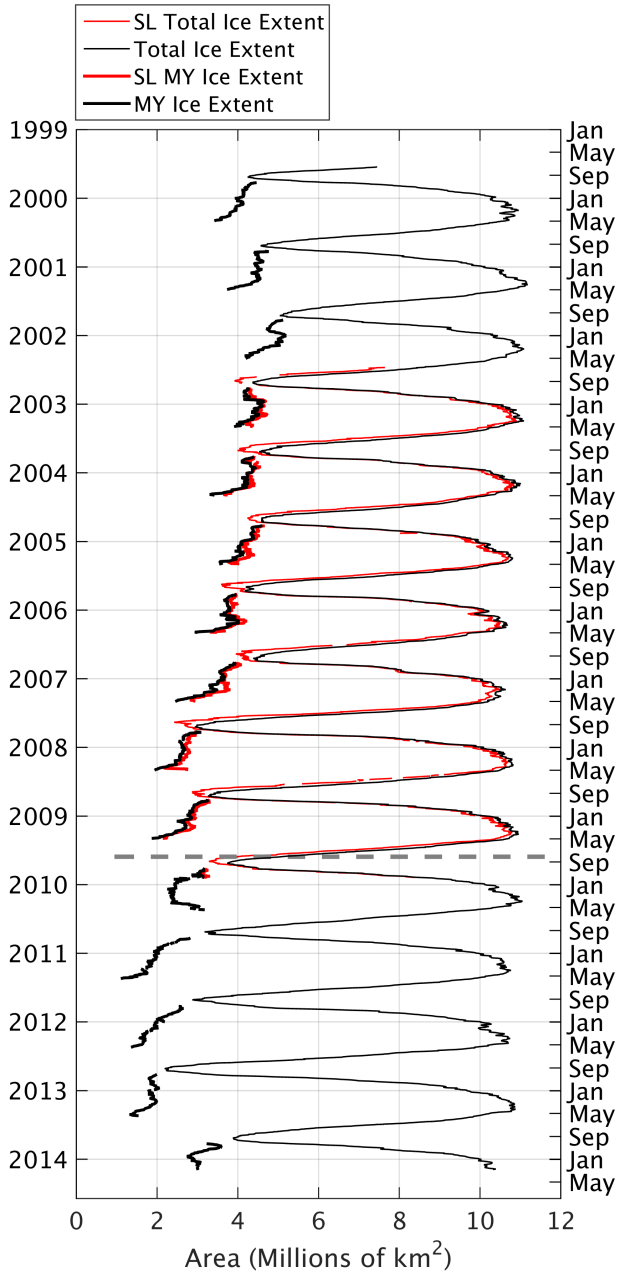

Figure 2.10: Plot of total Arctic ice area and MY ice area derived from QuikSCAT and OSCAT. The total area of Arctic ice extent is shown by the thin red and black lines. The thin black line indicates ice extent calculated using the NASA Team ice concentration product. The thin red line indicates the ice extent calculated using the SL method of applying a brightness temperature threshold to data from AMSR-E. Area of MY ice is shown by the thick red and black lines. The thick red line indicates area of MY ice classified using the SL algorithm. The thick black line indicates MY ice classified using QuikSCAT or OSCAT and the modified SL algorithm. MY ice for years above the dashed gray line is classified with QuikSCAT, while for years below it is classified with OSCAT.

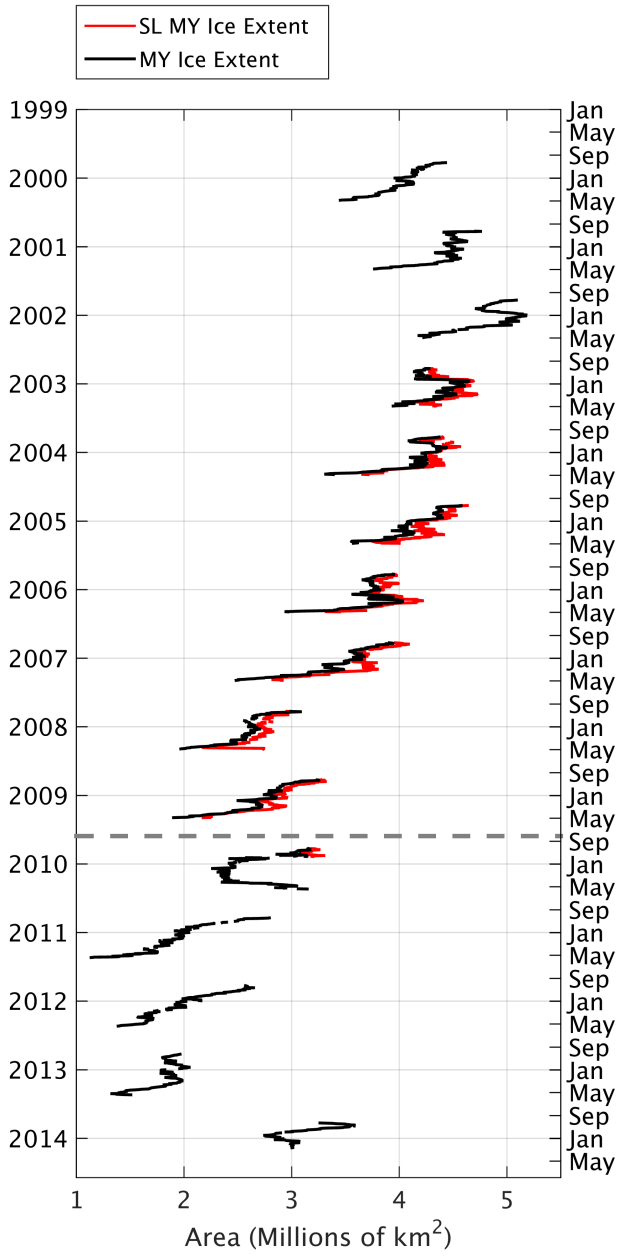

Figure 2.11: Plot of MY ice area derived from QuikSCAT and OSCAT. Area of MY ice is shown by the thick red and black lines. The thick red line indicates area of MY ice classified using the SL algorithm. The thick black line indicates MY ice classified using QuikSCAT or OSCAT and the modified SL algorithm. MY ice for years above the dashed gray line is classified with QuikSCAT, while for years below it is classified with OSCAT.

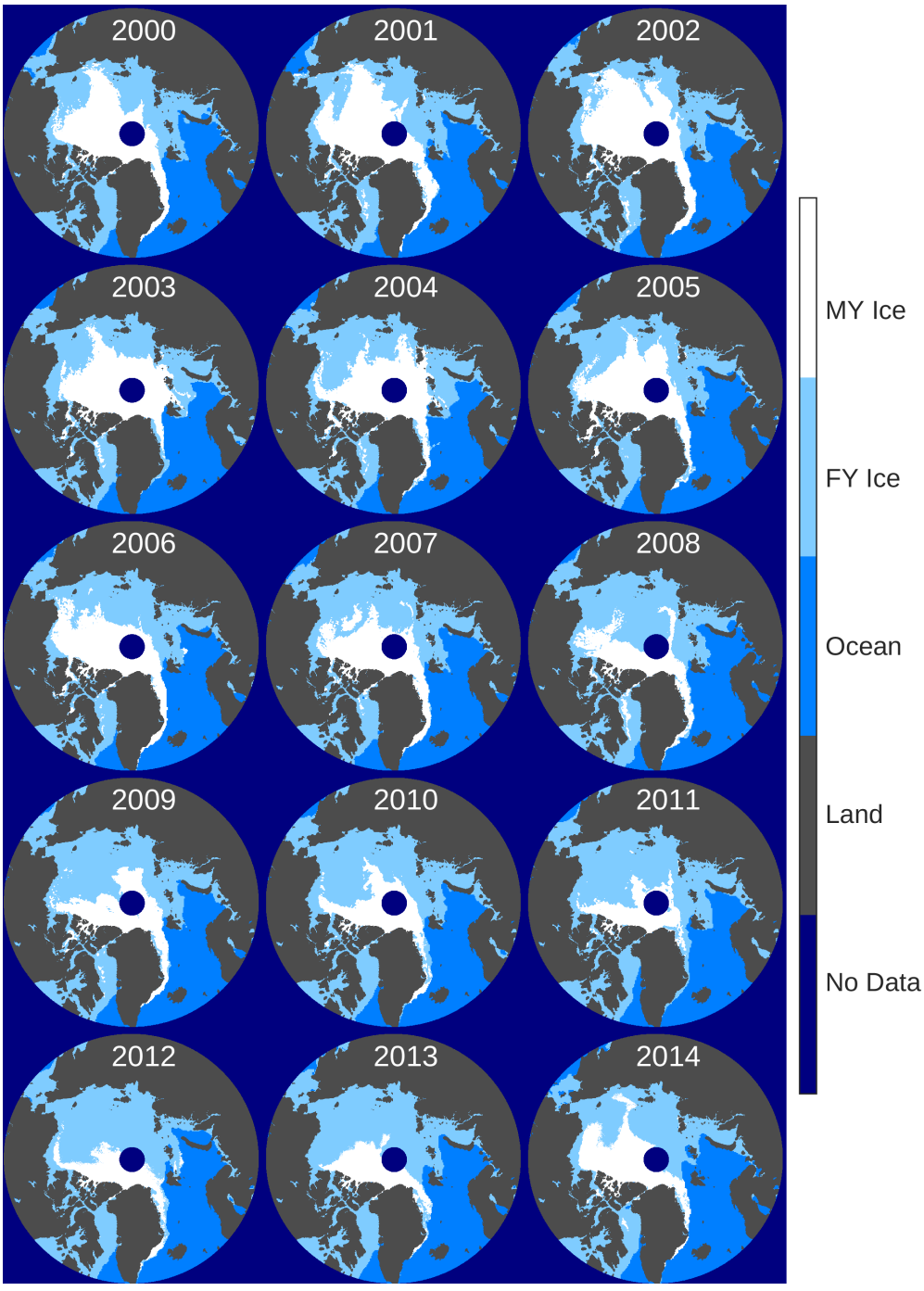

Figure 2.12: Maps of FY and MY ice, land, and ocean for DOY 45 from 2000 to 2014. The maps from 2000 to 2009 use data from QuikSCAT and maps from 2010 to 2014 use data from OSCAT.

Chapter 3

Ice Classification With ASCAT and SSMIS

The failure of the OSCAT sensor in 2014 and lack of a currently operational polar-orbiting Ku-band active sensor with readily available data motivates the use of the C-band ASCAT-A sensor to continue ice classification for years after 2014. ASCAT-A was launched in 2006 on the MetOp-A satellite and continues to operate; its successor, ASCAT-B, was launched in 2012 on the MetOp-B satellite, and ASCAT-C is scheduled for launch in a few years on MetOp-C.

Unfortunately, the lower frequency of the ASCAT sensor compared to OSCAT or QuikSCAT results in σ^0 measurements that are less sensitive to differences between FY and MY ice. To compensate for the decreased sensitivity, we exploit data from the 19 GHz and 37 GHz of the Special Sensor Microwave Imager Sounder (SSMIS) aid in distinguishing distributions of FY and MY ice.

This chapter describes how a combination of ASCAT and SSMIS data can be used to classify FY and MY ice in the Arctic using a Bayesian estimator. The sensors and data sources are described, the ice classification algorithm is detailed, and results are discussed.

3.1 Methodology

The backscatter properties of sea ice at Ku-band result in a bimodal distribution of σ^0 measurements over the Arctic with the distribution modes representing FY and MY ice occurring between approximately -25 and -18 dB and -12 and -10 dB, respectively [2]. To illustrate the separation of FY and MY ice at Ku-band and C-band, time series of daily σ^0 histograms from resolution enhanced QuikSCAT and ASCAT data at 40 degrees incidence angle are shown in Fig. 3.1. The data are obtained from the Scatterometer Climate Record Pathfinder [30]. Histograms of σ^0 are produced for each day and concatenated together to create the time series. Only Arctic σ^0 values from within the sea ice extent are used,

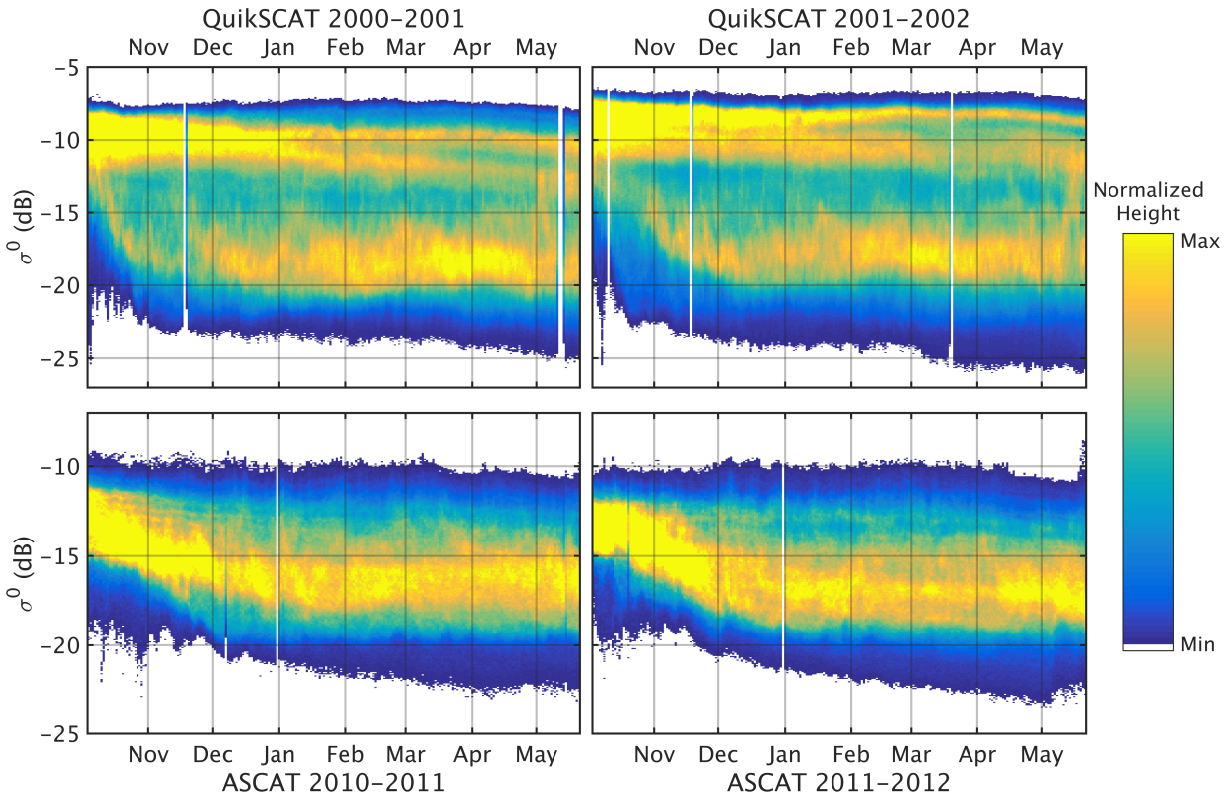

Figure 3.1: Multiyear average of a time series of daily histograms for ASCAT (from 2009 to 2014) and QuikSCAT (from 1999 to 2009). The QuikSCAT distribution demonstrates the separation between modes corresponding to FY ice and MY ice whereas the ASCAT distribution does not clearly demonstrate such separation. Each histogram in the time series has been normalized by its maximum bin count.

as identified by a 40% threshold on a daily NASA Team sea ice concentration product [1]. Data are shown for the winters of 2000/2001 and 2001/2002 for QuikSCAT and 2010/2011 and 2011/2012 for ASCAT.

In the figure, the backscatter distributions are shown from day of year 287 to 141 of the next year. Classifications of sea ice are completed for days 284 to 134 of the next year; they are not completed during the summer melt because the backscatter signatures of FY and MY ice become similar, resulting in poor ice classification results. In the QuikSCAT histograms, regions of high bin count for σ^0 greater than -12 dB and less than -17 dB can be identified and correspond to distributions of MY and FY ice, respectively [2, 13].

The QuikSCAT and OSCAT ice classifications [13] use a threshold fitted to a minimum histogram bin count between FY and MY ice distributions in a time series of histograms (as in Fig. 3.1) to classify ice as FY or MY. In this classification scheme, pixels with σ^0 measurements above the threshold are classified as MY ice, and those with measurements below the threshold are classified as FY ice. While a region of minimum bin count between the two modes can be easily observed in the QuikSCAT histograms, in the ASCAT histograms, two separate regions of high bin count are not as easily identifiable. As distributions of MY and FY ice are not as separated in the ASCAT histograms as in the QuikSCAT histograms, the thresholding method used to classify FY and MY with QuikSCAT and OSCAT ice may not be as effective with ASCAT. Rather than continuing the QuikSCAT/OSCAT ice classification record with ASCAT using the same classification methodology as [13], we show how a Bayesian classification algorithm which uses data from ASCAT and SSMIS can be used to classify ice type.

3.1.1 Sensor Information

A summary of the characteristics of the ASCAT and SSMIS sensors is shown in Table 3.1. The ASCAT sensor is a fan beam scatterometer launched in 2006 into a sun-synchronous near-polar orbit. It operates at 5.255 GHz (C-band) and continues to deliver near-global daily coverage. The SSMIS sensor is a passive microwave radiometer and was launched aboard the Defense Meteorological Satellite Program (DMSP) F-16, F-17, and F-18 platforms in 2003, 2006, and 2009. SSMIS operates at 24 different frequency channels and can collect atmospheric temperature measurements and brightness temperature measurements at a number of different polarizations and frequencies. In this study, data from SSMIS aboard the F-17 platform are used because it provides measurements for the full period of the ASCAT mission.

3.1.2 Sensors and Data Sources

The new classification method is completed using data from ASCAT and from the 19 GHz H-polarization (HH) and 37 GHz V-polarization (VV) channels of SSMIS. The choice of frequency channels is motivated by the use of these channels in the NASA team algorithm

Table 3.1: Characteristics of ASCAT and SSMIS

Parameter	**ASCAT**	**SSMIS**
Organization	European Organization for the Exploitation of Meteorological Satellites (EUMETSAT)	Defense Meteorological Satellite Program (DMSP)
Frequency Channels	5.255 GHz	19.35, 22.235, 37, 50.3, 52.8, 53.596, 54.4, 55.5, 57.29, 59.4, 63.28, 60.79, 91.665, 150, 183.311 GHz
Orbital Period	101 minutes	102 minutes (F-17)
Orbital Inclination	98.7°	98.8°
Ascending Node Local Time	9:30 p.m.	5:31 p.m.
Satellite Altitude	817 km	850 km
Start Date	October 19, 2006	November, 04 2006
Incidence Angle	Various	53.1 degrees
Swath Width	500 km	1707 km
Image Resolution	4.45 km/pixel	25 km/pixel

[31] and to provide more information for the Bayesian classification algorithm. The 19 GHz VV channel is also used in the NASA team algorithm; however, the brightness temperature separation between FY and MY ice at this channel is not as great as that of the other two channels, therefore we choose to omit the 19 GHz VV channel. Brightness temperature measurements for known areas of FY and MY ice are referred to ice "tie-points" in the algorithm and are shown in Table 3.2 [31]. The table shows that the brightness temperatures of FY and MY ice are separated by approximately 66.5 K for 37 GHz VV, 38.9 K for 19 GHz HH, and by 35 K for 19 GHz VV.

SSMIS data are obtained from the National Snow and Ice Data Center (NSIDC) [32], which provides daily average Arctic brightness temperature images on a 25×25 km/pixel resolution grid in a polar stereographic projection. To improve the detection of high-resolution features in the FY and MY ice classifications, we incorporate the enhanced resolution ASCAT data [30] and interpolate the SSMIS data onto the ASCAT 4.45×4.45 km/pixel grid in the polar stereographic projection. The combination of low-resolution radiometer

Table 3.2: NASA Team Tie Points

Frequency	Polarization	Ice Type	Brightness Temperature
19 GHz	V	FY	258.2 K
		MY	223.2 K
	H	FY	242.8 K
		MY	203.9 K
37 GHz	V	FY	252.8 K
		MY	186.3 K

data and high-resolution active microwave data have previously been used to classify sea ice [33, 34, 35].

ASCAT enhanced-resolution data are obtained from the Scatterometer Climate Record Pathfinder [30], which provides daily postings of two-day averaged ASCAT Arctic σ^0 data normalized to 40 degrees incidence angle and gridded at 4.45 $\times$ 4.45 km/pixel resolution in a polar stereographic projection. The enhanced resolution data are produced using the Scatterometer Image Reconstruction (SIR) algorithm [36], a modified algebraic image reconstruction technique which employs the sampling geometry and spatial response function (SRF) of the ASCAT sensor [19]. The SRF describes the contribution of each area within the antenna footprint to the measured value of σ^0. Each ASCAT measurement represents an integration of σ^0 weighted by the spatial response function over the area illuminated by the antenna. For a fine pixel grid, the area illuminated by the antenna encompasses multiple pixels, so if the SRF is known for a given measurement, information about multiple pixel values can be inferred from the single measurement. The SIR algorithm exploits knowledge of the ASCAT spatial response function to reconstruct σ^0 onto a fine pixel grid.

The two-day averaged reconstructed ASCAT data provide full coverage of the Arctic. As multiple passes of data are required, it is assumed that the backscatter should not change substantially over the time the measurements are taken.

Example Arctic sea ice data from ASCAT and SSMIS for day of year 61, 2011 are shown in Fig. 3.2. The main areas of MY ice can be visually identified by locating areas

containing higher σ^0 values and lower brightness temperatures compared to the rest of the ice extent.

Following the QuikSCAT/OSCAT classification scheme [13], the area of classification is restricted to within the ice extent by applying a 40% threshold to a daily NASA Team ice concentration product [1]. The NASA Team product was selected because of its consistent performance [37] and the long time series of available data, which continue to be published. Data from pixels in the ASCAT and SSMIS 19 GHz and 37 GHz products which fall within the 40% ice extent are collocated and classified as FY or MY. Classification is completed using a Bayesian estimator and *a priori* probabilities from either the QuikSCAT/OSCAT classification product or previous ASCAT/SSMIS classifications if they are available.

3.1.3 Comparison Datasets

The classification results are compared to classifications of MY and FY ice from two datasets: the EASE-Grid Sea Ice Age dataset [38], and the Canadian Ice Service (CIS) Arctic Regional Sea Ice Charts [39]. Both datasets are provided by the NSIDC.

The EASE-Grid Sea Ice Age dataset is produced from 1979 onward and reports the age of sea ice in years on a 12.5 $\times$ 12.5 km/pixel Equal-Area Scalable Earth (EASE) grid. The ice age estimates are produced using sea ice motion vectors derived from a Lagrangian tracking procedure [40]. Over the time extent of the dataset, the ice motion vectors are produced using data from the Special Sensor Microwave/Imager (SSM/I), the Scanning Multichannel Microwave Radiometer, the Advanced Very High Resolution Radiometer, and from drifting buoys from the International Arctic Buoy program [40]. The trajectories of grid cells containing ice are estimated over the years, and the age of tracked ice is recorded.

An analysis of tracking error has been completed by Kwok et al., who use motion vectors derived from SSM/I data to track ice parcels and compare the estimated trajectories to buoy motion trajectories and trajectories derived from SAR data [41]. They find the location error to be approximately 5 to 12 km per day; the errors do not necessarily accumulate, as annual location error is on the order of 50-100 km [41]. We use the EASE-Grid Sea Ice Age product with the ASCAT/SSMIS classifications to compare the total extent of pixels

classified as MY or FY ice. As the comparison deals with extent rather than location, it should be relatively insensitive to the errors in ice location tracking.

The CIS charts are prepared by the Canadian Ice Service and are typically available at weekly intervals from the year 2006 onward. Each ice chart is prepared manually from inspection of *in situ* observations from land, ship and aircraft, and from satellite and aerial reconnaissance data. Charts are prepared with data from up to 72 hours prior to the reported date.

Ice charts are produced for different regions of the Canadian Arctic, including the Western Arctic, Eastern Arctic, the Hudson bay, the Great Lakes, and the East Coast. As the Western Arctic region has the most overlap with the ASCAT/SSMIS classifications, it is selected for comparison.

Various characteristics of ice are reported in the charts, including the total ice concentration, ice form, and stage of development. In each region, the charts outline subregions of approximately homogeneous ice properties. Total ice concentration is reported, as well as properties of the three most prominent ice types: the partial ice concentration, the stage of development or thickness, and the ice form or floe size. The sum of the three reported partial ice concentrations is always less than or equal to the reported total ice concentration.

To compare the ASCAT/SSMIS classifications to the CIS charts, we identify areas of total ice concentration greater than 40% in the CIS charts and follow the procedure of Swan and Long [2]. All ice stages having survived at least one melt season in the CIS charts (second-year ice, MY ice, and old ice) are grouped as MY ice, while all other ice types are grouped as FY ice. For each subregion detailed in a given CIS chart, the three ice types are identified as FY or MY ice and their concentrations are summed to determine a FY and MY ice concentration. The ASCAT/SSMIS classifications can then be compared to the CIS chart subregions, and the MY and FY ice concentrations are observed for which ice is typically classified as FY or MY using ASCAT/SSMIS.

3.1.4 ASCAT/SSMIS Classification

The classification of FY and MY ice with ASCAT and SSMIS uses a Bayesian decision model. The classification is completed by iterating over all pixels within the ice extent and

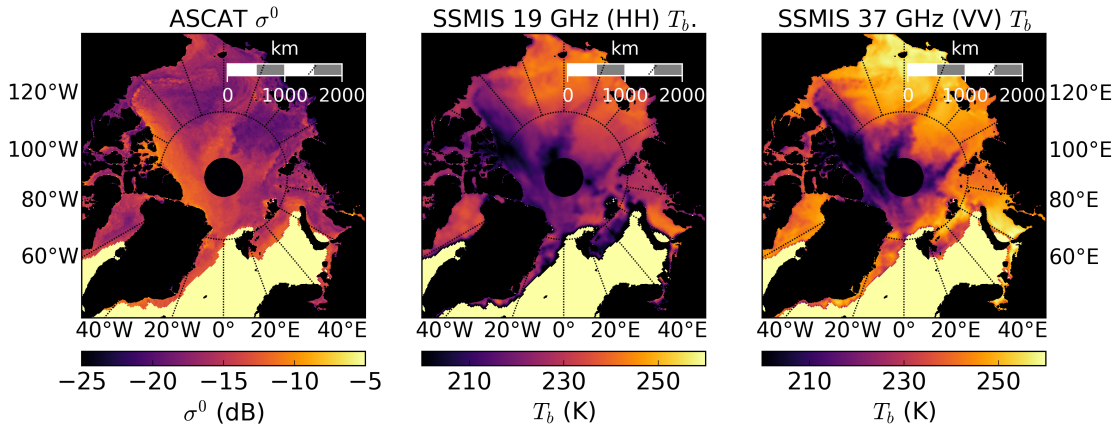

Figure 3.2: Example images of ASCAT σ^0 values and reported brightness temperatures for day of year 61, 2011 from the 19 GHz (HH) and 37 GHz (VV) channels of SSMIS over the Arctic. Areas of open water and land are masked as light yellow or black, respectively. The areas of MY ice correspond generally to the areas of high σ^0 values and low brightness temperature (T_b) values.

using the decision model to select FY or MY ice. The input to the decision function is a measurement column vector, $\boldsymbol{x}$, which is given as

$$\boldsymbol{x} = [\text{ASCAT}_{\sigma^0}, \text{SSMIS}_{19}, \text{SSMIS}_{37}]^T, \tag{3.1}$$

where $\boldsymbol{x}$ consists of an ASCAT σ^0 measurement and SSMIS 19 GHz and 37 GHz brightness temperature measurements, all from the same day and pixel.

The Bayesian classification decides whether the probability of FY ice (I_{FY}) given the measurement vector $\boldsymbol{x}$ is greater than the probability of MY ice (I_{MY}) given $\boldsymbol{x}$, or

$$\text{P}(I_{MY}|\boldsymbol{x}) \gtrless \text{P}(I_{FY}|\boldsymbol{x}). \tag{3.2}$$

Using Bayes' rule, an equivalent decision is derived in terms of the FY and MY ice distributions: the probabilities of $\boldsymbol{x}$ given $\boldsymbol{x}$ is FY or MY ice, or

$$\text{P}(\boldsymbol{x}|I_{MY})\text{P}(I_{MY}) \gtrless \text{P}(\boldsymbol{x}|I_{FY})\text{P}(I_{FY}), \tag{3.3}$$

which can be practically implemented.

The multivariate normal expression used for the probabilistic model is given as

$$f(\boldsymbol{x}) = \frac{1}{\sqrt{(2\pi)^3|\boldsymbol{S}|}} e^{-\frac{1}{2}(\boldsymbol{x}-\boldsymbol{\mu}^T)\boldsymbol{S}^{-1}(\boldsymbol{x}-\boldsymbol{\mu})}, \tag{3.4}$$

where $\boldsymbol{S}$ is the data covariance matrix, $|\boldsymbol{S}|$ is the determinant of $\boldsymbol{S}$, and $\boldsymbol{\mu}$ is the mean vector. The probabilities $\mathrm{P}(\boldsymbol{x}|I_{FY})$ and $\mathrm{P}(\boldsymbol{x}|I_{MY})$ are determined by evaluating $f(\boldsymbol{x})$ where $\boldsymbol{S}$ and $\boldsymbol{\mu}$ are estimated for FY and MY ice from σ^0 and brightness temperature measurements of FY and MY ice.

The distributions of FY and MY ice can be observed by visually inspecting scatterplots of brightness temperature and σ^0 values from the sensors. Joint scatterplots/2-D histograms are shown in Fig. 3.3 for data from day of year 61, 2011. The joint scatterplots/2-D histograms plot SSMIS 19 GHz versus SSMIS 37 GHz data points and ASCAT σ^0 versus SSMIS 37 GHz data points. In areas where the scatterplot point density is too great to be able to discern individual points, a 2-D histogram is used. The distributions of FY and MY ice are also plotted, using the OSCAT ice type classifications to identify pixels corresponding to FY or MY ice [13]. The plots show that distributions of FY and MY ice are moderately separated, motivating the use of the Bayesian decision model for classification. In areas where the distributions of FY and MY ice overlap, misclassifications of ice are more likely to occur. Also, FY ice measurements which fall in the region of low brightness temperature and high backscatter are likely to be misclassified as MY ice. Measurement noise and high backscatter from FY ice with rough surface features can contribute to such misclassifications.

The first ice classifications are processed for day of year 284, 2009 using the QuikSCAT classifications [13] to identify the areas of FY and MY ice in the ASCAT and SSMIS data. Areas of FY and MY ice are identified for days 284 to 289, 2009, and the mean and covariance values of the FY and MY ice measurement vectors are calculated using these five days of data to initialize the processing. The probabilities of FY and MY ice ($P(I_{FY})$ and $P(I_{MY})$) are also calculated from these data by calculating number of pixels classified as FY or MY ice divided by the total number of pixels within the ice extent.

Using the calculated mean, covariance values, and probability values, ice is first classified for day of year 284, 2009 using the ASCAT/SSMIS data. Completed classifications are

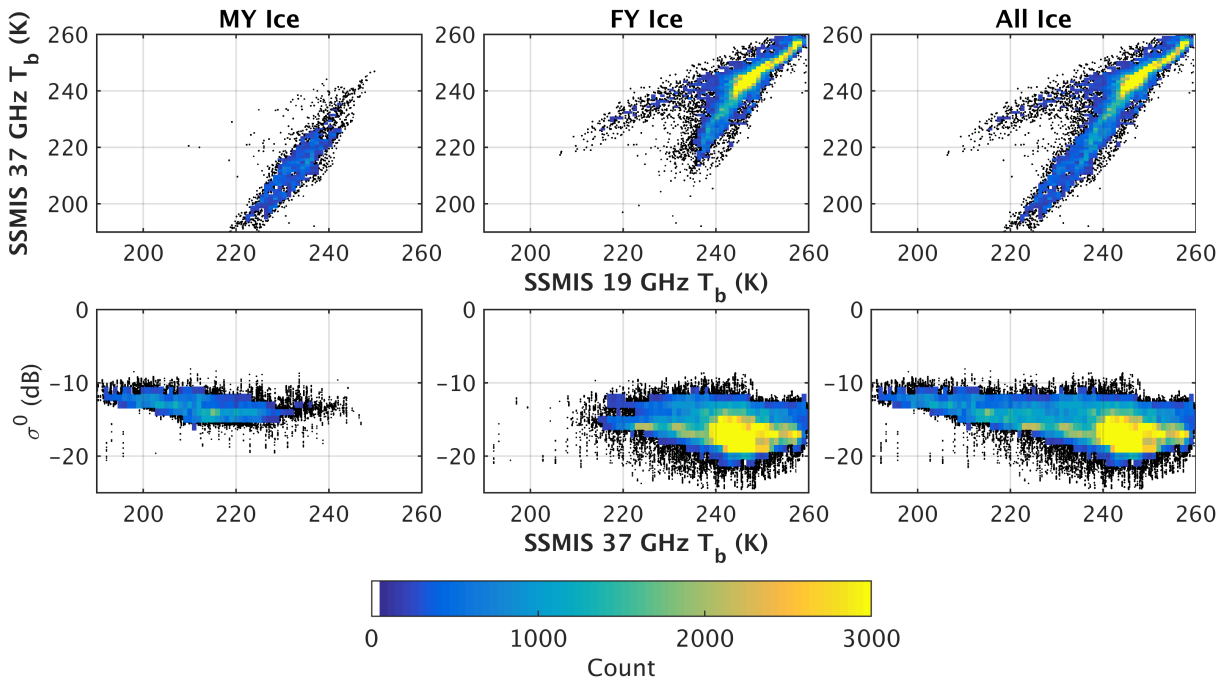

Figure 3.3: Joint scatterplots/2-D histograms of ASCAT σ^0 values and SSMIS reported brightness temperatures (T_b) for day of year 61, 2011. When the density of the scatterplot becomes too great to be able to discern individual points, the density is shown in a 2-D histogram. For the 2-D histogram, bin sizes are 1 K by 1 K for the top row of plots and 1 dB by 1 K for the bottom row of plots. Plots for the sea ice extent and distributions of FY and MY ice are shown. The distributions of FY and MY ice are derived using the OSCAT ice type classifications [13]. Unlike for Ku-band, the C-band FY and MY distributions show only moderate separation from each other.

used to recalculate the mean, covariance, and probability values for FY and MY ice, and an average of the calculated statistics for the 5 previously classified days are used for successive classifications. After the first five classifications are completed, the statistics used to initialize classifications for day of year 284 are no longer used. At that point, classifications rely on the statistics generated from the classifications for days after day 284. On day of year 284 for years after 2009, this process is repeated, except ASCAT/SSMIS data and classifications from the previous year are used to initialize the statistics and probabilities. As ice is not classified during the summer melt, and classifications begin on day of year 284, we choose to use the prior year's statistical and probabilistic data, or *a priori* data, to re-initialize the processing.

Some days in the ASCAT and SSMIS datasets have gaps or are missing data. Data from these days are not used to update the *a priori* data used for classification. Instead, subsequent classifications rely on the *a priori* data from the 5 previously completed classifications where no data was missing.

The ASCAT sensor is sensitive to areas of rough or broken ice, and the backscatter signatures of such areas can appear similar to backscatter from MY ice. The addition of SSMIS brightness temperature data to the classification algorithm helps to mitigate misclassifications of MY ice around areas of fragmented ice, but does not entirely remove such misclassifications. Occasionally, the Bayesian decision model classifies ice as MY in areas which are distant from the main area of MY ice and which are classified as FY in previous days. Conversely, areas which are located in the main area of MY ice and are classified as MY ice in previous days are occasionally classified as FY.

To mitigate the apparent misclassifications, cost functions, C_{FY} and C_{MY}, are introduced to the Bayesian decision model and updated for each day of classification. The main areas of MY ice are identified by selecting all pixels that fall approximately 65 km away from boundaries of FY and MY ice. Main areas of FY ice are identified by selecting all pixels approximately 65 km away from the same boundary. The 65 km distance on each side of the FY/MY ice boundary is assumed to adequately allow for possible movement of areas of FY and MY ice from day to day. For the initial classification (before boundaries of FY and MY ice are known), the cost functions are set to a value of one and have no effect on the classifications.

After the initial classification, the cost function C_{MY} is set to a high value (near unity) for pixels solidly within the area of MY ice. For areas within the main area of FY ice, C_{MY} is set to a low value (near zero). The cost function C_{FY} is set in a similar fashion for pixels solidly within and without areas of FY ice. For areas near the FY/MY boundary, the cost functions take on a value of one, and so have no effect. The cost functions are binary, and so only take on one of the two values for a given pixel. With the addition of the cost functions, the Bayesian decision model becomes

$$\mathrm{P}(\boldsymbol{x}|I_{MY})\mathrm{P}(I_{MY})C_{MY} \gtrless \mathrm{P}(\boldsymbol{x}|I_{FY})\mathrm{P}(I_{FY})C_{FY}. \tag{3.5}$$

At the interface between sea ice and open water, ocean dynamics can result in rough, broken patches of sea ice, leading to areas of increased backscatter near the ice edge. Areas of MY ice are typically characterized by greater backscatter levels than FY ice, and so high backscatter levels from ocean regions near the ice edge can result in erroneous MY ice classification. Whereas true MY ice should persist until a melt, spuriously classified areas of MY ice near the sea ice edge typically appear and then disappear after a few days. To suppress such misclassified areas of MY ice, we employ a correction algorithm which reclassifies MY ice to FY in areas where transient MY ice appears near the ice edge, outside the main body of MY ice [13]. The correction algorithm first identifies the area of classified MY ice from a previous day's classifications and creates a MY ice mask. The mask of MY ice is dilated to account for movement of the MY ice edge and compared with the next day's MY ice classifications. Areas of classified MY ice which appear outside of the mask are assumed to be misclassified and are reclassified as FY ice. The process then repeats with a new MY ice mask for the next day of data. The first MY ice mask is initialized using the area of MY ice common to the first three days of classification. The algorithm effectively removes most areas of misclassified MY ice near the sea ice edge [13].

3.2 Results and Discussion

The decision model is applied to data for the years 2009 to 2014 to create classification images for each day. The ASCAT/SSMIS classifications are compared to the OSCAT classifications [13], the CIS charts [39], and the EASE-Grid Sea Ice Age dataset [38]. Using the CIS charts, typical concentrations of MY ice are found for which ice is classified as MY with ASCAT/SSMIS. A time series analysis of minimum total ice extent and MY ice extent is also completed using extent data from the ASCAT/SSMIS classifications, OSCAT classifications, and the EASE-Grid Sea Ice Age dataset [38]. Extent data are also included for classifications processed using the same methodology as the ASCAT/SSMIS classifications, but only using SSMIS data for comparison.

Example classification images for day of year 3 of years 2010, 2011, and 2012 are shown in Fig. 3.4 and are representative of typical classification results. The images provide a comparison to OSCAT classifications for the same days. Some differences are apparent

between the ASCAT/SSMIS classifications and the OSCAT classifications. Despite the correction algorithm, the OSCAT classifications classify a patch of ice near the sea ice edge as MY in the 2012 image. When areas of high backscatter near the ice edge persist for several days, the effectiveness of the correction algorithm is decreased [13]. The inclusion of the passive microwave data in the ASCAT/SSMIS classifications helps to mitigate such patches of spuriously classified MY ice.

Typically, the ASCAT/SSMIS classifications of MY ice extend beyond the area classified with OSCAT, except near the east coast of Greenland. As shown in Fig. 3.4, in the year 2012, ice which advects south along the east coast of Greenland into the Atlantic ocean is not classified as MY using ASCAT/SSMIS, but is classified as MY using OSCAT. For the same day in 2010, however, most ice in the same area is classified as MY with both ASCAT/SSMIS and OSCAT. This discrepancy is due to the limited ability of the ASCAT/SSMIS classification method to track discrete parcels of MY ice which drift south along the east coast of Greenland. As MY ice drifts along the east coast of Greenland further from the main body of MY ice, the classified MY ice parcels can become fragmented (like those closest to the southern tip of Greenland in the 2012 image) and become less likely, due to the cost functions of the classification algorithm, to be classified as MY ice. If the MY ice which moves along the Greenland coast is continuous in area, it typically remains classified as MY ice, as in the 2010 image.

The difference in MY ice classification extent along most of the MY/FY ice boundary may be due to a difference in the sensitivity of the classification algorithms to different concentrations of MY ice. To determine the typical concentration of MY ice for which an area of ice is classified as MY using ASCAT/SSMIS, we compare the ASCAT/SSMIS classifications to the CIS charts.

3.2.1 CIS Chart Comparison

The ASCAT/SSMIS classifications are compared to the CIS charts for the region of the Western Arctic. Fig. 3.5 shows the ASCAT/SSMIS classifications for day of year 2, 2011 and the same classifications with the CIS chart classifications from day of year 3, 2011 overlaid. As data for up to 72 hours prior to the reported date are used to create the

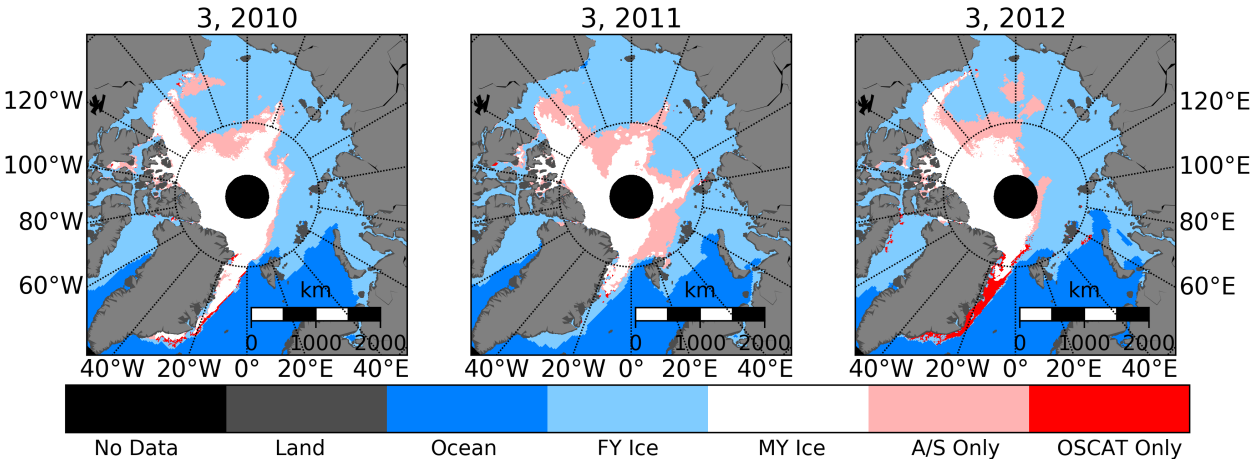

Figure 3.4: Example ice classification images from day of year 3 for years 2010, 2011, and 2012. The ASCAT/SSMIS classifications are compared to the OSCAT classifications and the differences are highlighted. Areas classified as MY in the ASCAT/SSMIS classifications but not by OSCAT are highlighted in pink. Areas classified as MY in the OSCAT classifications but not by ASCAT/SSMIS are highlighted in red.

CIS charts, we choose a single-day offset for the comparison. In the figure, the CIS chart data indicate the percent concentration of MY ice derived from summing reported percent concentrations of 2nd-year ice, MY ice, and old ice. The areas of same MY ice concentration in the CIS chart overlay are identified by a red outline. Visual comparison of the plots shows that the ASCAT/SSMIS classifications of MY ice correspond to areas of approximately 50% MY ice concentration or greater as indicated by the CIS chart data.

CIS chart data from 2010, 2011, and 2012 are used to further analyze the percent FY/MY ice concentration at which ice is classified as MY using ASCAT/SSMIS. For days on which both ASCAT/SSMIS classifications and CIS chart classifications are available, pixels classified as MY ice using ASCAT/SSMIS are collocated with the CIS chart classifications of percent MY ice concentration to produce a histogram of ASCAT/SSMIS MY ice pixel count versus CIS chart percent MY ice concentration. The study is repeated for ice classified as FY using ASCAT/SSMIS. The resulting histograms are shown in Fig. 3.6. The histograms show that for most pixels classified as MY ice using ASCAT/SSMIS, the corresponding CIS chart concentrations of MY and FY ice are approximately greater than 50% and less than 20%, respectively. For most pixels classified as FY ice using ASCAT/SSMIS, the corresponding

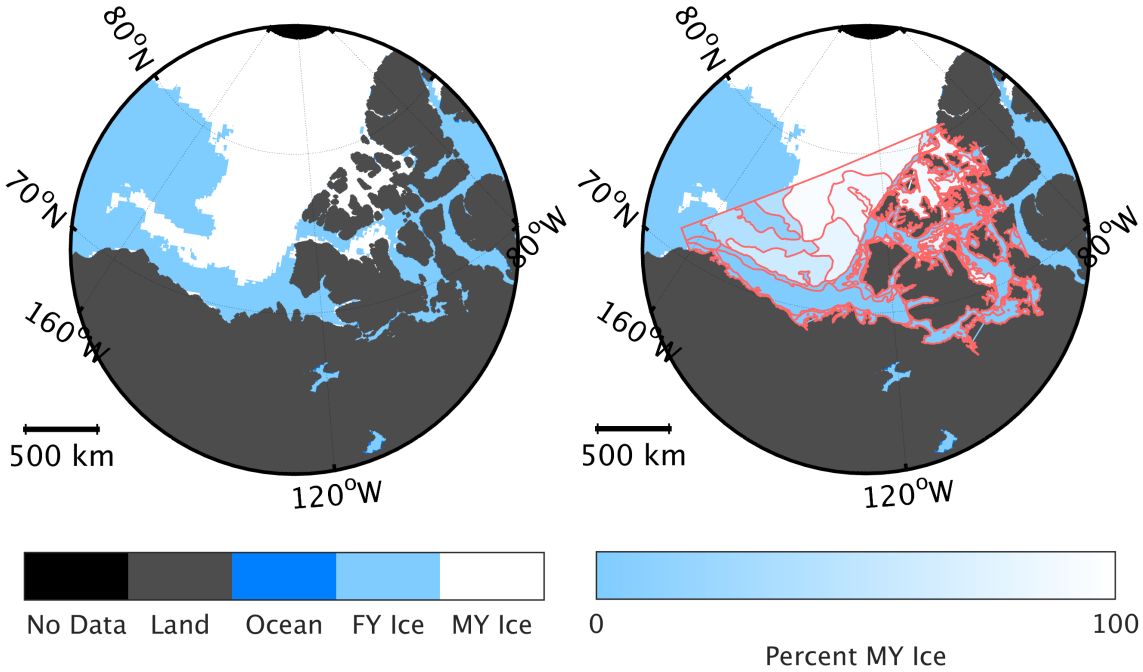

Figure 3.5: Images of ASCAT/SSMIS ice classifications for day of year 2, 2011 (left), and CIS chart classifications for day of year 3, 2011 overlaid on the ASCAT/SSMIS classifications (right). The data dates are offset because CIS charts are constructed using data retrieved up to 72 hours prior to the reported date. In the right image, areas of the same CIS chart classification are enclosed by a red line.

CIS chart concentrations are approximately greater than 90% and less than 10% for FY ice and MY ice, respectively.

3.2.2 Ice Extent Time Series

A time series of total ice extent and MY ice extent from ASCAT/SSMIS, SSMIS only, OSCAT, and the EASE-Grid Sea Ice Age datasets is shown in Fig. 3.7. In each case the MY ice extent is determined by summing the area of grid cells classified as MY ice. Similarly to [13], we do not include grid cells of the pole hole (black disc in Fig. 3.4), which extends from 87 to 90 degrees N latitude over an area of 364 thousand sq. km. The grid area for each pixel is determined using the Scatterometer Image Reconstruction grid area file for the north polar stereographic projection. The area file is available from the Scatterometer Climate Record Pathfinder FTP site [30]. We calculate the standard deviation of the MY ice extent values for ASCAT/SSMIS using a sliding window of 10 days of extent values. The

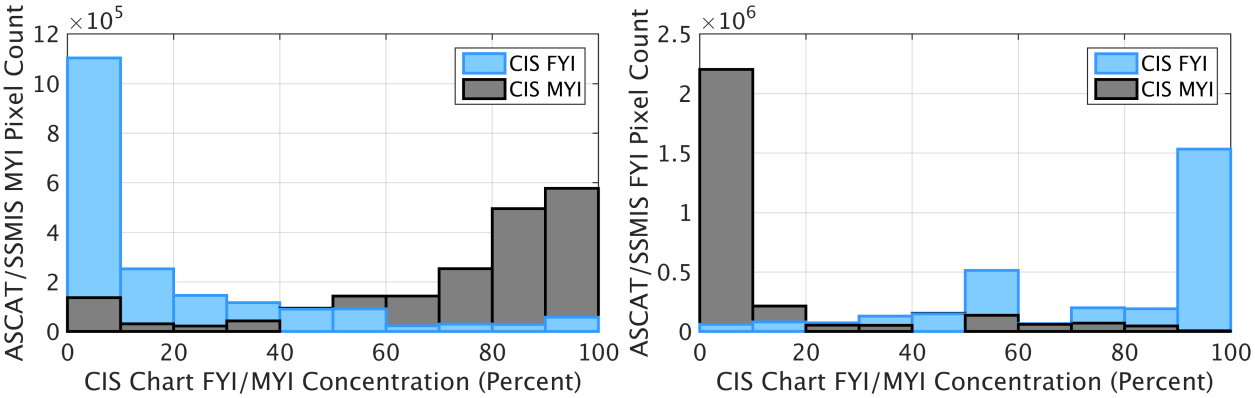

Figure 3.6: Histograms of pixel counts of ice classified as MY (left) and FY (right) using ASCAT/SSMIS versus the CIS chart percent concentrations of FY and MY ice. Most ASCAT/SSMIS pixels classified as MY ice (MYI) correspond to a MYI concentration of approximately 50% or greater and a FY ice (FYI) concentration of approximately 20% or less in the CIS charts. Most FYI classified pixels correspond to a FYI concentration of approximately 90% or greater and a MYI concentration of approximately 10% or less in the CIS charts.

standard deviation values are too small to be easily observed on the plot, and so are not included. The RMS value of the calculated standard deviations is 115 thousand sq. km.

In the EASE-Grid Sea Ice Age dataset, the age of sea ice is classified by year using integer values from one to ten. The EASE-Grid Sea Ice Age data are regridded to the ASCAT/SSMIS grid and MY ice areas of age two years or greater (EASE 2+) and three years or greater (EASE 3+) are identified by summing the area of all grid cells classified with a value of two or greater and three or greater. Again, grid cells within the pole hole are omitted. Both EASE-Grid Sea Ice Age groups are included for comparison with the ASCAT/SSMIS, SSMIS-only, and OSCAT ice classifications. We note that the EASE-Grid Sea Ice Age data are available only through 2012, so data for years after are not included.

In Fig. 3.7, the ASCAT/SSMIS classifications typically classify a greater extent of MY ice immediately after the melt season and then show greater agreement with the OSCAT classifications as the winter progresses. Occasionally at the beginning of winters, increases in MY ice extent appear, followed by a decrease. The MY ice extent increases during the beginning of winter could correspond to areas of high MY ice concentration becoming spread out as the sea ice extent increases rapidly, resulting in greater areas of diffuse MY ice, which continue to be classified as MY ice with ASCAT/SSMIS. Other factors which cause FY ice to

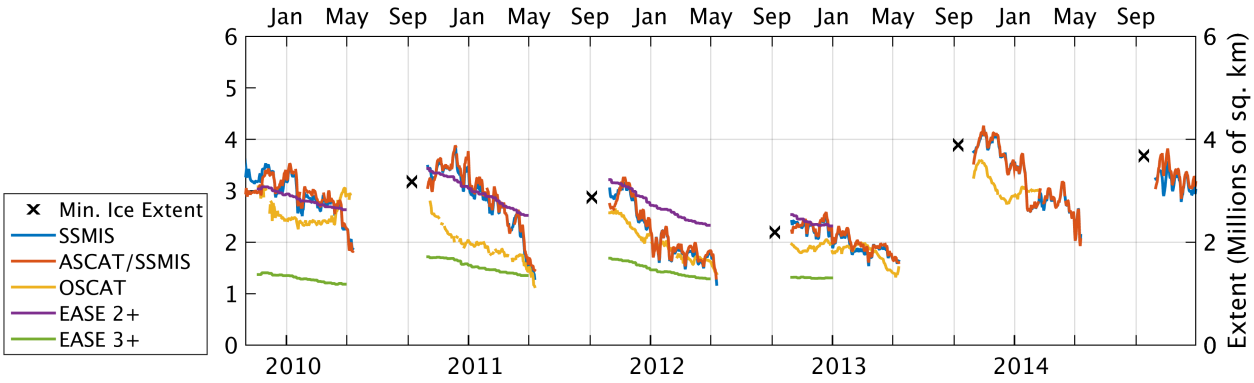

Figure 3.7: Time series of minimum total ice extent and MY ice extent. Plots are shown of the MY ice extent from SSMIS-only, ASCAT/SSMIS, and OSCAT ice classifications, as well as ice ages classified as greater than 1 year and greater than 2 years by the Ease-Grid Sea Ice Age dataset. The total ice extent minima are calculated using a 40% ice concentration ice edge as reported by a NASA Team ice concentration product [1]. The calculated RMS standard deviation for the ASCAT/SSMIS MY extent is 115 thousand sq. km.

appear similar to MY ice could contribute to an increased area of MY ice classification. Such factors include deformation of FY ice, which can increase σ^0 at C-band due to the increase in surface roughness, and deep snow, which can cause a decrease in brightness temperature at 19 GHz and 37 GHz [21].

The variability in the extent of the ASCAT/SSMIS classifications is likely caused by the changing parameters of the Bayesian classifier, which result in greater variation of the FY/MY boundary than for the ice motion vector tracking method of the EASE-Grid Sea Ice Age product, or the slowly varying backscatter threshold of the OSCAT classifications.

The SSMIS-only classifications appear very similar to the ASCAT/SSMIS classifications, which suggests that the passive data have a significant impact on the classification performance. A zoom-in comparison of classifications for day of year 2, 2011 in Fig. 3.8 shows a similar MY ice extent, but some finer resolution details are present in the ASCAT/SSMIS classifications which are not present in the SSMIS-only classifications.

The addition of SSMIS passive data is useful because it not only provides more information for the Bayesian classifier, but also helps to compensate for the sensitivity of ASCAT σ^0 to areas of broken ice near the ice edge and reduce misclassification of ice. Using ASCAT data alone results in large areas of misclassified ice near the ice edge that skew the Bayesian classification parameters as they are updated using previous classifications.

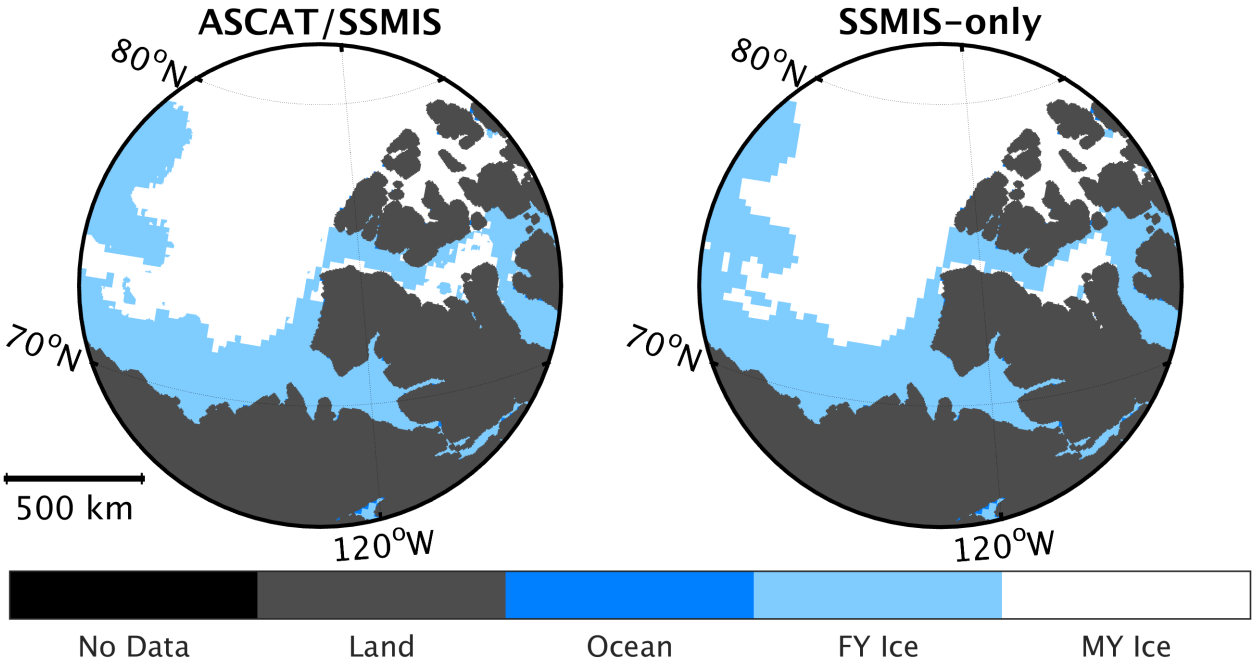

Figure 3.8: Zoom-in comparison of ASCAT/SSMIS and SSMIS-only ice classifications for day of year 2, 2011. In some areas, the ASCAT/SSMIS classifications contain finer details than the SSMIS classifications because of the inclusion of enhanced-resolution ASCAT data.

By reducing such misclassifications, the SSMIS data help to prevent a drift in error as the Bayesian classification parameters are updated.

A plot of the differences in MY ice extent between EASE 2+ and the ASCAT/SSMIS, SSMIS, and OSCAT classifications is shown in Fig. 3.9. In Fig. 3.10, differences are shown with respect to the EASE 3+ MY ice extent. The ASCAT/SSMIS MY ice extent generally stays within one million sq. km of the ice extent of EASE 2+, with an RMS difference of 372 thousand sq. km. The SSMIS-only classifications are similar, with an RMS MY extent difference of 373 thousand sq. km. When compared with the ice extent of EASE 3+, the OSCAT MY extent shows an RMS difference of 810 thousand sq. km. Finally, the RMS difference between the ASCAT/SSMIS and OSCAT MY ice extent is 622 thousand sq. km.

The total extent of MY ice appears to decrease from the winters of 2009 to 2013, followed by a recovery in 2014. Other studies have similarly reported a decline in MY ice [42, 13] and recovery in 2014 [43]. Total MY ice extent levels appear to follow roughly the same cycle from the winters of 2009 to 2013. Following the winter of 2013, MY ice extent

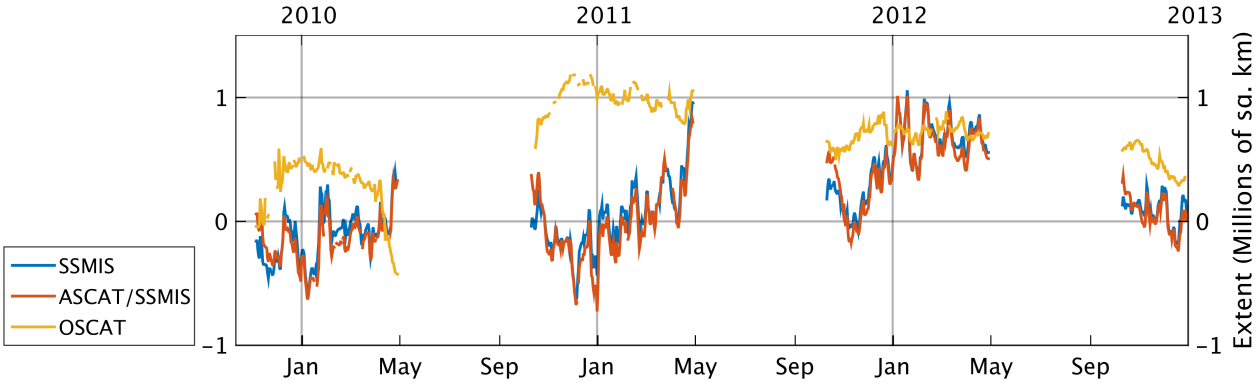

Figure 3.9: Time series of differences in total MY ice extent compared to extent of ice classified as age two years or greater in the EASE-Grid Sea Ice Age dataset (EASE 2+). Plots are shown for SSMIS, ASCAT/SSMIS, and OSCAT.

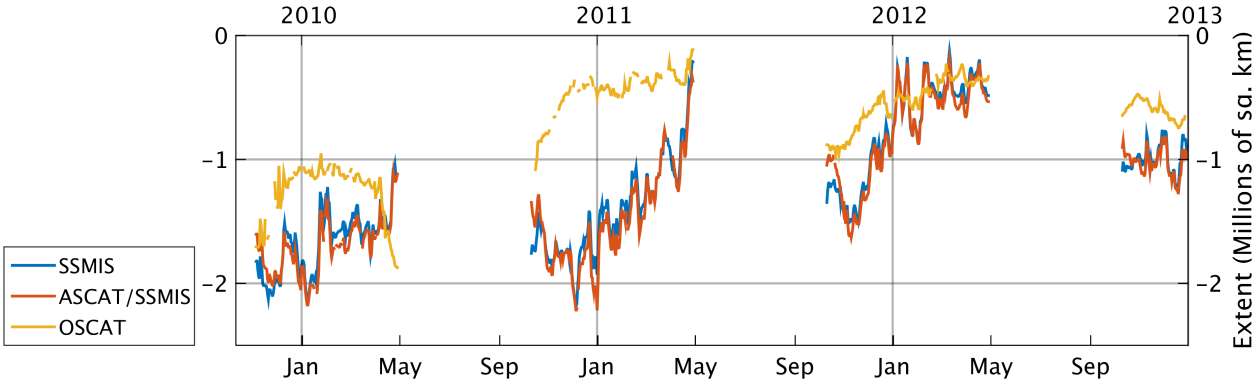

Figure 3.10: Time series of differences in total MY ice extent compared to extent of ice classified as age three years or greater in the EASE-Grid Sea Ice Age dataset (EASE 3+). Plots are shown for SSMIS, ASCAT/SSMIS, and OSCAT.

levels do not drop to the low levels observed in previous years (below 2 million sq. km), and vary from approximately 3 to 4 million sq. km during the majority of the winter.

3.3 Conclusion

Using a fusion of active and passive microwave data, FY and MY ice can be classified in the Arctic. Comparison of ASCAT/SSMIS classifications to the CIS charts shows that areas of approximately 50% or greater MY ice concentration in the CIS charts are typically classified as MY ice in the ASCAT/SSMIS classifications. The extent of classified MY ice in the ASCAT/SSMIS classifications shows general agreement with the extent of MY ice

classified as age 2 years or greater in the EASE-Grid Sea Ice Age product. Compared to the OSCAT ice classifications, the ASCAT/SSMIS classifications generally classify a greater area of MY ice, especially near the beginning of winter; this effect may be due to a number of phenomena, including the diffusion of high concentration areas of MY ice as the ice extent expands. The addition of the passive SSMIS data appears to improve classifications by mitigating misclassifications caused by ASCAT's sensitivity to rough patches of ice which can appear similar to, but are not, MY ice. As the ASCAT and SSMIS sensors continue to operate, future work could be done to reduce the variability in the MY ice extent of the classifications and to improve classification of discrete parcels of MY ice outside the main area of MY ice, especially those which sometimes appear near the east coast of Greenland.

Chapter 4

High-Resolution Soil Moisture Retrieval with ASCAT

Current soil moisture retrieval algorithms using the Advanced Scatterometer (ASCAT) have provided publicly available, global soil moisture data [3]. The ASCAT soil moisture products, however, do not exploit the high-resolution capabilities of the ASCAT sensor and report the data either on a 12.5 × 12.5 or 25 × 25 km/pixel grid. This chapter describes an algorithm for high resolution (4.45 × 4.45 km/pixel) soil moisture estimation using data from ASCAT.

4.1 Introduction

Various algorithms have been devised to use active and passive spaceborne sensors to estimate soil moisture levels [15, 14, 44, 18], and orbiting sensors can provide near-global estimates of soil moisture every few days. These sensors are generally able to measure soil moisture parameters despite cloud coverage and, in some cases, vegetation coverage of the target area. In the case of ASCAT, an active C-band sensor, the electromagnetic wavelength and scattering properties restrict soil moisture retrieval to the top few centimeters of the soil. ASCAT soil moisture products typically report surface soil moisture and models are used to estimate moisture in deeper soil layers [45].

Both 12.5 × 12.5 and 25 × 25 km/pixel resolution global soil moisture products are presently being produced with data from the ASCAT sensors aboard the Metop-A and Metop-B satellites. The products are processed using the WAter Retrieval Package (WARP) algorithm [3], which is based on a change detection algorithm developed at the Vienna University of Technology (TU-Wien) [18]. To produce an improved resolution product, we use the AVE algorithm to create higher resolution images (4.45 × 4.45 km/pixel) of the radar backscatter coefficient (σ^0) [19]. Exploiting ASCAT's high-resolution image capability enables higher resolution images of soil moisture than are currently available. By resolving

finer soil moisture features, the higher resolution soil moisture images could complement soil moisture-related studies in such areas as crop yield prediction, drought prediction and localization, and modeling of the water table and water cycle [5].

Interest in soil moisture retrieval has prompted the development and launch of satellite sensors designed primarily for soil moisture monitoring. For example, the ESA's Soil Moisture and Ocean Salinity sensor and NASA's Soil Moisture Active Passive sensor are specifically designed to provide accurate soil moisture estimates at reasonable spatial resolutions (approximately 50 km and 9 km) [17, 16]. When compared with ASCAT, such sensors can provide more accurate measurements of soil moisture in certain areas, especially arid regions [46]. However, comparison studies generally show that ASCAT soil moisture products provide a consistent, well-calibrated record [46, 47]. Though other sensors are perhaps better suited to soil moisture monitoring in some areas, the high-resolution ASCAT estimates can be used to form a consistent soil moisture data record over a long period of time [44]. Such a record can be continued far into the future using the next iterations of the ASCAT sensor, launched on the MetOp-B satellite in 2012 and to be launched on the Metop-C satellite in a few years.

4.2 Background

Data collected from both ASCAT and the European Remote-sensing Satellite (ERS) C-band scatterometers have been used to estimate relative soil moisture levels at 12.5×12.5 and 25×25 km/pixel resolution by applying the TU-Wien change detection algorithm to reported σ^0 values [18, 44]. This change detection algorithm exploits the dependence of σ^0 on soil moisture levels: in general, σ^0 increases as the amount of moisture in the soil increases [18]. The relative soil moisture in a particular area can be estimated by first normalizing all σ^0 values to a nominal incidence angle. Then, the maximum and minimum backscatter measurements are found from a long time series of data collected from the area under study. An assumption is made that the highest backscatter value in the time series corresponds to soil which is saturated with water, and the lowest backscatter value corresponds to dry soil. For a given backscatter measurement, a relative soil moisture value (between 0% and 100%) is found by examining where the measurement falls between the measurements corresponding to

dry and water-saturated soil. The volume content of moisture in the soil can also be extracted by multiplying the relative soil moisture value by the porosity of the soil [18]. In this way, a quantitative estimate of soil moisture can be produced using only σ^0 measurements.

The TU-Wien algorithm is briefly summarized here. The relative soil moisture is estimated by first normalizing the σ^0 values to incidence angles which reduce the effect of vegetation growth on the soil moisture estimates. At incidence angles of of 25° (θ_{dry}) for dry soil and 40° (θ_{wet}) for wet soil, the backscatter from an undeveloped vegetation canopy is roughly equivalent to the backscatter from a developed vegetation canopy in a variety of climates [45].

As the relationship between σ^0 and the incidence angle is relatively unaffected by changes in soil moisture [48], the local backscatter values from a wide range of incidence angles are normalized to incidence angles of θ_{dry} and θ_{wet} and used to construct time series of measurements. The backscatter values are normalized as

$$\sigma^0(\theta_n, t) = \sigma^0(\theta, t) - \sigma^{0'}(\theta_n, t)(\theta - \theta_n) - \frac{1}{2}\sigma^{0''}(\theta_n)(\theta - \theta_n)^2, \tag{4.1}$$

where the first and second derivatives of σ^0 with respect to incidence angle are given by $\sigma^{0'}$ and $\sigma^{0''}$, θ is the incidence angle of a particular measurement, and θ_n is either θ_{dry} or θ_{wet} [3].

The relationship between incidence angle and backscatter is roughly linear, and so the second order terms are typically small. The linear relationship is illustrated in Fig. 4.1, where σ^0 measurements are plotted against incidence angle for a small area over 30 days of data. A linear fit appears to represent the data well, especially over the 30 to 60 degree incidence angle range.

The values of $\sigma^{0'}$ and $\sigma^{0''}$ over a given area are calculated using measurements from each ASCAT beam (fore, mid, and aft). Within a short temporal window, the separate beams observe each area within their collective swath at a different incidence angle; hence, an estimate of $\sigma^{0'}$ can be calculated as

$$\sigma^{0'}\left(\frac{\theta_m - \theta_{a/f}}{2}\right) = \frac{\sigma^0_m(\theta_m) - \sigma^0_{a/f}(\theta_{a/f})}{\theta_m - \theta_{a/f}}, \tag{4.2}$$

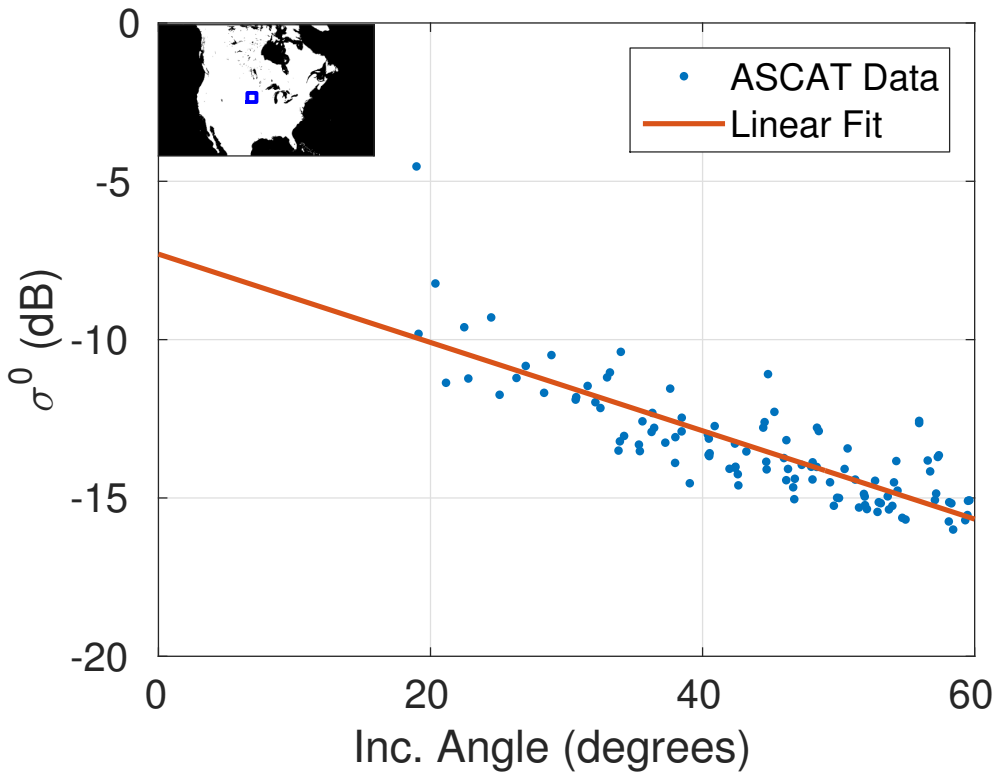

Figure 4.1: A plot of σ^0 versus incidence angle for ASCAT data from the pixel at the center of the square on the map in the upper left of the plot. Data are gathered over 30 days, from day of year 267 to 296 of 2011. The relationship between σ^0 and incidence angle is roughly linear as most data points fall near the regression line.

where the m subscript indicates the midbeam measurement and the a/f subscript indicates either the aft beam or the fore beam measurement. The value of $\sigma^{0''}$ is estimated by calculating the slope of a regression line fit to the estimates of $\sigma^{0'}$ given at a range of incidence angles over some time window.

As described by Naeimi et al. [3], the time series of estimates of $\sigma^{0'}$ and $\sigma^{0''}$ are parameterized as

$$\sigma^{0'}(40,t) = C' + D'\Psi'(t) \tag{4.3}$$

and

$$\sigma^{0''}(40,t) = C'' + D''\Psi''(t). \tag{4.4}$$

Here, C' and D' are parameters describing the minimum value and maximum range of the slope, $\sigma^{0'}$, and C'' and D'' describe the minimum value and maximum range of the curvature,

$\sigma^{0''}$. The seasonal variation of the slope and curvature in a time series are described, based on location and climate, by one of 68 empirically determined trigonometric functions Ψ' and Ψ'' [3].

The backscatter values corresponding to dry soil (σ^0_{dry}) and wet soil (σ^0_{wet}) at 40° incidence angle are found using the following equations.

$$\sigma^0_{dry}(40,t) = C^0_{dry} - D'\Psi'(t)(\theta_{dry} - 40) - \frac{1}{2}D''\Psi''(t)(\theta_{dry} - 40)^2. \tag{4.5}$$

$$\sigma^0_{wet}(40,t) = C^0_{wet} - D'\Psi'(t)(\theta_{wet} - 40) - \frac{1}{2}D''\Psi''(t)(\theta_{wet} - 40)^2. \tag{4.6}$$

Here, C^0_{dry} and C^0_{wet} correspond to the averaged lowest and highest observed values of backscatter in the time series where $\sigma^0(\theta_{inc})$ has been normalized to $\sigma^0(\theta_{dry})$ and $\sigma^0(\theta_{wet})$, respectively [45, 3]. Note that σ^0_{wet} is equal to C^0_{wet} because 40° is chosen for θ_{wet}.

The relative topsoil moisture (m_s) for a given σ^0 measurement can be calculated using σ^0_{wet} and σ^0_{dry} and is given by

$$m_s(t) = \frac{\sigma^0(t) - \sigma^0_{dry}(t)}{\sigma^0_{wet}(t) - \sigma^0_{dry}(t)}. \tag{4.7}$$

The m_s value is an estimate of the water saturation in the top few centimeters of the soil and takes on values between 0% and 100% [45]. Although this conceptually simple model does not perfectly describe the soil moisture, it provides a reasonable approximation.

4.3 High-Resolution Soil Moisture Retrieval

The process for creating high-resolution soil moisture estimates involves first creating high-resolution σ^0 images using the AVE algorithm [19]. Then, an adapted form of the TU-Wien algorithm is applied to extract the soil moisture estimation parameters on the 4.45 × 4.45 km/pixel grid. In the adapted TU-Wien algorithm, a time series of σ^0 measurements for each pixel are normalized to incidence angles of θ_{dry} and θ_{wet} and evaluated to obtain the parameters C^0_{dry} and C^0_{wet}. Following Naeimi, et al. [3], a correction is applied to compensate for an underestimation of C^0_{wet} in arid regions. The σ^0_{dry} and σ^0_{wet} values are calculated using

modified versions of Eqs. 4.5 and 4.6, and the relative topsoil moisture, m_s, is estimated on the 4.45 $\times$ 4.45 km/pixel grid.

The high resolution C-band images of σ^0 are developed separately for the fore, mid, and aft beams of ASCAT using the AVE algorithm on ASCAT data from 2009 to 2014; six years of data is assumed to result in a time series of adequate length to estimate soil moisture. The AVE algorithm is an image reconstruction technique which uses the spatial response function (SRF) of the scatterometer to identify the contribution of each area of the ground footprint of the sensor to a measured σ^0 value [19]. Each pixel in the reconstructed image is formed by taking an average of all σ^0 measurement values, weighted by the SRF value [19, 49].

Due to the fan beam geometry of the ASCAT sensor, σ^0 is measured at a range of incidence angles across the swaths of the fore, mid, and aft beams. The ASCAT swath geometry is shown in Fig. 4.2 [50]. Range-Doppler processing produces 256 measurements along each beam, though only 192 measurements are reported in the publicly available ASCAT data products [50]. Measurement swaths to the right and left side of the sensor ground track are approximately 550 km wide. No measurements are recovered from the nadir gap, or gap in coverage along the ground track of the sensor.

When constructing the ASCAT AVE images for each beam, the effect of the variation in incidence angle is preserved across the measurement swaths. Example images in Fig. 4.3 show the incidence angle variation across measurement swaths for multiple passes over North America. The incidence angles reported from mid-beam measurements differ from those reported by the fore and aft beams, which are somewhat similar. The incidence angles taper off across the swath, affecting the σ^0 measurements, which can be seen for the same passes in Fig. 4.4. As incidence angle decreases, the reported σ^0 measurements increase in value. Where the swaths of the three beams overlap, three observations of σ^0 at different incidence angles are available. Using many measurements of σ^0 at various incidence angles, the first order slope ($\sigma^{0\prime}$) and second order slope ($\sigma^{0\prime\prime}$) of σ^0 versus incidence angle can be calculated.

In order to reduce noise effects while preserving temporal variation, $\sigma^{0\prime}$ values are calculated for each pixel using Eq. 4.2 and a moving window of 30 days of data. To estimate

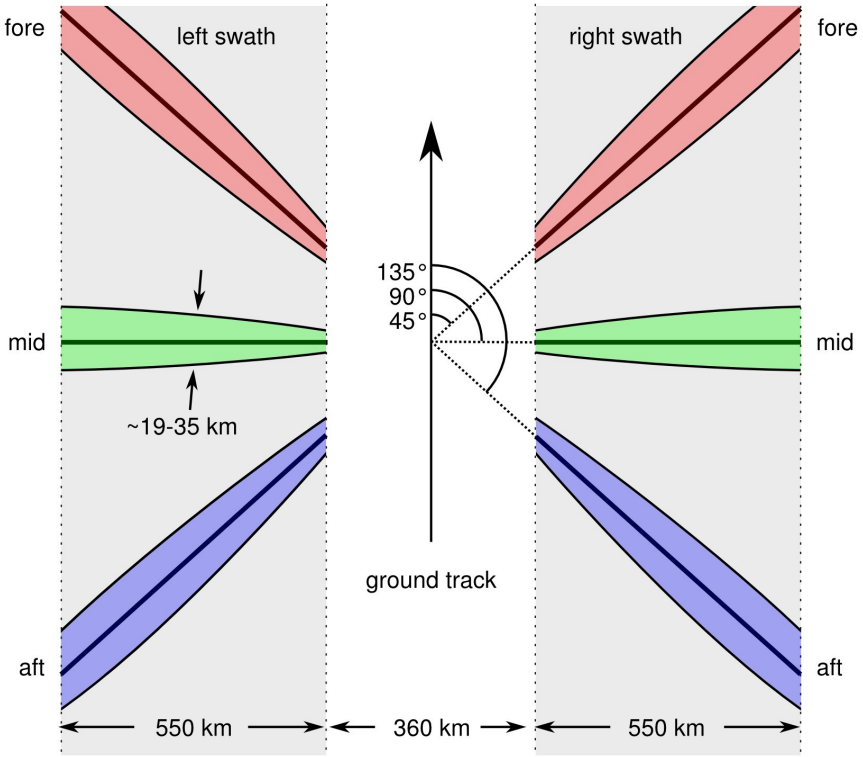

Figure 4.2: The swath geometry of the ASCAT sensor. The azimuth angles of the six beams are shown as well as dimensions of the beam footprints, swaths, and ground track coverage gap. Reproduced from [50].

the value of $\sigma^{0'}$ at 40° incidence angle, estimates of $\sigma^{0'}$ near 40° incidence angle are averaged. The value of $\sigma^{0''}$ is estimated by calculating the slope of a regression line fit to all estimates of $\sigma^{0'}$ from within the 30-day window for each pixel.

Unfortunately, images of $\sigma^{0''}$ contain artifacts where measurements from swath edges of separate orbital passes overlap. To suppress such artifacts, a median filter is applied to the $\sigma^{0''}$ images. Fig. 4.5 demonstrates the effect of the median filter on a sample image of $\sigma^{0''}$ from day 201, 2009. The image artifacts are removed in the median filtered image, and some finer details in the unfiltered image may also be removed.

The AVE σ^0 images are normalized to 25° (θ_{dry}) and 40° (θ_{wet}) incidence angle using Eq. 4.1 with the $\sigma^{0'}$ and median-filtered $\sigma^{0''}$ values. The normalized images from the fore, mid, and aft beams are combined using a weighted average of the pixel values, where the weighting is determined by the number of measurements from the original AVE reconstruction which contributed to each pixel value.

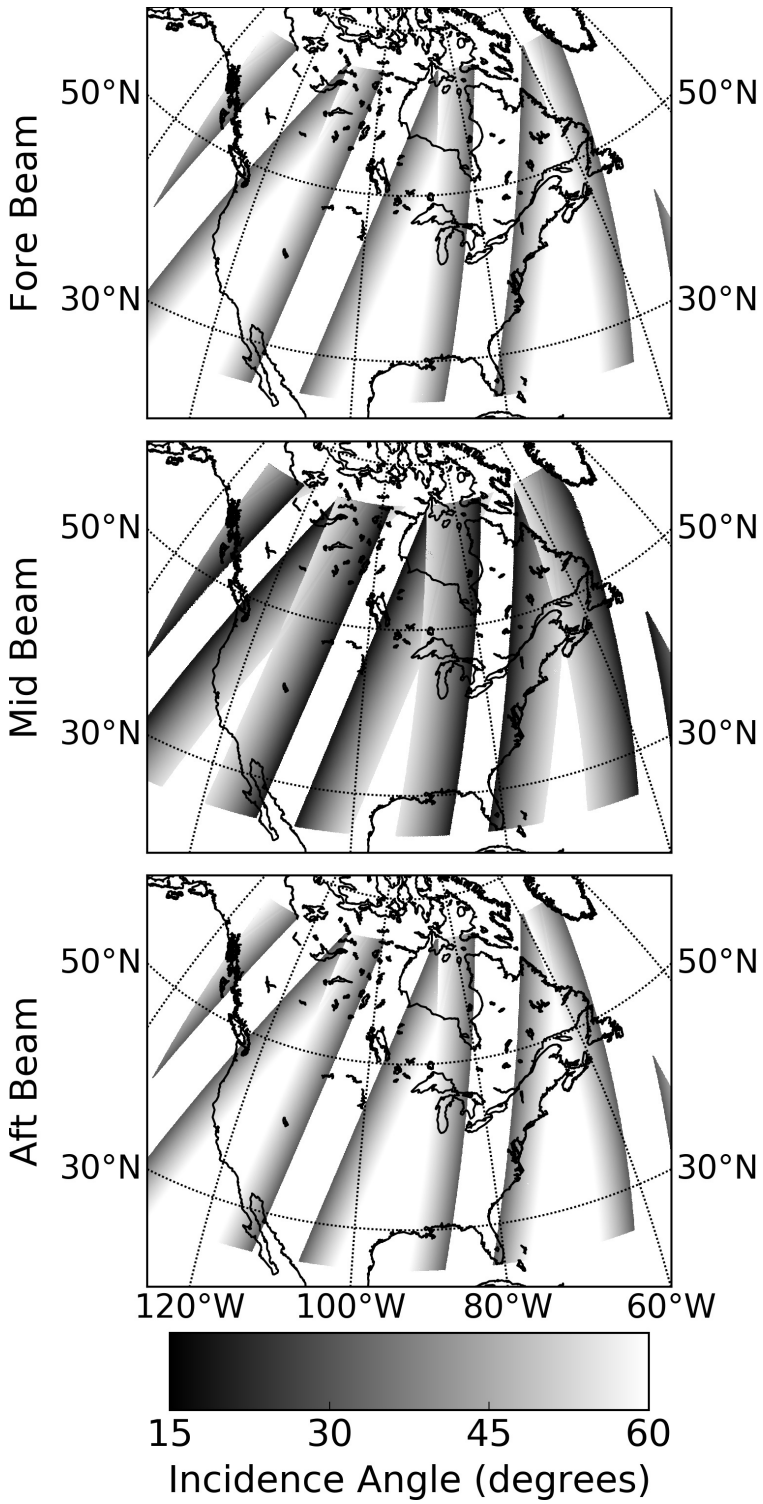

Figure 4.3: Incidence angle measurements from the fore, mid, and aft beams for multiple passes over North America on day of year 201, 2011. Where multiple passes overlap, only data from one pass are shown. The incidence angle values are tapered across the swaths.

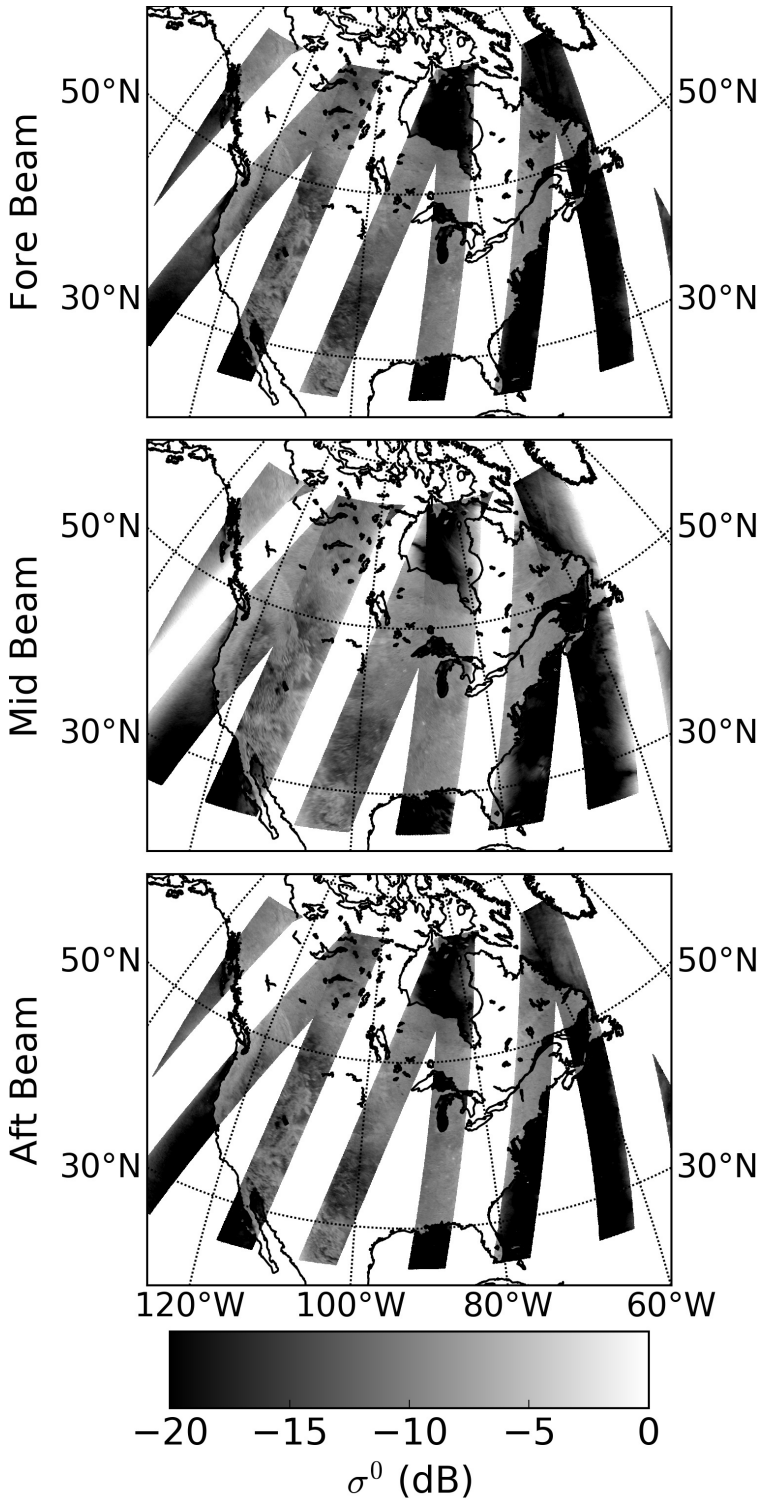

Figure 4.4: Reported σ^0 measurements from the fore, mid, and aft beams for multiple passes over North America on day of year 201, 2011. Where multiple passes overlap, only data from one pass are shown. Values of σ^0 are affected by the change in incidence angle across the swath.

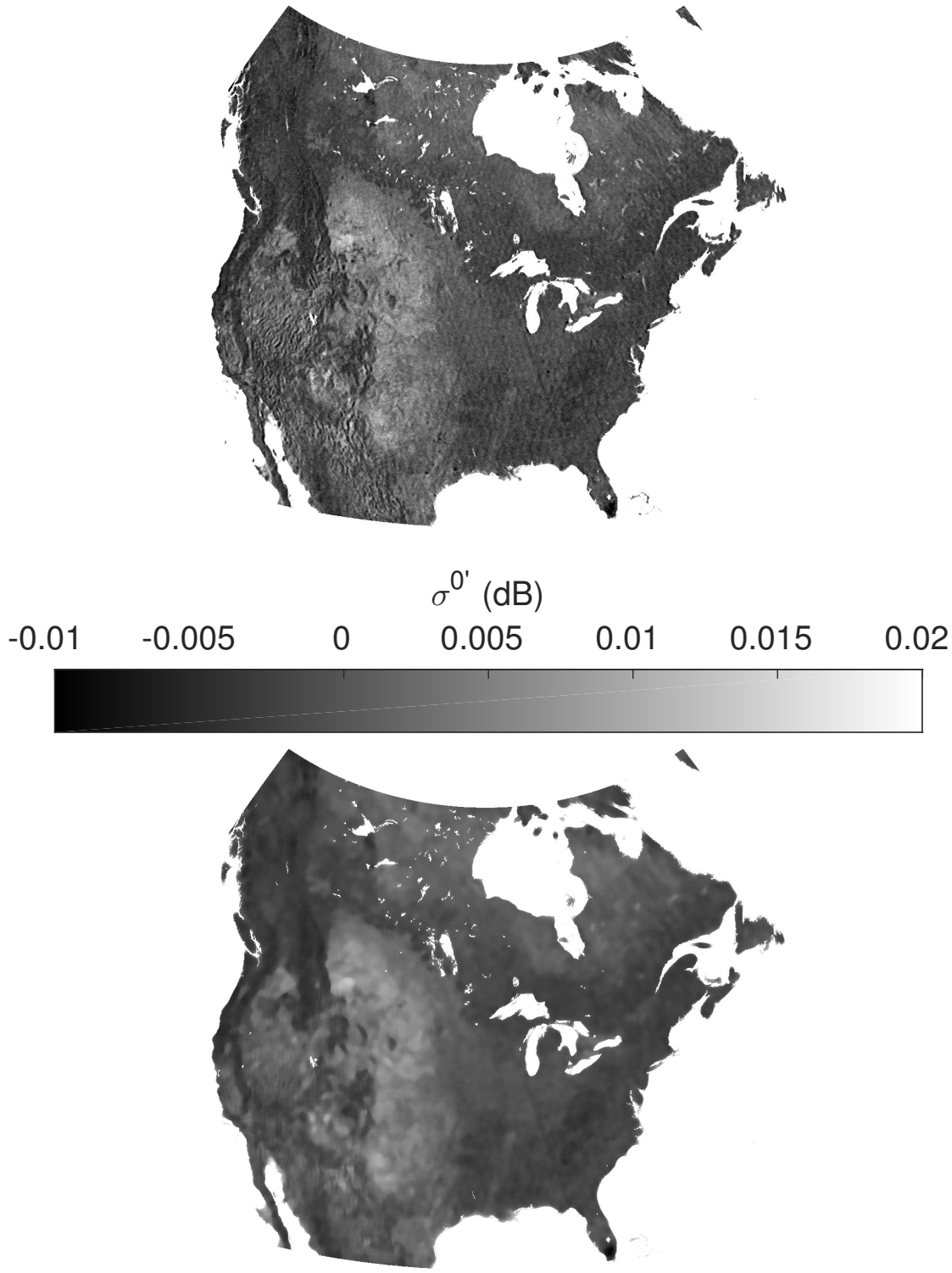

Figure 4.5: Images of $\sigma^{0''}$ over North America for day 201, 2009 prior to median filtering (top) and after median filtering (bottom). Note that the moiré pattern present in the top image is removed by the median filter.

A time series of σ^0 (θ_{dry}) and σ^0 (θ_{wet}) values is constructed for each land pixel of the combined-beam images, and the parameters C^0_{dry} and C^0_{wet} are estimated. Following the WARP version 4 method of ASCAT m_s retrieval [3], $\sigma^0(\theta_{dry})$ and $\sigma^0(\theta_{wet})$ time series outlier values falling beyond three times the interquartile range from the mean are discarded. An average of the remaining σ^0 values is taken and all values falling beyond 1.5 times the interquartile range are discarded. An average of the remaining lowest $\sigma^0(\theta_{dry})$ and highest $\sigma^0(\theta_{wet})$ values is assumed to correspond to dry and water-saturated soil moisture conditions over the land area associated with each pixel. For each pixel, the averaged high and low backscatter values are C^0_{dry} and C^0_{wet}.

The sensitivity of the algorithm to soil moisture changes, C^s, can be observed by normalizing the C^0_{dry} values to a 40° incidence angle (using Eq. 4.1) and taking the difference between C^0_{wet} and $C^0_{dry,40°}$. The soil moisture retrieval algorithm assumes that observations of wet and dry soil are contained within the time series of measurements for each area. In general, C^s decreases as vegetation cover increases and is greatest in areas of thin vegetation or bare soil [45]. In areas of very heavy vegetation, C^0_{dry} increases and C^s decreases, making classification less effective. Despite the lack of vegetation in especially arid or desert areas, values of C^0_{wet} are much lower than in other sparsely vegetated, wetter regimes, contributing to an especially low C^s. The decreased sensitivity in dry regimes likely results from an absence of σ^0 measurements from water-saturated soil across the entire time series of measurements being analyzed. Such low-biased C^0_{wet} values lead to an underestimation of σ^0_{wet}.

Low C^0_{wet} values are identified using a map of climate regimes to isolate areas with an arid climate classification [51]. Following Naeimi et al. [3], a correction is applied in such areas by increasing C^0_{wet} until C^s is at least 5 dB. Differences between initial C^0_{wet} values and the corrected values over North America can be seen in Fig. 4.6. The majority of the corrections correspond to dry, arid regions in the southwestern United States and Mexico.

The values of σ^0_{dry} and σ^0_{wet} are calculated by normalizing C^0_{dry} and C^0_{wet} from incidence angles of θ_{dry} and θ_{wet} to a 40° incidence angle using Eq. 4.1. In this case, θ_{wet} is chosen to be 40° [3], so C^0_{wet} is equivalent to σ^0_{wet} and does not vary temporally. The σ^0_{dry} estimates vary over time and are smoothed to reduce the effects of noise. An example time series of

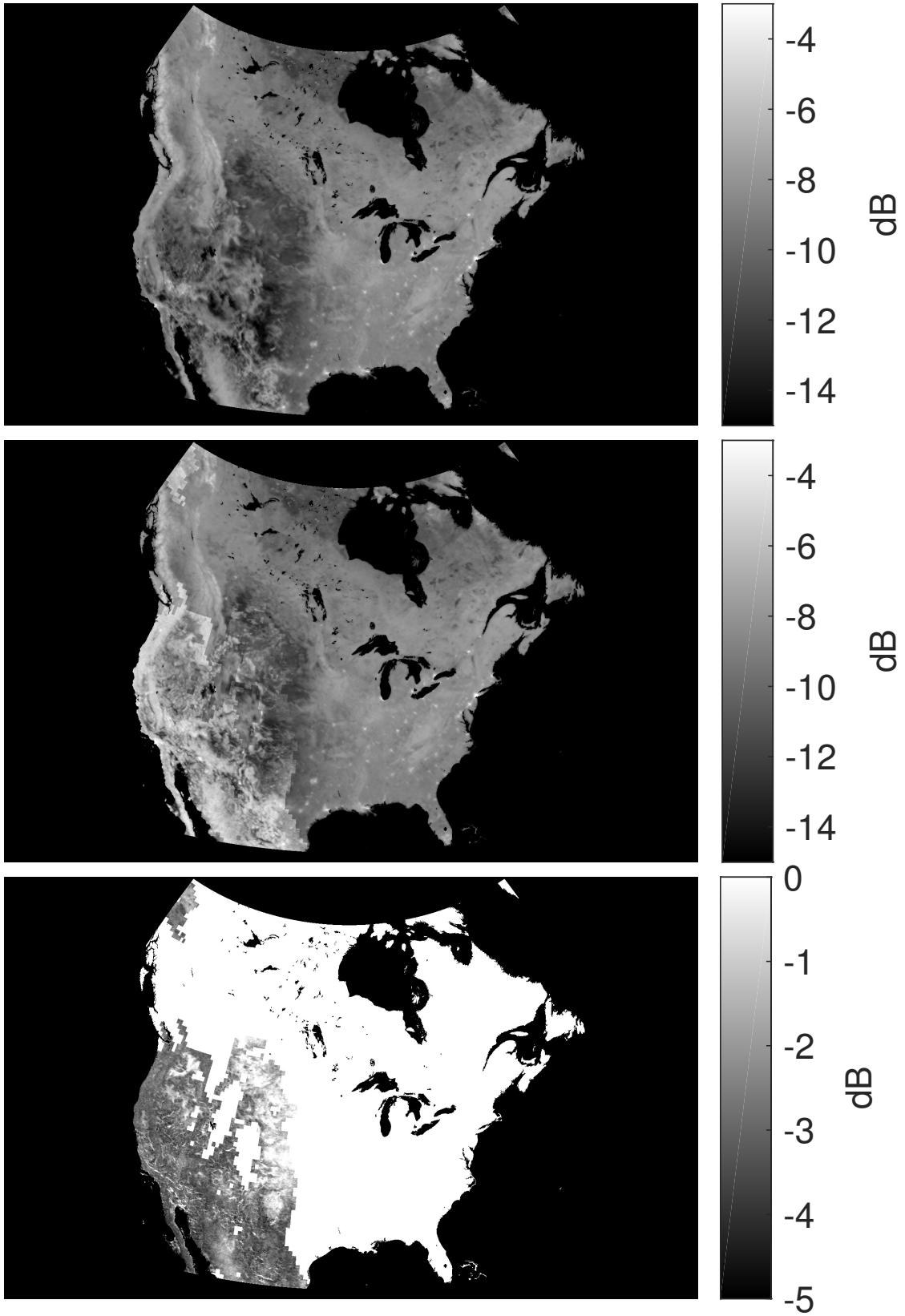

Figure 4.6: Series of images showing initial σ^0_{wet} values (top), the corrected σ^0_{wet} values (middle) and the difference (bottom).

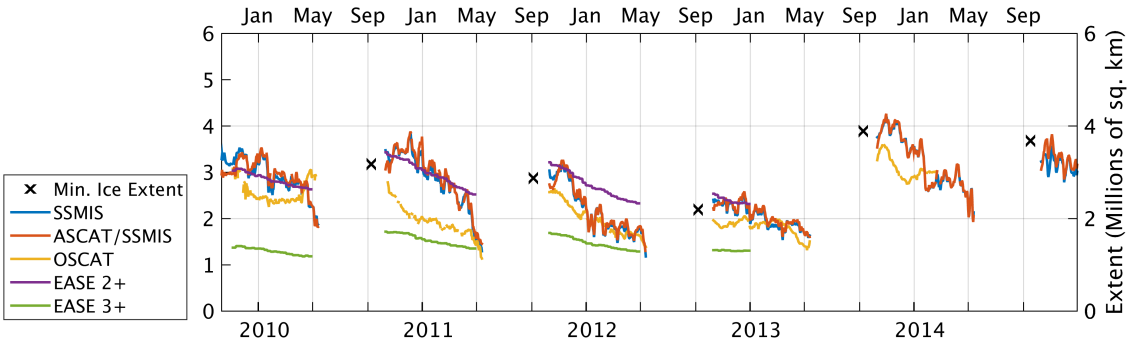

Figure 4.7: Time series of σ^0_{wet}, σ^0_{dry}, and σ^0 . for the pixel indicated in the map of North America in the upper right. Measurements of σ^0 approaching σ^0_{dry} (bottom line) are assumed to correspond to dry soil, whereas measurements approaching σ^0_{wet} (top line) are assumed to correspond to wet soil.

σ^0_{wet}, σ^0_{dry}, and σ^0 for a single pixel is shown in Fig. 4.7. The figure shows the seasonal variation of σ^0 as well as where σ^0_{wet} and σ^0_{dry} are located with respect to the highest and lowest observed values of σ^0 . Using the values calculated for σ^0_{dry} and σ^0_{wet}, m_s is found using Eq. 4.7.

4.4 Results

The high-resolution m_s estimates are compared to the lower-resolution WARP 5.5 soil moisture product for validation. Data from the WARP soil moisture product are obtained from the EUMETSAT Satellite Application Facility on Support to Operational Hydrology and Water Management (H-SAF) data center and placed on a 12.5 km grid using a drop-in-the-bucket approach.

Images comparing the high-resolution and low-resolution WARP retrieved soil moisture parameters over North America, along with a zoom-in comparison near Lake Superior are shown in Fig. 4.8. Some differences are apparent between retrieved values of m_s, with the high-resolution product exhibiting somewhat greater values than the WARP product throughout the southeast and southwest United States. In the zoom-in comparison, the higher resolution image more clearly resolves the extent of wet areas on the coast of Lake Superior and reveals more of the variation within drier areas.

Differences between the high-resolution and WARP products over North America are further characterized by examining data from the year 2009. Images of m_s at high-

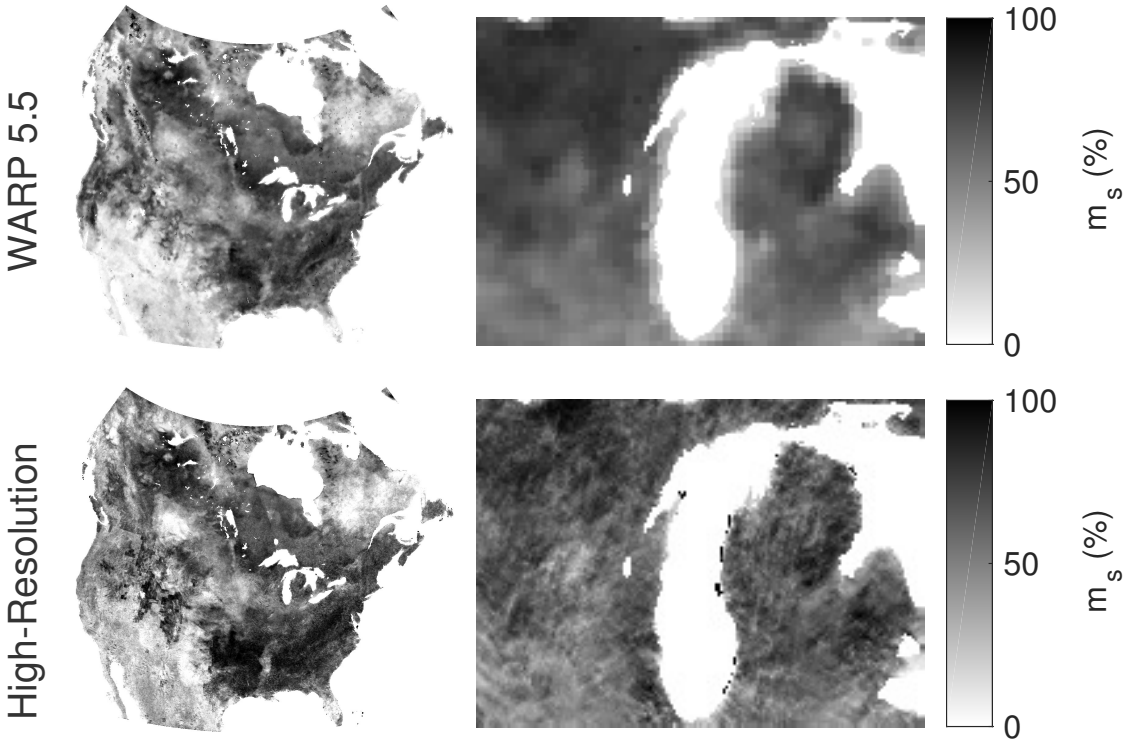

Figure 4.8: Series of images comparing the high-resolution and WARP low-resolution m_s values using data from DOY 121-125, 2009. The high resolution image reveals finer features than the WARP image, but reports greater soil moisture values than WARP in the southern United States.

resolution and from the WARP product are processed for every two days using five days of data to reduce coverage gaps. For each pair of high- and low-resolution images, the difference between pixel m_s values is calculated. The mean and standard deviation of the pixel value differences for this period are shown in Fig. 4.9. The RMS mean pixel difference is 10.82 percent, and the RMS standard deviation is 10.51 percent. The figure demonstrates that the high-resolution m_s estimates exceed those reported by the low-resolution product in some areas throughout North America. Overall, the high-resolution product appears to be slightly biased towards greater values of m_s compared to the low-resolution product.

Estimates of m_s are also produced on a 12.5 $\times$ 12.5 km/pixel grid using the same method as the high resolution m_s estimates, except without resolution enhancement. The σ^0 data are placed on the 12.5 $\times$ 12.5 km/pixel grid by binning and averaging all measurements whose centers fall within each pixel for each pass. The m_s estimates produced with this method are also compared to the WARP product over North America using the 2009 data.

The resulting mean difference and standard deviation values are comparable to those shown in Fig. 4.9; the RMS mean pixel difference is 10.96 percent, and the RMS standard deviation is 10.97 percent.

The bias in the high and low-resolution soil moisture estimates compared to the WARP soil moisture estimates is likely a result of differences in processing techniques. The WARP product may incorporate more extensive empirical corrections to σ^0_{wet} that are not replicated here. Additionally, while a moving average is here used to smooth noisy estimates of the $\sigma^{0\prime}$ and $\sigma^{0\prime\prime}$ parameters over the time series, the WARP product uses empirically derived trigonometric functions to interpolate the parameters over time [3]. Though we attempt to replicate the WARP algorithm based on the documentation in the literature, other implementation differences are possible. The performance of the WARP algorithm has been evaluated using soil moisture data from other satellite sensors and *in situ* data from soil moisture monitoring stations [52, 47, 53, 54].

To improve the m_s estimates, measurements from the ASCAT-B sensor aboard the MetOp-B satellite could also be incorporated into the algorithm. As the ASCAT-B sensor is well-calibrated to ASCAT-A and operates at the same frequency, tandem processing of the data is reasonable. Incorporating ASCAT-B measurements would increase the number of measurements available, leading to reduced noise in estimates of the soil moisture parameters. Additional measurements might also enable m_s images at finer temporal resolution. Differences between ASCAT-A and ASCAT-B, as well as high-resolution processing of tandem data are discussed in greater detail in Appendix A.

4.5 Conclusion

Using high-resolution estimates of σ^0 produced with ASCAT and the AVE algorithm, high-resolution soil moisture estimates can successfully be retrieved. Estimates of m_s are produced for North America using a modified version of the TU-Wien algorithm. High-resolution values of m_s show a bias towards greater soil moisture values when compared with the lower-resolution WARP soil-moisture product. Overall trends in the high-resolution estimates show general agreement with the lower-resolution WARP product, with an RMS mean difference in 2009 of 10.82 percent. In the high-resolution images, it is possible to

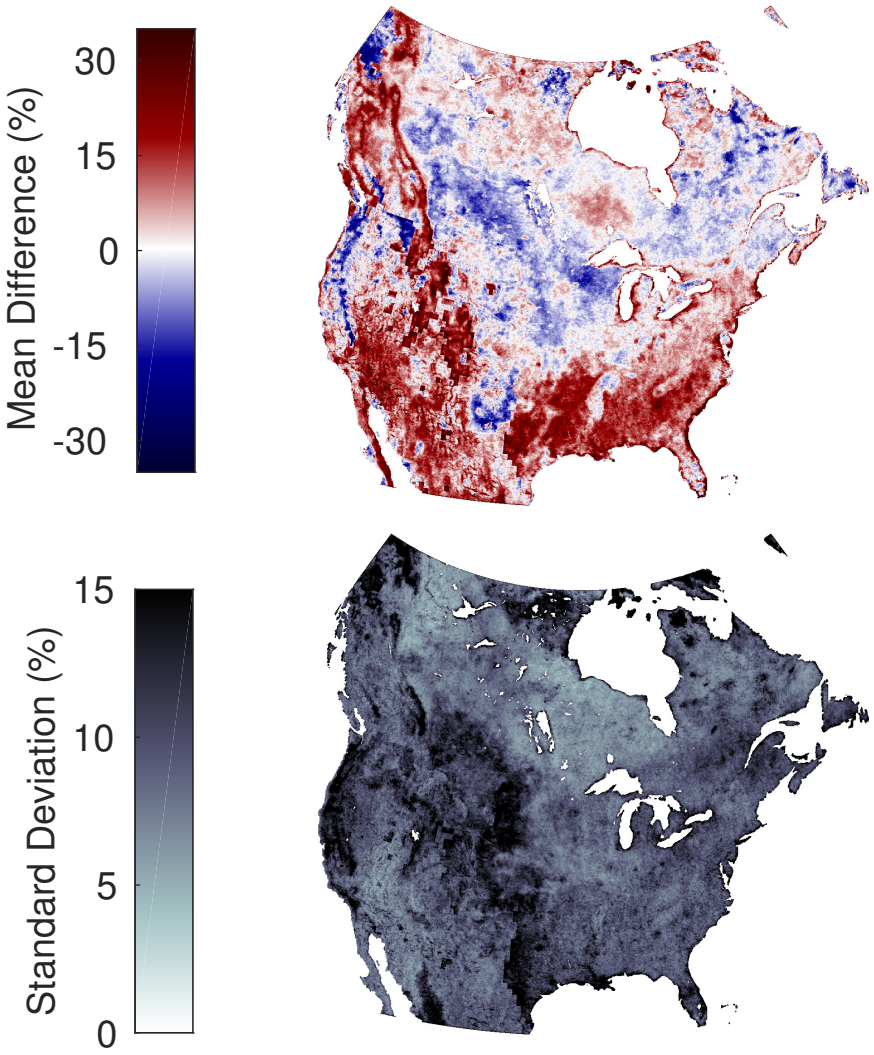

Figure 4.9: Mean (left) and standard deviation (right) of the pixel value differences between the high-resolution and WARP low-resolution m_s estimates over a time series of images for 2009 for North America.

observe soil moisture features at a finer scale. Although soil moisture retrieval in this chapter is limited to North America, retrieval over other regions is possible.

Chapter 5

Conclusion

Satellite microwave sensors provide information which can help improve understanding of the earth's dynamic and complex physical systems. This thesis demonstrates that data from the QuikSCAT, OSCAT, ASCAT, and SSMIS sensors enable classification of the type and extent of Arctic ice and high-resolution estimation of moisture content in the soil. In order to estimate such physical properties, data processing algorithms are developed which can extract physical information from microwave scattering and passive emissivity measurements.

By employing a simple thresholding scheme on backscatter values from QuikSCAT and OSCAT, Arctic ice can be classified as FY or MY within the area of the ice extent. Ice classifications are completed with QuikSCAT from 1999 to 2009 and then extended using data from the OSCAT sensor for the years 2009 to 2014. Corrections are applied to account for anomalies in the OSCAT dataset, and a correction algorithm is applied to the entire ice classification record to reduce spurious classifications of MY ice near the sea ice edge. Using QuikSCAT and OSCAT, a 15-year record of near-contiguous daily Arctic ice classification images is produced.

The OSCAT ice classification record ends with the failure of the OSCAT sensor in 2014. To provide ice classifications for the years after, ASCAT is employed with passive microwave brightness temperature data from SSMIS to synergistically classify ice age in the Arctic. A Bayesian estimator is employed to classify the ice, and the resulting classifications are compared with the OSCAT ice classifications and classifications from the EASE-Grid Sea Ice Age data set and the Canadian Ice Service ice charts. The comparison shows that the extent of MY ice classified using ASCAT/SSMIS typically exceeds the extent classified using OSCAT, but shows better agreement with the extent of ice classified as 2 years or older in the EASE-Grid Sea Ice Age dataset. Ice classifications using ASCAT and SSMIS

can be continued into the future as the current sensors continue to operate and as the next iterations of ASCAT and SSMIS are introduced.

Enhanced resolution processing techniques can also be applied to data from the ASCAT sensor to improve the resolution of soil-moisture estimates. While ASCAT soil moisture estimates presently produced using the WAter Retrieval Package (WARP) are available on a 12.5×12.5 or 25×25 km/pixel grid, using the ASCAT spatial response function and a modified version of the WARP algorithm produces estimates at 4.45×4.45 km/pixel resolution. The high-resolution estimates are compared with the lower resolution WARP estimates over North America and found to be slightly biased towards higher values, especially in the southern United States, where the enhanced-resolution soil moisture values are approximately 20 to 30 percent greater than the low-resolution estimates. The overall RMS mean difference of data analyzed for 2009 was 10.82 percent. The differences may be a result of empirical climate corrections in the WARP product that are not reproduced in the high-resolution product. Greater noise levels in the high-resolution product or other differences between the retrieval algorithms may also contribute to differences. The high-resolution product reveals finer soil moisture details than are visible in the WARP products.

5.1 Contributions

The results of this thesis contribute to the body of published work in the areas of remote sensing of sea ice and soil moisture. The details of ice classification using QuikSCAT and OSCAT, described in Chapter 2, have been published in [13]. Key results from Arctic ice classification using ASCAT/SSMIS and soil moisture estimation using ASCAT, described in Chapters 3 and 4, have been submitted for publication [55, 56]. The primary contributions can be summarized as follows.

1. An ice classification algorithm for QuikSCAT and OSCAT that is used to produce a 15-year record of FY and MY ice classifications in the Arctic.

2. A new algorithm for ice classification using a fusion of ASCAT and SSMIS data that can be used to classify Arctic sea ice for years after the failure of the OSCAT sensor.

3. An algorithm for high-resolution soil moisture retrieval which exploits ASCAT's high-resolution image capability using a modified version of the WARP algorithm.

5.2 Future Work

Areas of future research relating to the improvement or continuation of ice classification and soil moisture studies are described in the following sections.

5.3 Reprocessing of OSCAT Classifications

Currently available OSCAT σ^0 measurements are poorly calibrated from year to year and contain jumps and shifts which appear to be caused by power anomalies onboard the sensor [28]. Additionally, many days of data are missing from the OSCAT dataset. If the Indian Space Research Organization releases an improved dataset, the OSCAT ice classifications can be improved by reprocessing with the corrected data.

5.4 Analysis of MIZ Correction Algorithm

The MIZ correction algorithm could be analyzed to determine how each implementation step impacts the performance. One area of interest is the effect of the lag time on performance. The lag time describes the time delay between data used to create the MY ice mask and the day of ice classifications to which the mask is applied. The methods used to produce the MY ice mask could also be altered to use averaging or multiple days of data to possibly improve performance.

5.5 Improvement of ASCAT/SSMIS Ice Classifications

Data from additional sensors could be incorporated into the ASCAT/SSMIS classification methodology to improve the ice classifications. Increasing the amount of data could reduce artifacts caused by sudden increases in total ice extent or reduce the effects of noise on the classification results. Instead of using a Gaussian model, estimates of the actual probability distributions of FY and MY ice could also be used to improve the classifications.

5.6 Extension of ASCAT/SSMIS Ice Classifications

As the current ASCAT and SSMIS sensors continue to produce data and future iterations of these sensors come online, ice classifications can continue to be processed. An analysis of the resulting long time series of ice classifications could be helpful in revealing trends in the growth or retreat of MY ice in the Arctic.

5.7 Tandem Processing for Soil Moisture Estimates

Data from both currently operational ASCAT sensors (ASCAT-A and ASCAT-B) can be used to increase the number of measurements for soil moisture estimation. An increase in the number of measurements could result in reduced noise and improved spatial coverage of the relative soil moisture estimates. More measurements could also improve estimates of parameters used in the soil moisture retrieval algorithm.

5.8 Global Soil Moisture Retrieval

In this thesis, high-resolution soil moisture estimates are only analyzed for North America. The estimates can also be processed for other areas. Although empirical corrections are employed to improve soil moisture retrieval in dry climate regimes, a superior data-based correction could also be developed which would simplify and perhaps improve performance of the retrieval algorithm globally.

Bibliography

[1] D. Cavalieri, C. Parkinson, P. Gloersen, and H. Zwally. (1996, updated yearly) Sea ice concentrations from Nimbus-7 SMMR and DMSP SSM/I-SSMIS passive microwave data. [Subset 1999-2014]. Boulder, Colorado USA: NASA National Snow and Ice Data Center Distributed Active Archive Center. [Online]. Available: http://dx.doi.org/10.5067/8GQ8LZQVL0VL xi, 1, 9, 10, 29, 33, 44

[2] A. Swan and D. Long, "Multi-year Arctic sea ice classification using QuikSCAT," *IEEE Trans. Geosci. Remote Sens.*, vol. 50, no. 3, pp. 3317–3326, 2012. 1, 2, 4, 8, 9, 11, 28, 29, 34

[3] V. Naeimi, K. Scipal, Z. Bartalis, S. Hasenauer, and W. Wagner, "An improved soil moisture retrieval algorithm for ERS and METOP scatterometer observations," *IEEE Trans. Geosci. Remote Sens.*, vol. 47, no. 7, pp. 1999–2013, July 2009. 1, 2, 4, 48, 50, 51, 52, 58, 62

[4] F. D. Carsey, R. G. Barry, and W. F. Weeks, *Introduction.* American Geophysical Union, 1992, pp. 1–7. [Online]. Available: http://dx.doi.org/10.1029/GM068p0001 1

[5] *Earth Science and Applications from Space: National Imperatives for the Next Decade and Beyond.* Washington, DC: The National Academies Press, 2007. 1, 2, 5, 49

[6] W. Crow, G. Huffman, R. Bindlish, and T. Jackson, "Improving satellite-based rainfall accumulation estimates using spaceborne surface soil moisture retrievals," *"J. Hydrometeorol."*, vol. 10, pp. 199–212, February 2009. 1

[7] C. Hauck, C. Barthlott, L. Krauss, and N. Kalthoff, "Soil moisture variability and its influence on convective precipitation over complex terrain," *Quarterly Journal of the Royal Meteorological Society*, vol. 137, no. S1, pp. 42–56, 2011. 1

[8] A. L. Barbu, J. Calvet, J. Mahfouf, and S. Lafont, "Integrating ASCAT surface soil moisture and GEOV1 leaf area index into the SURFEX modelling platform: a land data assimilation application over France," *Hydrology and Earth System Sciences*, vol. 18, no. 1, pp. 173–192, 2014. 1

[9] A. K. Prasad, L. Chai, R. P. Singh, and M. Kafatos, "Crop yield estimation model for Iowa using remote sensing and surface parameters," *International Journal of Applied Earth Observation and Geoinformation*, vol. 8, no. 1, pp. 26 – 33, 2006. 1

[10] J. Comiso, "Characteristics of Arctic winter sea ice from satellite multispectral microwave observations," *Journal of Geophysical Research*, vol. 91, no. C1, pp. 975–994, 1986. 2

[11] F. Carsey, "Arctic sea ice distribution at end of summer 1973–1976 from satellite microwave data," *Journal of Geophysical Research*, vol. 87, no. C8, pp. 5809–5835, 1982. 2

[12] D. Thomas and D. Rothrock, "The Arctic Ocean ice balance: A Kalman smoother estimate," *Journal of geophysical research*, vol. 98, no. C6, pp. 10 053–10, 1993. 2

[13] D. Lindell and D. Long, "Multiyear Arctic sea ice classification using OSCAT and QuikSCAT," *IEEE Trans. Geosci. Remote Sens.*, vol. 54, no. 1, pp. 167–175, Jan 2016. x, 2, 5, 29, 30, 33, 36, 37, 39, 40, 42, 45, 65

[14] S. Paloscia, G. Macelloni, E. Santi, and T. Koike, "A multifrequency algorithm for the retrieval of soil moisture on a large scale using microwave data from SMMR and SSM/I satellites," *IEEE Trans. Geosci. Remote Sens.*, vol. 39, no. 8, pp. 1655–1661, Aug 2001. 2, 48

[15] T. Jackson, M. Cosh, R. Bindlish, and J. Du, "Validation of AMSR-E soil moisture algorithms with ground based networks," in *Geoscience and Remote Sensing Symposium, 2007. IGARSS 2007. IEEE International*, July 2007, pp. 1181–1184. 2, 48

[16] D. Entekhabi, E. Njoku, P. O'Neill, K. Kellogg, W. Crow, W. Edelstein, J. Entin, S. Goodman, T. Jackson, J. Johnson, J. Kimball, J. Piepmeier, R. Koster, N. Martin, K. McDonald, M. Moghaddam, S. Moran, R. Reichle, J. Shi, M. Spencer, S. Thurman, L. Tsang, and J. Van Zyl, "The Soil Moisture Active Passive (SMAP) mission," *Proceedings of the IEEE*, vol. 98, no. 5, pp. 704–716, May 2010. 2, 49

[17] Y. Kerr, P. Waldteufel, J. Wigneron, J. Martinuzzi, J. Font, and M. Berger, "Soil moisture retrieval from space: the Soil Moisture and Ocean Salinity (SMOS) mission," *IEEE Trans. Geosci. Remote Sens.*, vol. 39, no. 8, pp. 1729–1735, Aug 2001. 2, 49

[18] W. Wagner, G. Lemoine, and H. Rott, "A method for estimating soil moisture from ERS scatterometer and soil data," *Remote Sensing of Environment*, vol. 70, no. 2, pp. 191–207, 1999. 4, 48, 49, 50

[19] R. Lindsley and D. Long, "Enhanced-resolution reconstruction of ASCAT backscatter measurements," *IEEE Trans. Geosci. Remote Sens.*, vol. PP, no. 99, pp. 1–13, 2015. 4, 32, 48, 52, 53, 84, 89

[20] W. Tucker, D. Perovich, A. Gow, W. Weeks, and M. Drinkwater, *Microwave remote sensing of sea ice*. American Geophysical Union, 1992, ch. Physical Properties of Sea Ice Relevant to Remote Sensing. 7

[21] D. T. Eppler, L. D. Farmer, A. W. Lohanick, M. R. Anderson, D. J. Cavalieri, J. Comiso, P. Gloersen, C. Garrity, T. C. Grenfell, M. Hallikainen, J. A. Maslanik, C. Mätzler, R. A. Melloh, I. Rubinstein, and C. T. Swift, *Passive Microwave Signatures of Sea Ice*. American Geophysical Union, 2013, pp. 47–71. [Online]. Available: http://dx.doi.org/10.1029/GM068p0047 8, 44

[22] J. Haarpaintner, R. Tonboe, D. Long, and M. Van Woert, "Automatic detection and validity of the sea-ice edge: an application of enhanced-resolution QuikScat/SeaWinds data," *IEEE Trans. Geosci. Remote Sens.*, vol. 42, no. 7, pp. 1433–1443, 2004. 8

[23] D. Early and D. Long, "Image reconstruction and enhanced resolution imaging from irregular samples," *IEEE Trans. Geosci. Remote Sens.*, vol. 39, no. 2, pp. 291–302, Feb 2001. 8

[24] M. Spencer, C. Wu, and D. Long, "Improved resolution backscatter measurements with the SeaWinds pencil-beam scatterometer," *IEEE Trans. Geosci. Remote Sens.*, vol. 38, no. 1, pp. 89–104, 2000. 8

[25] J. Bradley and D. Long, "Estimation of the OSCAT spatial response function using island targets," *IEEE Trans. Geosci. Remote Sens.*, vol. 52, no. 4, pp. 1924–1934, April 2014. 11

[26] D. Cavalieri. (2003, May) NASA team sea ice algorithm. [Online]. Available: http://nsidc.org/data/docs/daac/nasateam/ 10

[27] W. Meier and J. Stroeve, "Comparison of sea-ice extent and ice-edge location estimates from passive microwave and enhanced-resolution scatterometer data," *Annals of Glaciology*, vol. 48, pp. 65–70, 2008. 11

[28] S. Bhowmick, R. Kumar, and A. Kumar, "Cross calibration of the OceanSAT-2 scatterometer with QuikSCAT scatterometer using natural terrestrial targets," *IEEE Trans. Geosci. Remote Sens.*, vol. 52, no. 6, pp. 3393–3398, June 2014. 13, 66

[29] M. Rivas, J. Verspeek, A. Verhoef, and A. Stoffelen, "Bayesian sea ice detection with the Advanced Scatterometer ASCAT," *IEEE Trans. Geosci. Remote Sens.*, vol. 50, no. 7, pp. 2649–2657, July 2012. 24

[30] Scatterometer climate record pathfinder. [Online]. Available: http://www.scp.byu.edu/ 28, 31, 32, 42, 89, 91

[31] D. Cavalieri. (1992, May) NASA team sea ice algorithm. [Online]. Available: http://nsidc.org/data/docs/daac/nasateam/ 31

[32] J. Maslanik and J. Stroeve. (2015) DMSP SSM/I-SSMIS daily polar gridded brightness temperatures. National Snow and Ice Data Center, Boulder, CO. [Online]. Available: http://nsidc.org/data/nsidc-0001/ 31

[33] S. Beaven, S. Gogineni, and F. Carsey, "Fusion of satellite active and passive microwave data for sea ice type concentration estimates," *IEEE Trans. Geosci. Remote Sens.*, vol. 34, no. 5, pp. 1172–1183, Sep 1996. 32

[34] Q. Remund, D. Long, and M. Drinkwater, "An iterative approach to multisensor sea ice classification," *IEEE Trans. Geosci. Remote Sens.*, vol. 38, no. 4, pp. 1843–1856, Jul 2000. 32

[35] M. Shokr and T. Agnew, "Validation and potential applications of Environment Canada Ice Concentration Extractor (ECICE) algorithm to Arctic ice by combining AMSR-E and QuikSCAT observations," *Remote Sensing of Environment*, vol. 128, pp. 315 – 332, 2013. [Online]. Available: http://www.sciencedirect.com/science/article/pii/S003442571200404X 32

[36] D. Long, P. Hardin, and P. Whiting, "Resolution enhancement of spaceborne scatterometer data," *IEEE Trans. Geosci. Remote Sens.*, vol. 31, no. 3, pp. 700–715, 1993. 32

[37] D. Cavalieri, C. Parkinson, N. DiGirolamo, and A. Ivanoff, "Intersensor calibration between F13 SSMI and F17 SSMIS for global sea ice data records," *Geoscience and Remote Sensing Letters, IEEE*, vol. 9, no. 2, pp. 233–236, March 2012. 33

[38] M. Tschudi, C. Fowler, and J. Maslanik. (2014) EASE-grid sea ice age [2009-2012]. Boulder, Colorado USA: NASA National Snow and Ice Data Center Distributed Active Archive Center. [Online]. Available: http://dx.doi.org/10.5067/1UQJWCYPVX61 33, 39

[39] (2014) Canadian ice service Arctic regional sea ice charts in SIGRID-3 format, version 1. [2010-2012]. Boulder, Colorado USA: NASA National Snow and Ice Data Center Distributed Active Archive Center. [Online]. Available: http://dx.doi.org/10.7265/N51V5BW9 33, 39

[40] M. Tschudi, C. Fowler, J. Maslanik, and J. Stroeve, "Tracking the movement and changing surface characteristics of Arctic sea ice," *IEEE J. Sel. Topics Appl. Earth Observations Remote Sens.*, vol. 3, no. 4, pp. 536–540, Dec 2010. 33

[41] R. Kwok, A. Schweiger, D. A. Rothrock, S. Pang, and C. Kottmeier, "Sea ice motion from satellite passive microwave imagery assessed with ERS SAR and buoy motions," *Journal of Geophysical Research: Oceans*, vol. 103, no. C4, pp. 8191–8214, 1998. [Online]. Available: http://dx.doi.org/10.1029/97JC03334 33

[42] J. Comiso, "Large decadal decline of the Arctic multiyear ice cover," *Journal of Climate*, vol. 25, no. 4, pp. 1176–1193, 2012. 45

[43] R. Tilling, A. Ridout, A. Shepherd, and D. Wingham, "Increased Arctic sea ice volume after anomalously low melting in 2013," *Nature Geoscience*, vol. 8, no. 8, pp. 643–646, 2015. 45

[44] S. Hahn, T. Melzer, and W. Wagner, "Error assessment of the initial near real-time METOP ASCAT surface soil moisture product," *IEEE Trans. Geosci. Remote Sens.*, vol. 50, no. 7, pp. 2556–2565, July 2012. 48, 49, 74

[45] K. Scipal, "Global soil moisture retrieval from ERS scatterometer data," PhD dissertation, Institute of Photogrammetry and Remote Sensing of Vienna University of Technology, 2002. 48, 50, 52, 58

[46] W. Wagner, S. Hahn, A. Gruber, and W. Dorigo, "Identification of soil moisture retrieval errors: Learning from the comparison of SMOS and ASCAT," in *Geoscience and Remote Sensing Symposium (IGARSS), 2012 IEEE International*, July 2012, pp. 3795–3798. 49

[47] W. Wagner, L. Brocca, V. Naeimi, R. Reichle, C. Draper, R. de Jeu, D. Ryu, C. Su, A. Western, J. Calvet, Y. Kerr, D. Leroux, M. Drusch, T. Jackson, S. Hahn, W. Dorigo, and C. Paulik, "Clarifications on the comparison between SMOS, VUA, ASCAT, and ECMWF soil moisture products over four watersheds in U.S." *IEEE Trans. Geosci. Remote Sens.*, vol. 52, no. 3, pp. 1901–1906, March 2014. 49, 62

[48] W. Wagner and G. Lemoine, "Land cover effects on ERS scatterometer data," in *Geoscience and Remote Sensing Symposium Proceedings, 1998. IGARSS '98. 1998 IEEE International*, vol. 3, Jul 1998, pp. 1574–1576 vol.3. 50

[49] R. Lindsley and D. Long, "A parameterized ASCAT measurement spatial response function," *IEEE Trans. Geosci. Remote Sens.*, in review. 53

[50] R. Lindsley, "Enhanced resolution processing and applications of the ASCAT scatterometer," PhD dissertation, Brigham Young University, 2015. xi, xiii, xiv, 53, 54, 74, 75, 82, 84, 85, 87

[51] M. Kottek, J. Grieser, C. Beck, Z. Rudolf, and F. Rubel, "World map of the Koppen-Geiger climate classification updated," *Meteorologische Zeitschrift*, vol. 15, no. 3, pp. 259–263, Jun 2006. 58

[52] R. Amri, M. Zribi, Z. Lili-Chabaane, W. Wagner, and S. Hasenauer, "Analysis of C-Band scatterometer moisture estimations derived over a semiarid region," *IEEE Transactions on Geoscience and Remote Sensing*, vol. 50, no. 7, pp. 2630–2638, July 2012. 62

[53] K. R. Bhimala and P. Goswami, "A comparison of ASCAT soil moisture data with in situ observations over the Indian region: A multiscale analysis," *IEEE Transactions on Geoscience and Remote Sensing*, vol. 53, no. 10, pp. 5425–5434, Oct 2015. 62

[54] L. Brocca, F. Melone, T. Moramarco, W. Wagner, and S. Hasenauer, "ASCAT soil wetness index validation through in situ and modeled soil moisture data in central Italy," *Remote Sensing of Environment*, vol. 114, no. 11, pp. 2745 – 2755, 2010. [Online]. Available: http://www.sciencedirect.com/science/article/pii/S0034425710001999 62

[55] D. Lindell and D. Long, "Multiyear Arctic ice classification using ASCAT and SSMIS," *Remote Sensing*, "in review". 65

[56] ——, "High-resolution soil moisture retrieval with ASCAT," *IEEE Geosci. Remote Sens. Lett.*, "in review". 65

[57] X. Yang, X. Li, W. Pichel, and Z. Li, "Comparison of ocean surface winds from ENVISAT ASAR, MetOp ASCAT scatterometer, bouy measurements, and NOGAPS model," *IEEE Trans. Geosci. Remote Sens.*, vol. 49, no. 12, pp. 4743–4750, 2011. 74

[58] A. Verhoef, M. Portabella, and A. Stoffelen, "High-resolution ASCAT scatterometer winds near the coast," *IEEE Trans. Geosci. Remote Sens.*, vol. 50, no. 7, pp. 2481–2487, 2012. 74

[59] V. Naeimi, C. Paulik, A. Bartsch, W. Wagner, R. Kidd, S. Park, K. Elger, and J. Boike, "ASCAT surface state flag (SSF): extracting information on surface freeze/thaw conditions from backscatter data using an empirical threshold-analysis algorithm," *IEEE Trans. Geosci. Remote Sens.*, vol. 50, no. 7, pp. 2566–2582, 2012. 74

[60] R. Lindsley and D. Long, "Local time of day processing with ASCAT," Microwave Earth Remote Sensing Laboratory, Tech. Rep. MERS 10-01, April 2010. [Online]. Available: http://www.scp.byu.edu/docs/pdf/MERS1001.pdf 74, 78

[61] D. Long, P. Hardin, and P. Whiting, "Resolution enhancement of spaceborne scatterometer data," *IEEE Trans. Geosci. Remote Sens.*, vol. 31, no. 3, pp. 700–715, May 1993. 84

[62] B. Williams, "Signal Processing Methods for Ultra High Resolution Scatterometry," Ph.D. dissertation, Brigham Young University, 2010. 89

[63] R. Lindsley and D. Long, "Standard BYU ASCAT land/ice image products," Microwave Earth Remote Sensing Laboratory, Tech. Rep. MERS 10-02, June 2010. [Online]. Available: http://www.scp.byu.edu/docs/pdf/MERS1002.pdf 89

Appendix A

Tandem Enhanced Resolution ASCAT Processing

A.1 Introduction

The Advanced Scatterometer (ASCAT) instrument is a C-band fan-beam microwave sensor. Applications of ASCAT data include the measurement of ocean wind speeds, soil moisture content, and soil freeze/thaw conditions [44, 57, 58, 59]. ASCAT instruments are currently operational on the MetOp-A and MetOp-B satellites and provide global coverage in a near-polar orbit. The complimentary orbits of MetOp-A and MetOp-B result in different coverage patterns over each revolution. Using tandem processing, data from both ASCAT sensors (ASCAT-A and ASCAT-B) can be combined to achieve increased global coverage after fewer orbits. Potential benefits of tandem processing include increased temporal resolution of satellite imagery and improved radiometric accuracy. This appendix describes the coverage patterns of ASCAT-A and ASCAT-B, a method of tandem image processing which can capture diurnal effects, and algorithms for tandem enhanced resolution image reconstruction. The performance of different image reconstruction algorithms is summarized with results reproduced from Lindsley's analysis [50].

The paths of the ASCAT-A and ASCAT-B polar orbits result in a high number of observations located near the poles. High coverage over the poles enables observation of diurnal effects through local time of day processing [60]. Local time of day (LTD) processing creates images of the polar regions using only measurements taken from similar local times. The MetOp-B orbit trails the MetOp-A orbit by approximately 55 minutes, so temporal differences in coverage must be considered when determining how to create LTD images for each sensor and for tandem processing. Temporal boundaries on LTD processing for ASCAT-A and ASCAT-B are determined using an analysis of the local times observed over the coverage paths. Similarities between the local times observed for ASCAT-A and ASCAT-B polar coverage make LTD tandem processing feasible.

Enhanced resolution image reconstruction for tandem or single sensor images requires knowledge of the spatial response function (SRF) of the sensor. The SRF provides a spatially varying weighting function which is applied to the measured σ^0 value over the area of each measurement. Either a full or partial representation of the SRF can be used to reconstruct the image. Though use of the partial SRF can greatly reduce computational expense, using the full SRF results in lower signal and noise error in the reconstructed image [50].

The report is organized as follows: Section 2 discusses the coverage patterns of ASCAT-A and ASCAT-B, Section 3 discusses tandem SIR image processing, and LTD processing is discussed in Section 4. Section 5 describes image reconstruction using the SRF, and summarizes the performance of the full and partial SRF for image reconstruction; quan-

titative performance results are included from Lindsley's analysis of reconstruction using the full and partial SRF [50]. Section 6 concludes.

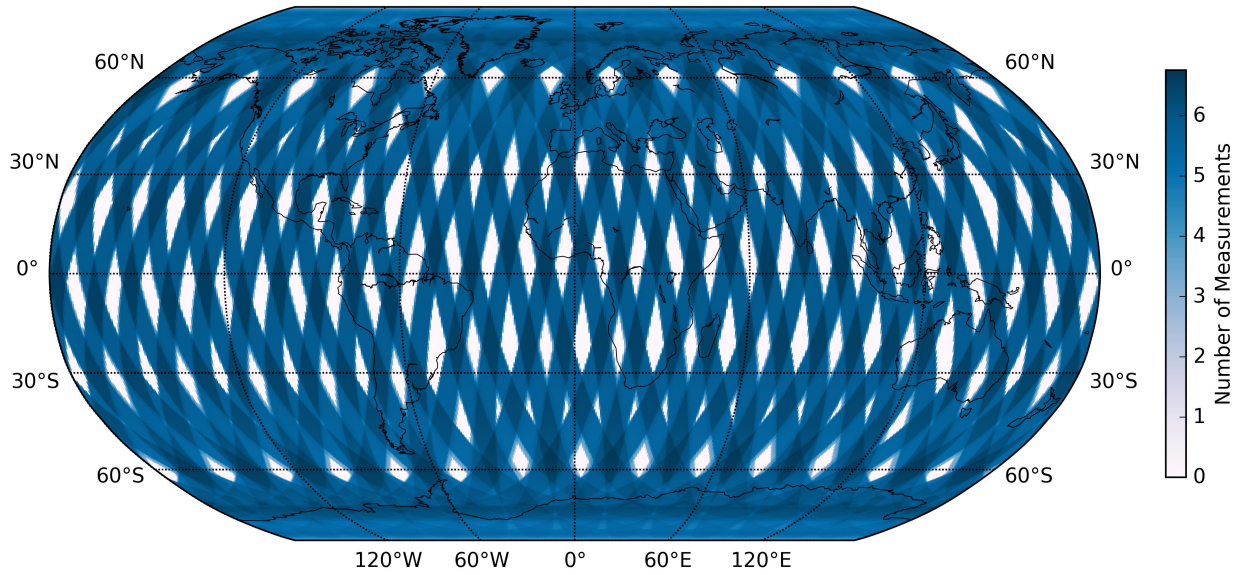

Figure A.1: Single day coverage map of ASCAT-A for January 1, 2014.

A.2 Coverage patterns

The usefulness of tandem processing of ASCAT-A and ASCAT-B is dependent on the differences in daily global coverage between the sensors. For both sensors, significant gaps in coverage area on the globe are present for a single day of data retrieval. Combining data from both sensors reduces gaps in the data. A single-day coverage map for ASCAT-A is shown in Figure A.1. Using data from both sensors, diamond-shaped gaps near the poles are filled in, and gaps closer to the equator are reduced. This is visible in Figure A.2 where data is taken from both ASCAT-A and ASCAT-B to produce a map of single-day coverage. Even after combining one-day data from both sensors, though, coverage gaps remain. Processing data for two days for both sensors gives an increase in global coverage as shown in Figure A.3. The two-day tandem coverage is greater than two-day coverage of ASCAT-A alone, which is shown in Figure A.4. Finally, Figure A.5 shows a histogram of the number of measurements reported after combining one-day coverage for both sensors on a global map. High levels of overlap occur in swaths near the poles, though there remain significant gaps in coverage from 30 degrees north latitude to 30 degrees south latitude.

Observing the coverage patterns of the ASCAT-A and ASCAT-B sensors reveals that tandem processing would improve σ^0 images produced at single and multi-day temporal resolution and could potentially improve LTD images. Single day images would show the most improvement in polar regions, where coverage gaps are removed after a single day of

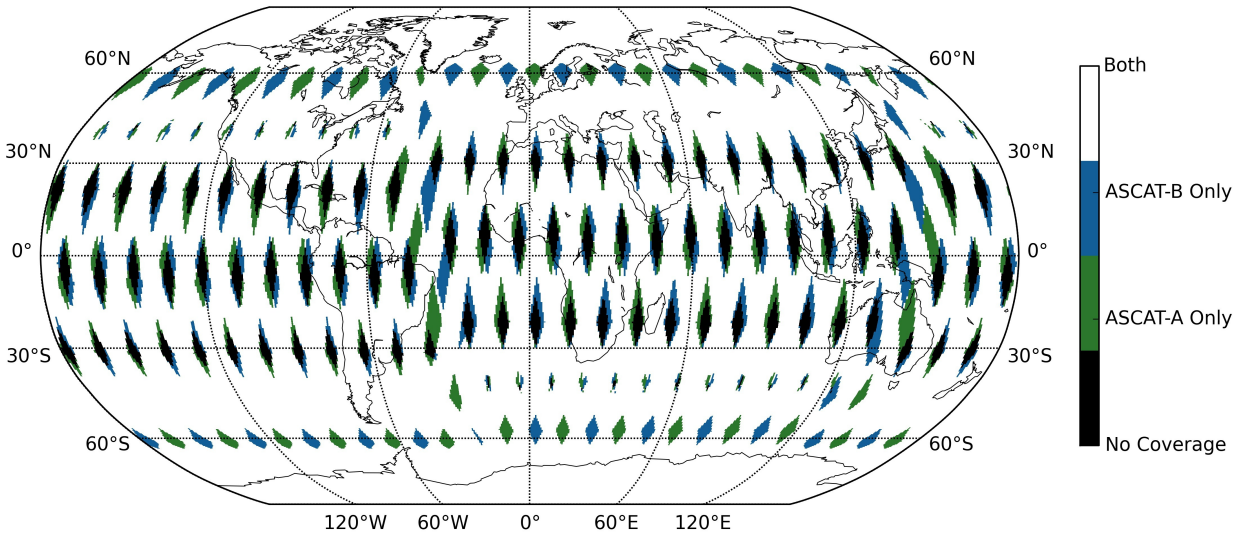

Figure A.2: Single day coverage map which combines ASCAT-A and ASCAT-B data for January 1, 2014.

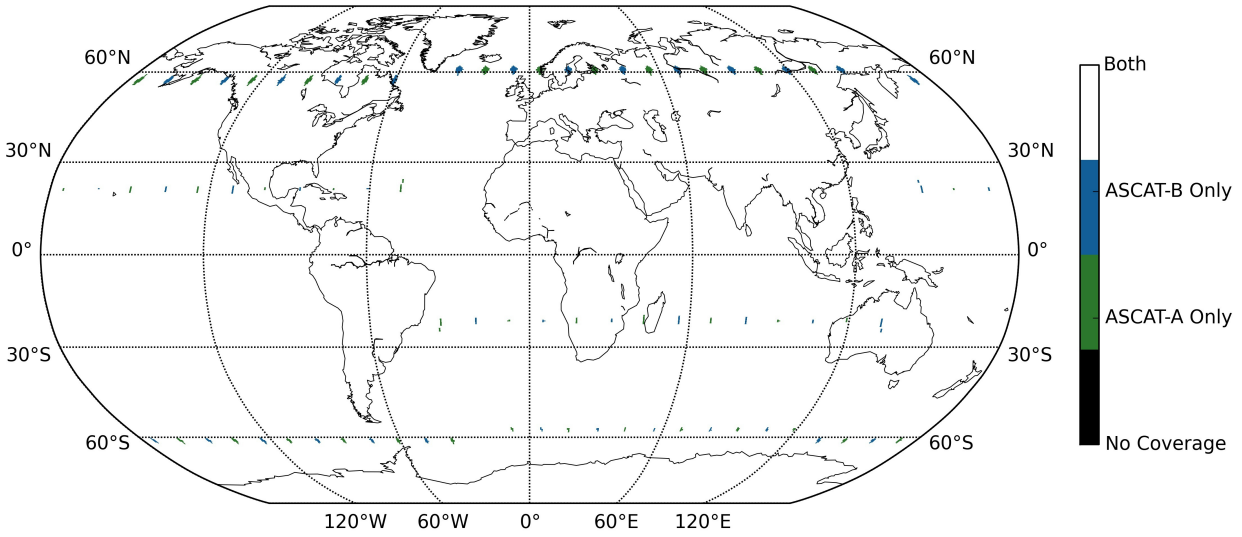

Figure A.3: Two-day coverage map combining data from ASCAT-A and ASCAT-B for January 1 to January 2, 2014.

measurements. High resolution images of other regions of the globe would likely be improved after two or more days of measurements, after which most mid-latitude coverage gaps are eliminated. LTD tandem images over the poles can be produced, though the timing of the ASCAT-A and ASCAT-B orbits must be analyzed (below) to ensure that measurement local times occur within a similar time frame for both sensors.

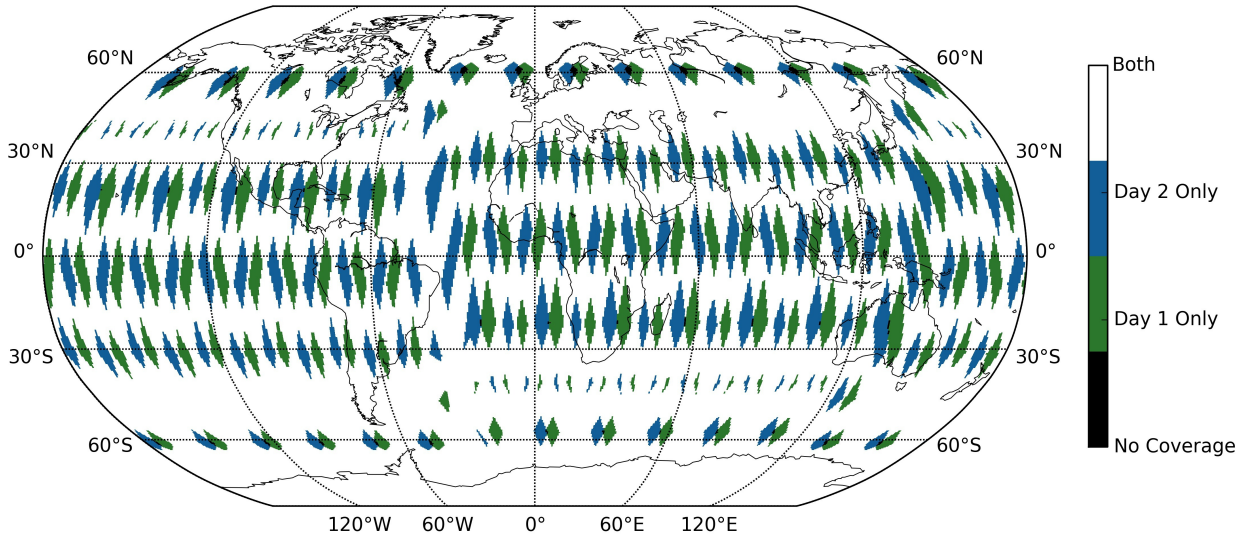

Figure A.4: Two-day coverage map for ASCAT-A from January 1 to January 2, 2014.

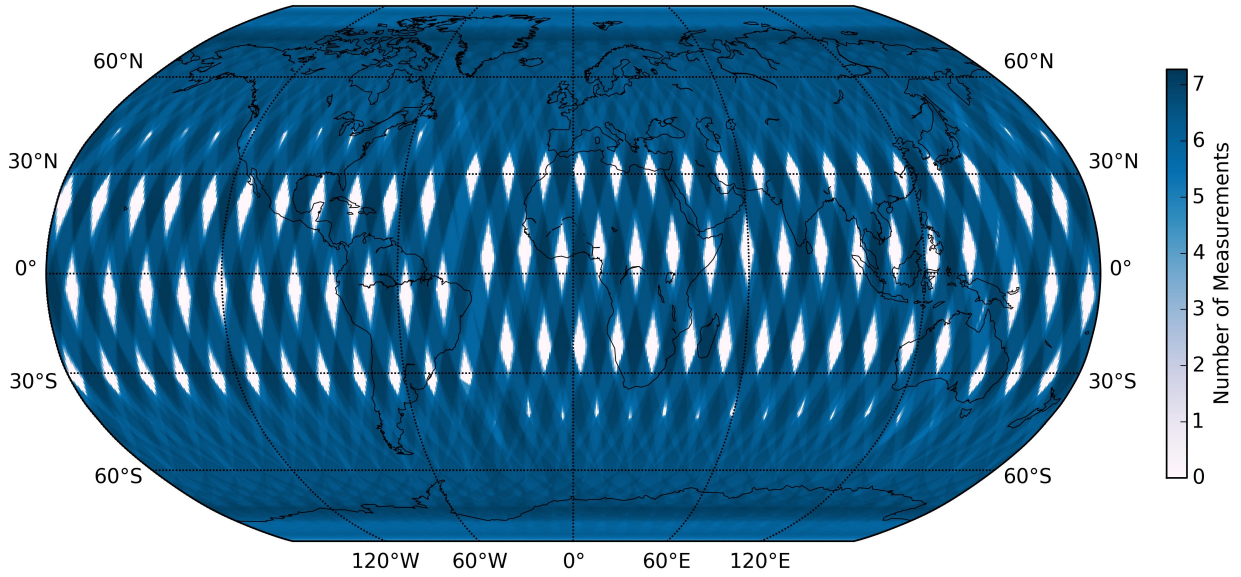

Figure A.5: Single day coverage histogram of ASCAT-A and ASCAT-B for January 1, 2014. The histogram shows the number of reported measurements across the globe.

A.3 Local Time of Day Processing

Local time of day processing combines polar σ^0 measurements within certain time divisions to create images with a smaller time variance than is achieved when measurements are combined over all 24 hours. LTD processing enables observation of diurnal events, which are obscured when images are created using measurements taken over the course of an entire day in local time. For the ASCAT-A sensor, optimal LTD measurement time divisions have

been determined [60]. Selecting only measurements which fall into these time divisions results in a loss of spatial coverage, so multi-day LTD images are also produced which demonstrate fewer coverage gaps.

The local time for any measurement can be found using the longitude and UTC time at which the measurement was taken. The derivation of the local time from these parameters is shown in Eqn. A.1.

$$\text{Local Time [minutes]} = \text{UTC [minutes]} + 4\left[\frac{\text{minutes}}{\text{degree}}\right] * \text{longitude [degrees]} \qquad \text{(A.1)}$$

Time divisions for ASCAT-A LTD processing are shown in Table A.1. These divisions are validated by analyzing the local times of retrieved data over selected areas in the Northern and Southern Hemispheres [60]. A comparison of the measurement local times for ASCAT-A and ASCAT-B shows that the same local time divisions used for ASCAT-A can be applied with good result to create ASCAT-B LTD images.

To determine the LTD divisions, measurements are analyzed within a strip in the Northern and Southern Hemisphere which is narrow in latitude and wide in longitude. In the Northern Hemisphere the region is defined by 82° to 83° N latitude and -80° W to 100° E longitude. The region in the Southern Hemisphere is defined by -82° to -83° S latitude and -80° W to 100° E longitude. Normalized histograms of measurements versus local time are shown in Figs. A.6 and A.7. Southern Hemisphere histograms are shown in Figs. A.8 and A.9. The lines in the figures delineate the LTD divisions as listed in Table A.1. For both ASCAT-A and ASCAT-B, the lines appear to be located in the center of the space between the bimodal distributions. The result is that two images can be produced with each one being made up of measurements coming from one of the LTD divisions. It is also noted that the ASCAT-A LTD divisions can be applied without change to ASCAT-B for LTD processing. These divisions can also be used for tandem LTD processing.

Table A.1: The ASCAT-A LTD window definition for regions in the Northern and Southern Hemispheres

NHe	7:30a-3:30p mnfa	3:30p-11:30p mefa
SHe	3:30a-11:30a mmfa	7:30p-3:30a mefa

A.4 SIR Image Comparison

A comparison of images of the Antarctic generated using ASCAT-A and ASCAT-B is done to illustrate the usefulness of tandem processing and to explore differences between taking an average of ASCAT-A and ASCAT-B SIR images and producing new images by applying the SIR algorithm directly to ASCAT-A and ASCAT-B data. The individual images of the Antarctic for day of year (DOY) 60 to 61 are shown for ASCAT-A and ASCAT-B in

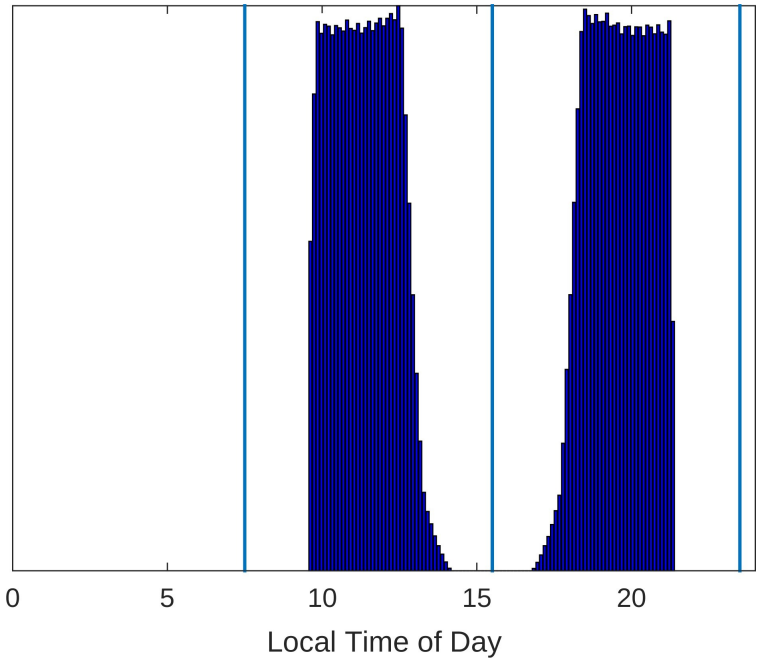

Figure A.6: Normalized histogram showing ASCAT-A measurements and local time of day over the Arctic from April 20-30, 2013. Measurements are taken from 82° to 83° N latitude and from -80° W to 100° E longitude.

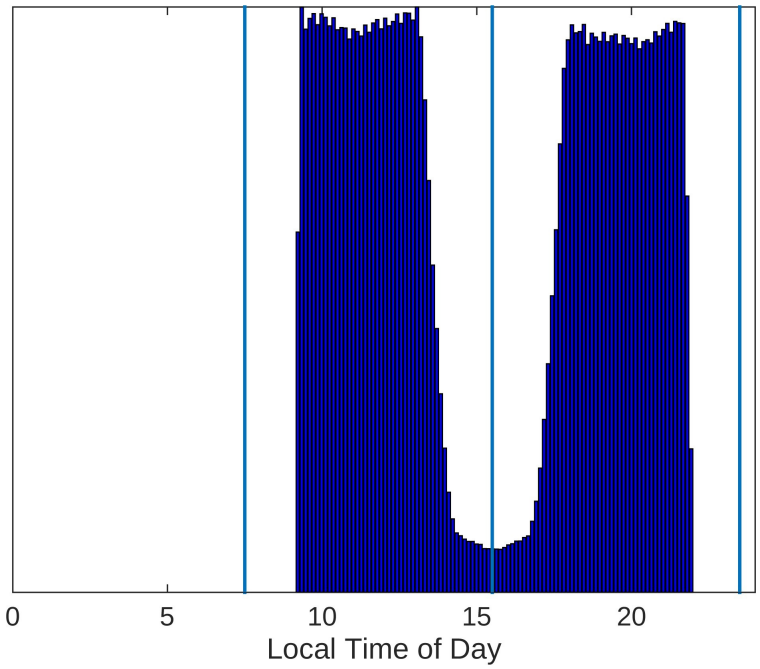

Figure A.7: Normalized histogram showing ASCAT-B measurements and local time of day over the Arctic from April 20-30, 2013. Measurements are taken from 82° to 83° N latitude and from -80° W to 100° E longitude.

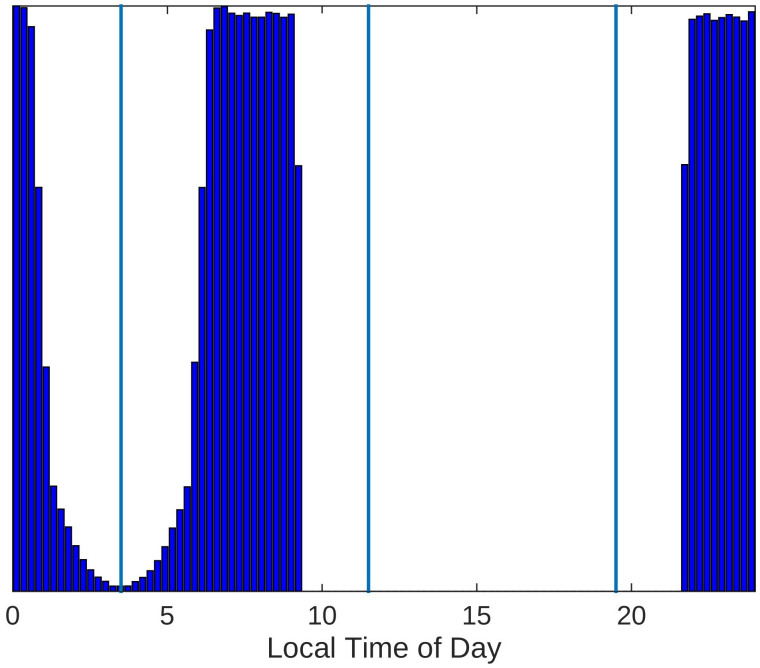

Figure A.8: Normalized histogram showing ASCAT-A measurements and local time of day over the Antarctic from April 20-30, 2013. Measurements are taken from -82° to -83° S latitude and from -80° W to 100° E longitude.

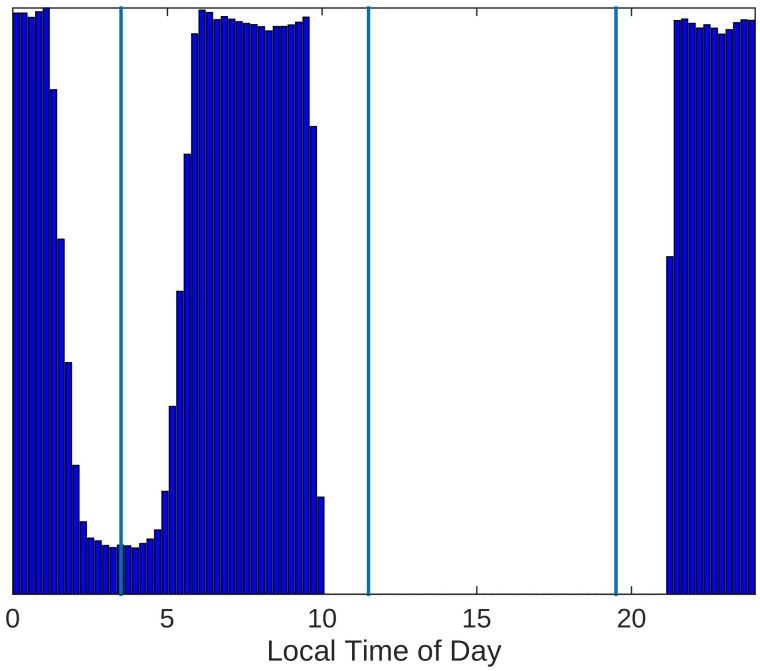

Figure A.9: Normalized histogram showing ASCAT-B measurements and local time of day over the Antarctic from April 20-30, 2013. Measurements are taken from -82° to -83° S latitude and from -80° W to 100° E longitude.

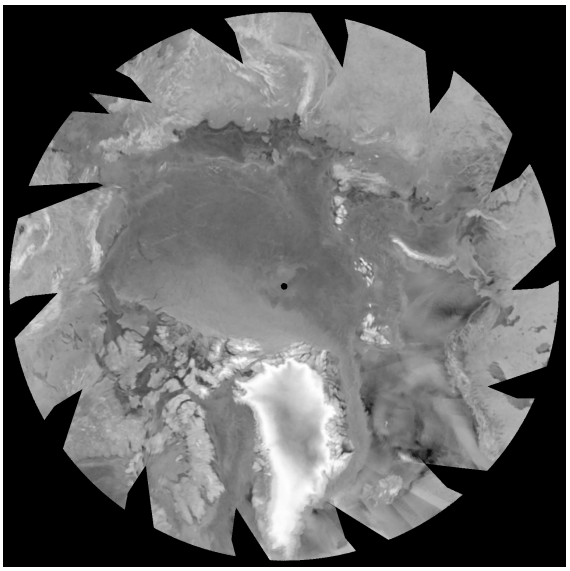

Figure A.10: LTD Evening ASCAT-A image for April 21-24, 2013.

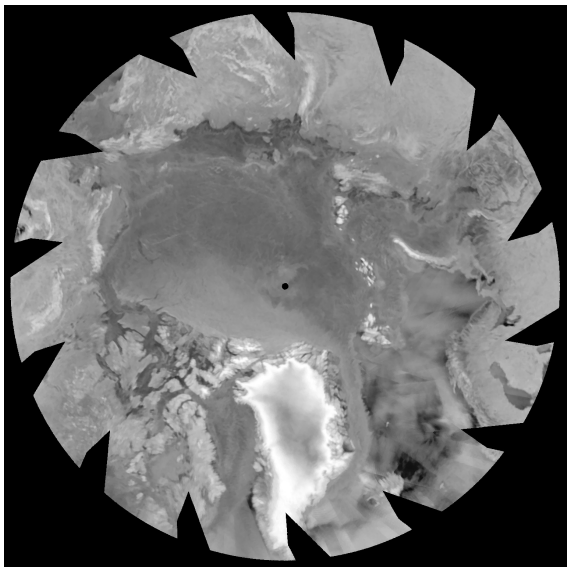

Figure A.11: LTD Evening ASCAT-B image for April 21-24, 2013.

Figures A.12 and A.13 respectively. Both of these images have diamond-shaped gaps in the data caused by incomplete orbital coverage of the imaged area.

Taking an average of the 2-day images of ASCAT-A and ASCAT-B eliminates the gaps in coverage and produces a complete image of the Antarctic, as shown in Figure A.14. Likewise, applying the SIR algorithm to data from the same 2-day period from both ASCAT-A and ASCAT-B produces an image with complete coverage over the Antarctic region (Figure A.15. The SIR processing in this case, however, achieves a better σ^0 slope estimate and so, upon visual inspection, the reconstructed image appears clearer.

The visible improvement in the images produced by applying the SIR algorithm directly to both ASCAT-A and ASCAT-B data rather than averaging 2-day SIR images displays the usefulness of the processing ASCAT-A and ASCAT-B polar images in tandem.

The usefulness of tandem processing can further be noted by inspecting images produced with one day of tandem data. One day of data from ASCAT-A and ASCAT-B enables the creation of Arctic and Antarctic images with no significant coverage gaps. Example Antarctic and Arctic tandem-processed images for DOY 65, 2013 are shown in Figures A.16 and A.17.

A.5 Spatial Response Function

Measured σ^0 values reported by the ASCAT sensors are calculated by observing the backscattered power from the area illuminated by an antenna. The contribution to the measured value of σ^0 from any given section of the illuminated area is non-uniform and can be represented using a spatial response function (SRF). A model for the measured values of

σ^0 observed by the ASCAT sensors is given by

$$\sigma^0_{meas} = \int \sigma^0(x,y)h(x,y)dxdy, \tag{A.2}$$

where $h(x,y)$ represents the SRF.

The SRF can be used to approximately reconstruct the truth values of σ^0 by inverting Eqn. 2. As a result, enhanced resolution images of σ^0 can be reconstructed. Either a fully-modeled SRF or a less accurate, but less computationally intensive, 3 dB-windowed SRF can be used during the image reconstruction process [50].

There are tradeoffs for using an approximate SRF to reconstruct the enhanced resolution image. The full-valued SRF is shown in Fig. A.18. It is evaluated to provide a tapered, quantized weighting between 0 and 1 for pixels falling in each measurement area. The weighting applied to each pixel is determined by evaluating the SRF at the location of the pixel center. The binary-valued SRF assigns a spatial response weighting of 1 to the pixel if SRF is greater than -3 dB at the location of the pixel center. Otherwise, the spatial response weighting becomes 0 and the pixel is not affected by that measurement. Differences in the SRFs result in slightly different reported σ^0 values in the reconstructed images.

The full-valued SRF provides a closer approximation to the actual SRF than the binary-valued SRF and produces images with decreased signal and noise error when used with the SIR algorithm. Before SIR is used to iteratively reconstruct the image, an AVE image is produced. The value of a pixel in the AVE image is determined by first identifying all measurements with a corresponding SRF of non-zero value at the pixel. A weighted average of all such measurements is used to determine the pixel value; weights are determined by the SRF values of the measurements at the pixel location. The SIR algorithm uses the AVE image to determine correction factors which are applied to create a new image with reduced

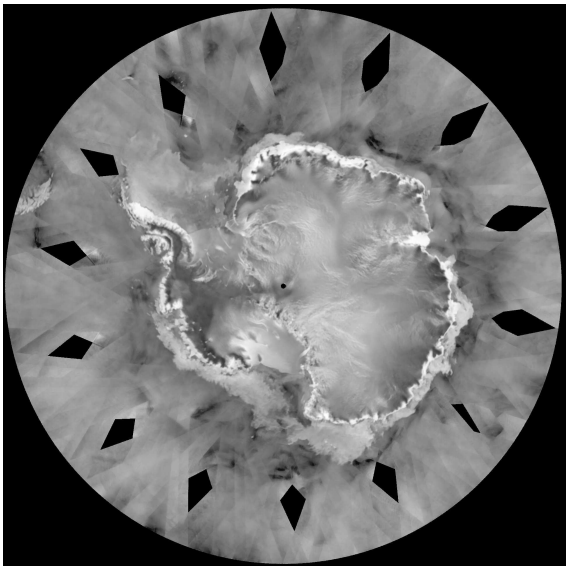

Figure A.12: 2-day Antarctic ASCAT-A image (DOY 60 to 61, 2013)

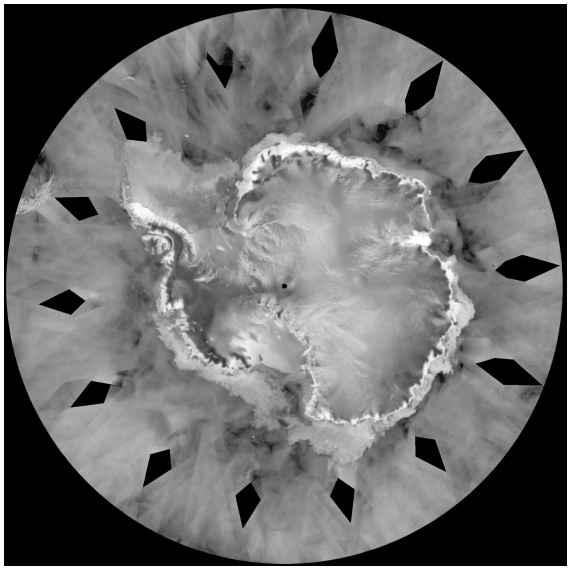

Figure A.13: 2-day Antarctic ASCAT-B image (DOY 60 to 61, 2013)

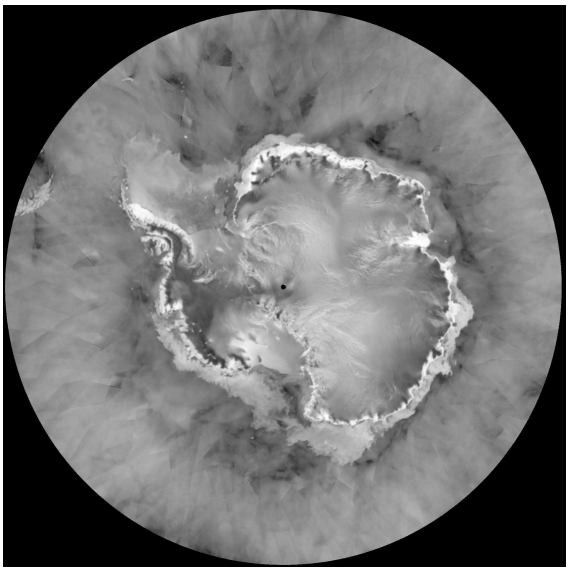

Figure A.14: 2-day Antarctic image created by taking an average of ASCAT-A and ASCAT-B SIR images for DOY 60 to 61, 2013

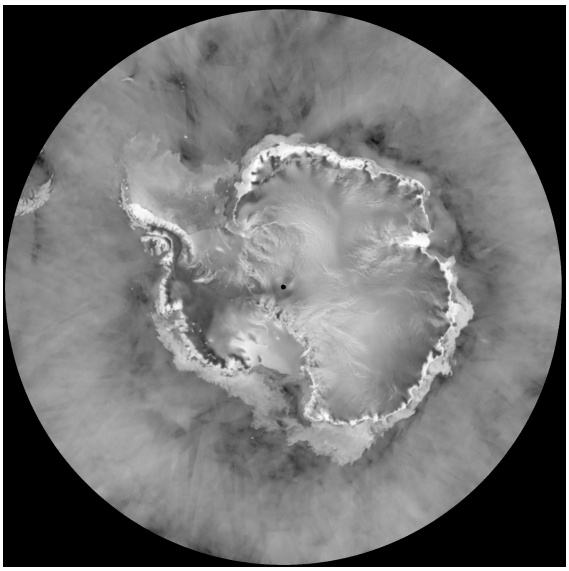

Figure A.15: 2-day Antarctic image created through use of the SIR algorithm on ASCAT-A and ASCAT-B data for DOY 60 to 61, 2013

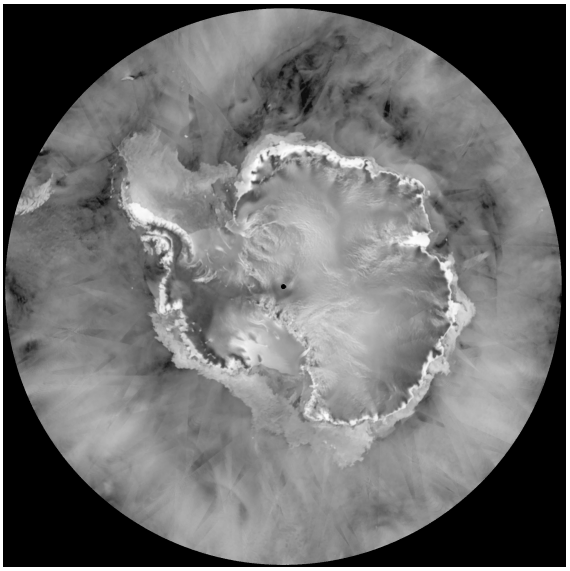

Figure A.16: 1-day Antarctic image created through use of the SIR algorithm on ASCAT-A and ASCAT-B data for DOY 65, 2013

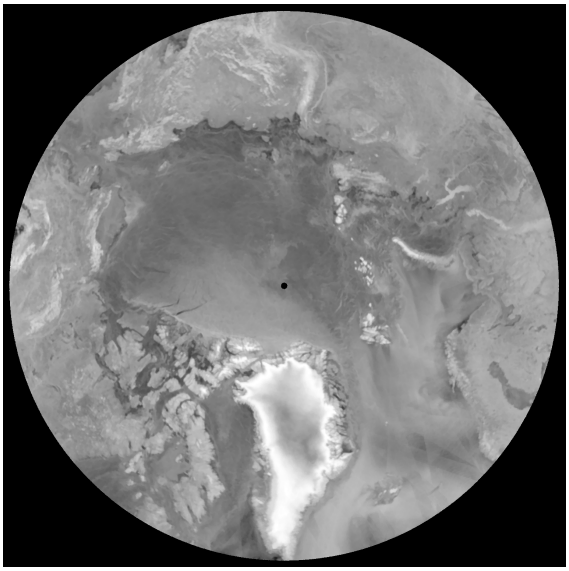

Figure A.17: 1-day Arctic image created through use of the SIR algorithm on ASCAT-A and ASCAT-B data for DOY 65, 2013

signal noise. The process of calculating and applying correction factors is iterative and ideally results in images which better approximate a truth image after successive iterations.

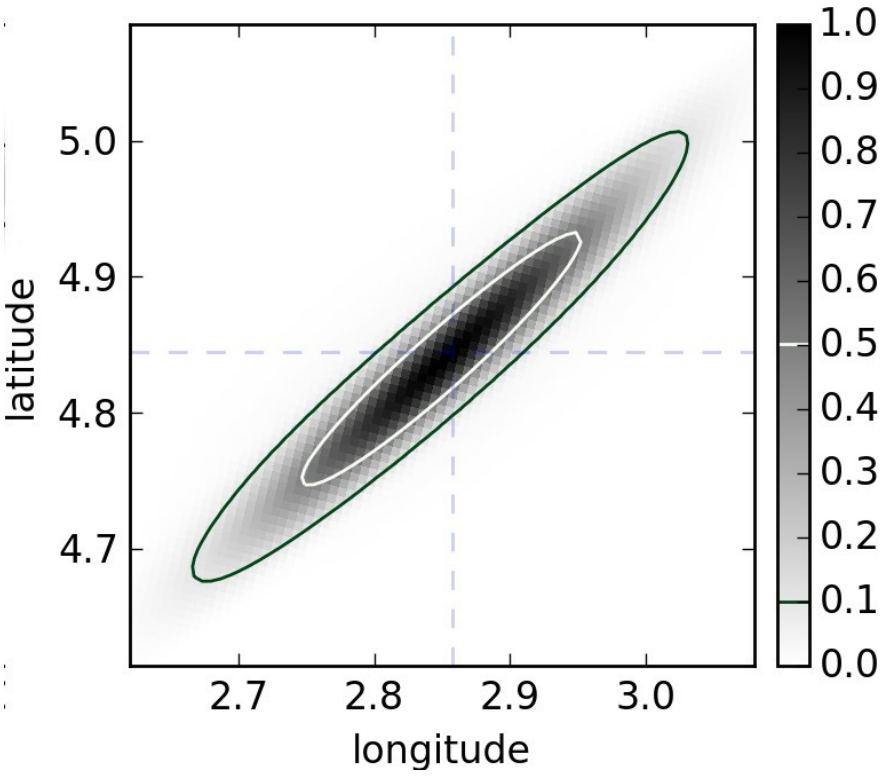

Figure A.18: ASCAT spatial response function for a left mid beam measurement. Reproduced from [50].

The SIR algorithm is an adapted form of multiplicative algebraic reconstruction which ideally converges to a point where the iterative image correction factors become unity [61]. Unfortunately noisy scatterometer measurements result in the introduction of increasing levels of noise error with increased iterations of the SIR algorithm. The non-convergence of the image reconstruction process has led to an adapted implementation of the SIR algorithm which specifies the number of iterations to reduce noise error (typically around 30) [19]. Image reconstruction using the SIR algorithm with the full-valued SRF is more computationally intensive than using the binary-valued SRF, but results in reduced noise and signal error.

A.5.1 Image Comparison

Although the binary-valued SRF enables image reconstruction with less computation, the resulting images differ slightly from those produced with the full-valued SRF. Differences in reported σ^0 values are especially apparent in areas of geographical transition, including coastlines and ice edge boundaries. The full-valued SRF also appears to demonstrate marginally sharper features than the binary-valued SRF. The difference in feature sharpness can be observed by comparing Figs. A.19 and A.20, which show reported σ^0 values from Southern England. Figs. A.21, A.22, and A.23 show the difference in reported σ^0 values between images produced with the binary-valued and full-valued SRF. The standard deviation

of σ^0 in the difference images ranges from approximately 0.14 to 0.18 dB. Most values show a difference of less than 0.5 dB, though more extreme differences occur near coastlines and other natural borders.

A close inspection of the difference images also reveals that many of the difference features are SRF-shaped. The binary-valued SRF has a binary weighting of 1 or 0 and leaves an egg-shaped edge around measurement areas when compared against the tapered full-valued SRF.

A.5.2 Error Analysis

The performance of the two SRF models is evaluated by Lindsley [50] using simulation (where the true image is known). A synthetic image is created and reconstructed using the SIR algorithm and ASCAT sampling geometry to determine the relative noise properties of image reconstruction with the full-valued or binary-valued SRF. A noiseless and noise-injected version of the synthetic image are used to analyze the signal and noise error of the reconstruction process. The noiseless synthetic image is shown in Fig. A.25 [50]. The amount of signal and noise error for each iteration of reconstruction is shown in Fig. A.26 [50]. The figure shows that successive iterations of the SIR algorithm initially reduce signal noise but ultimately introduce increasing levels of noise error as the number of iterations exceeds an optimal amount. Image reconstruction using the full-valued SRF demonstrates decreased levels of both noise and signal error compared to images reconstructed using the binary-valued SRF after approximately three iterations. The figure also shows the signal and noise errors for the AVE images and images produced using a traditional gridding (GRD), or drop-in-the-bucket, approach at two different pixel sizes. Note that the averaging used in the GRD method results in low noise error, but also results in high signal error because of the course resolution of the resulting image.

The signal error in the reconstructed image is calculated by taking the standard deviation of the difference between the noiseless reconstructed image and the truth image. The noise error is computed by taking the root square difference of the signal errors for the noisy and noiseless reconstructed images.

Using the full-valued SRF results in much lower levels of signal error in the reconstructed image when compared to results from the binary-valued SRF. Despite its computational expense, using the full-valued SRF for image reconstruction is the preferred method of reconstructing the high resolution images of σ^0.

A.6 Conclusion

Examining the coverage patterns of the ASCAT-A and ASCAT-B sensors suggests that tandem processing can be used to create images of the poles with 1-day temporal resolution. Although complete coverage of the earth is nearly achieved with both sensors over a 2-day span, approximately the same coverage is achieved with a single sensor over 2 days. Actual images produced using tandem processing of ASCAT-A and ASCAT-B 1-day and 2-day images confirm that polar coverage is achieved without significant gaps in the data. Direct tandem processing using the SIR algorithm on ASCAT-A and ASCAT-B data produces a clearer image than simple averaging of ASCAT-A and ASCAT-B SIR images and is recommended for creation of ASCAT tandem σ^0 images. LTD images can also

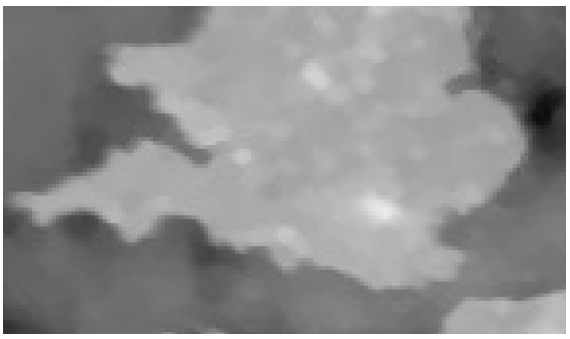

Figure A.19: Full-valued SRF σ^0(dB) image of Southern England produced from DOY 109-113, 2013.

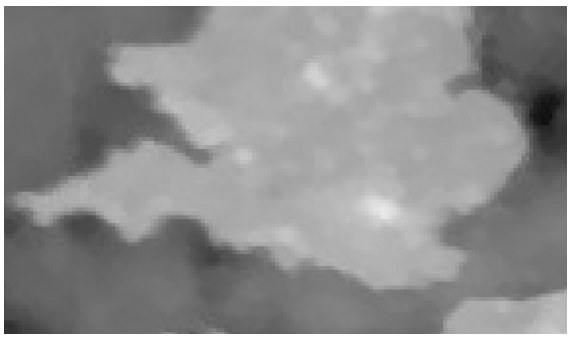

Figure A.20: Binary-valued SRF σ^0(dB) image of Southern England produced from DOY 109-113, 2013.

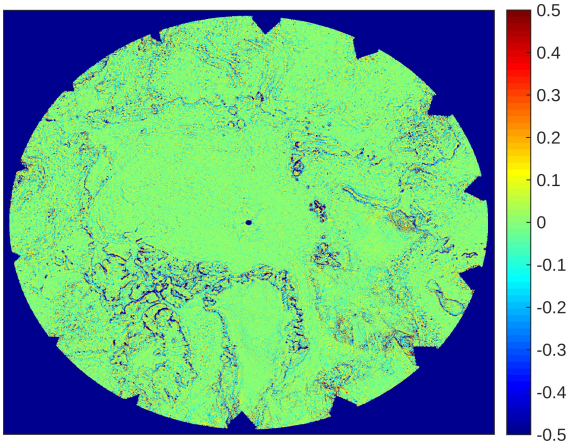

Figure A.21: Full-valued/binary-valued SRF σ^0(dB) difference image of the Arctic produced from DOY 112-113, 2013.

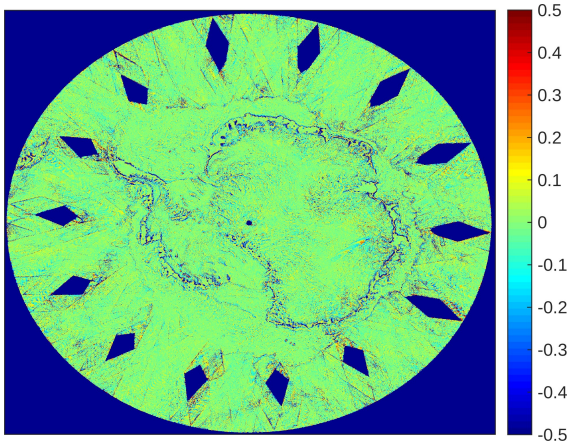

Figure A.22: Full-valued/binary-valued SRF σ^0(dB) difference image of the Antarctic produced from DOY 112-113, 2013.

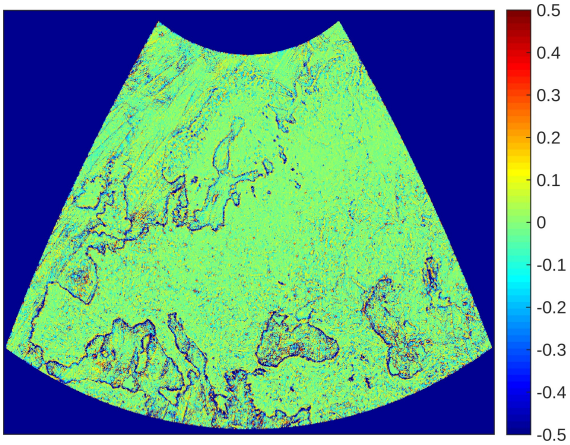

Figure A.23: Full-valued/binary-valued SRF σ^0(dB) difference image of Europe produced from DOY 109-113, 2013.

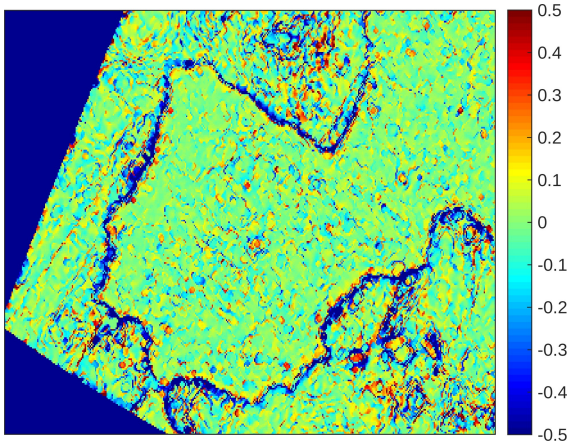

Figure A.24: Full-valued/Binary-valued SRF σ^0(dB) difference image of Spain produced from DOY 109-113, 2013.

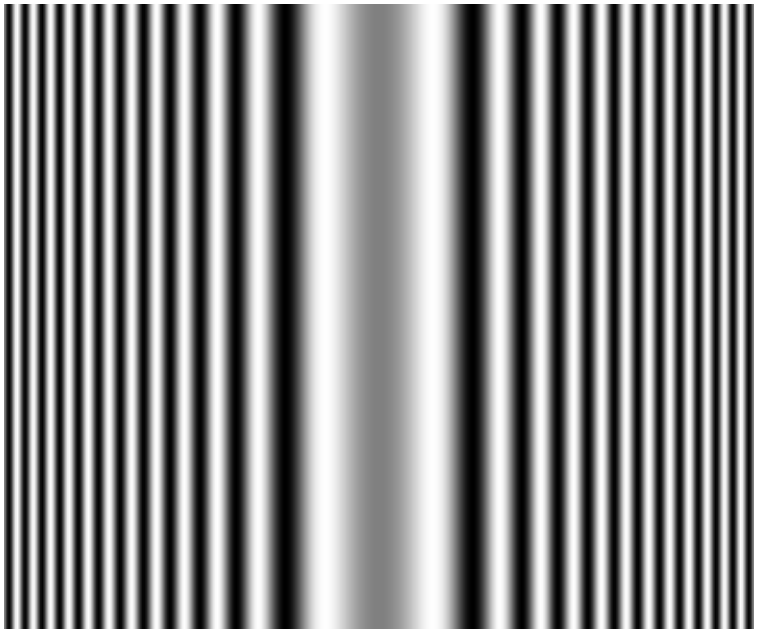

Figure A.25: Horizontal chirp synthetic image used to test SRF image reconstruction. Reproduced from [50].

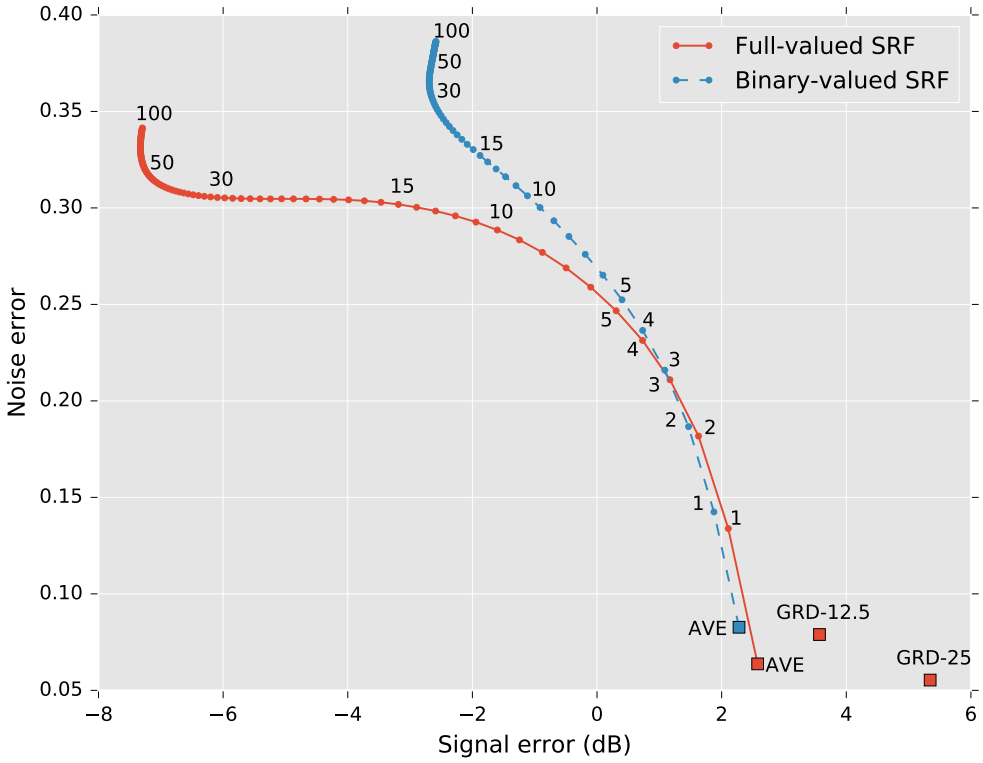

Figure A.26: Plot of noise error versus signal error for a synthetic chirp image reconstructed using the full-valued and binary-valued SRF. Performances of various reconstruction algorithms are shown, including SIR, AVE, and GRD. Reproduced from [50].

be produced in tandem without adjustment to LTD divisions which have been applied to ASCAT-A. Tandem LTD processing can reduce coverage gaps visible in single-sensor LTD images. Although both the full-valued and binary-valued SRF can be used to create high resolution images of σ^0 using the SIR algorithm, the full-valued SRF is preferred because of the decreased signal and noise error properties of the output image.

Appendix B

ASCAT Browse Images

B.1 Introduction

Enhanced resolution images of σ^0 at C-band are produced using data from ASCAT and publicly disseminated through the Scatterometer Climate Record Pathfinder (SCP) [30]. Separate images are available for all continents and the Arctic and are produced by combining ASCAT data from two, four, or five days, which is the required amount of time for the sensor to sample the imaged regions without significant gaps in coverage. Here, daily ASCAT σ^0 browse images are described which display the entire globe, the Arctic, and the Antarctic at low resolution. Images capturing data from ascending, descending, and both passes are processed for the entire globe, while images of the poles use all passes to reduce coverage gaps. The data are made available on the SCP and are intended to complement the ASCAT high-resolution dataset.

B.2 ASCAT Browse Image Reconstruction

A drop-in-the-bucket gridding approach is selected for processing the ASCAT σ^0 browse images [62]. This approach conforms with previous processing techniques used to create the Oceansat-2 scatterometer σ^0 browse product and is less computationally expensive than high-resolution image reconstruction techniques, including SIR or AVE [19].

The images are produced by defining a latitude and longitude grid of 0.2 deg/pixel in a rectangular map projection for the global images, and a grid of 22.25 km/pixel in a polar stereographic projection for the Northern and Southern Hemisphere images. All measurements falling into each grid cell over a day of coverage are averaged to produce an image.

Due to the fan beam geometry of the ASCAT sensor, σ^0 observations occur at different incidence angles across the measurement swaths of each antenna. The difference in incidence angle results in a bias of σ^0 across the swath and undesirable artifacts in the reconstructed images. Measurements from areas near the edge of the swath typically occur at extreme incidence angles and are responsible introduce many of the artifacts. To correct for the incidence angle dependency of the σ^0 values, a linear relationship between incidence angle and σ^0 is assumed, and σ^0 values are corrected to a nominal incidence angle (40 degrees). The enhanced-resolution ASCAT products undergo a similar normalization process [63].

The σ^0 values are normalized to a nominal incidence angle of 40 degrees using the equation

$$\sigma_n^0 = A - B(\theta - 40^\circ), \tag{B.1}$$

where σ_n^0 is the normalized σ^0 measurement, A is the reported σ^0 measurement at some incidence angle, and B is an estimate of the slope of σ^0 versus incidence angle. The value of B is estimated by fitting a least-squares regression line to all recorded values of σ^0 and the corresponding incidence angle measurements. Since the relationship between σ^0 and incidence angle is roughly linear, the slope of the regression line provides an adequate estimate for B. In pixel areas where only one σ^0 measurement is recorded or where there is not enough variation in incidence angle to calculate B, a subjectively selected value is used for B. In such cases, values of B are chosen for areas over land and water which visually appear to minimize artifacts in the browse images.

B.3 Region Definitions

The σ^0 browse images are produced for 5 different regions. The regions and their properties are shown in Tables B.1 and B.2. All global images are processed for a rectangular map projection and the Northern and Southern Hemisphere images are processed for a stereographic projection. Images processed using a local-time-of-day technique, which increases the temporal resolution, contain significant coverage gaps and so are not processed as part of the collection of σ^0 browse images.

Table B.1: ASCAT σ^0 Browse Global Region Definitions

Region Name	Projection	Lon, Lat Scale (pix/deg)	Size
Global Ascending	Rectangular	5, 5	1800x1900
Global Descending	Rectangular	5, 5	1800x1900
Global (Both Passes)	Rectangular	5, 5	1800x1900

Table B.2: ASCAT σ^0 Browse Polar Region Definitions

Region Name	Projection	X,Y Scales (km/pix)	Size
North Hemisphere (All Passes)	Polar Stereographic	22.25, 22.25	388x388
South Hemisphere (All Passes)	Polar Stereographic	22.25, 22.25	388x388

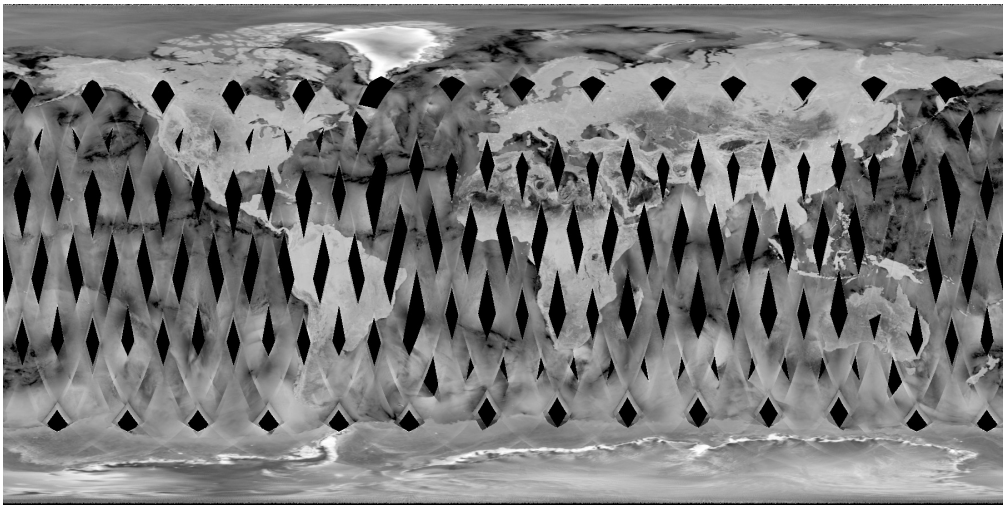

Figure B.1: Global image incorporating all passes for DOY 200, 2013.

B.4 Sample Images

A collection of sample σ^0 browse images for day of year 200 of 2013 are shown in Figs. B.1,B.2,B.3,B.4, and B.5. Included are the ascending, descending, and all-pass global browse images as well as the Northern and Southern Hemisphere images. Although some coverage gaps exist for the global all-pass image, main features of the globe are visible, including large mountain ranges and the polar ice sheets. The ascending and descending images provide less coverage, but do not contain the artifacts visible in the all-pass image where the ascending and descending passes overlap. The Northern and Southern Hemisphere images also contain some diamond-shaped coverage gaps, though most areas at extreme latitudes are pictured. In all images, few measurements are recorded for areas near the gaps in coverage. The low number of measurements results in a poor B value estimate and so pixel values may appear to be skewed compared to surrounding areas.

B.5 Conclusion

Daily images of the globe and Northern and Southern Hemisphere regions are created using ASCAT data and a drop-in-the-bucket image reconstruction method. Intended for browsing purposes, these images are lower resolution, and some contain areas with significant coverage gaps. The collection of daily images processed with this method complements the data record of images produced using the SIR algorithm with two, four, and five day temporal resolution. The images are made available online through the Scatterometer Climate Record Pathfinder [30].

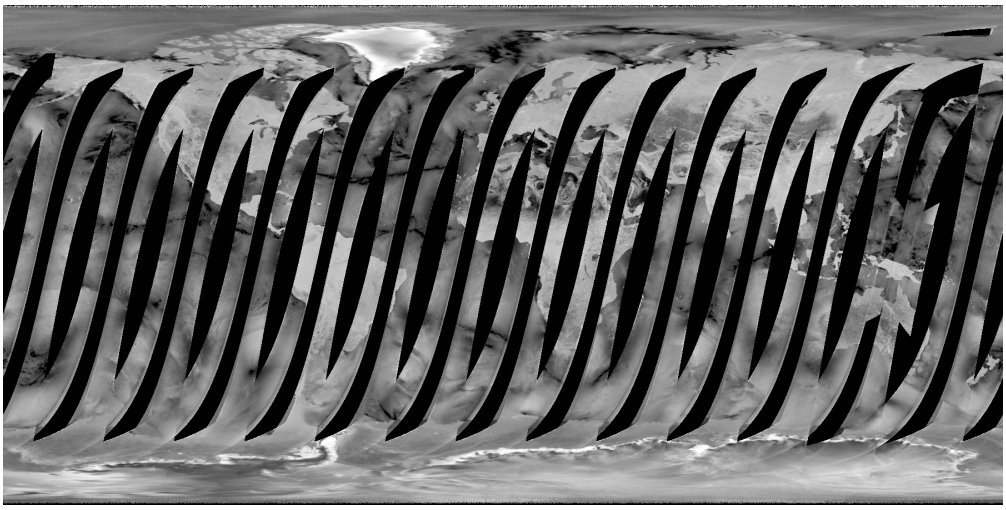

Figure B.2: Global image incorporating ascending passes for DOY 200, 2013.

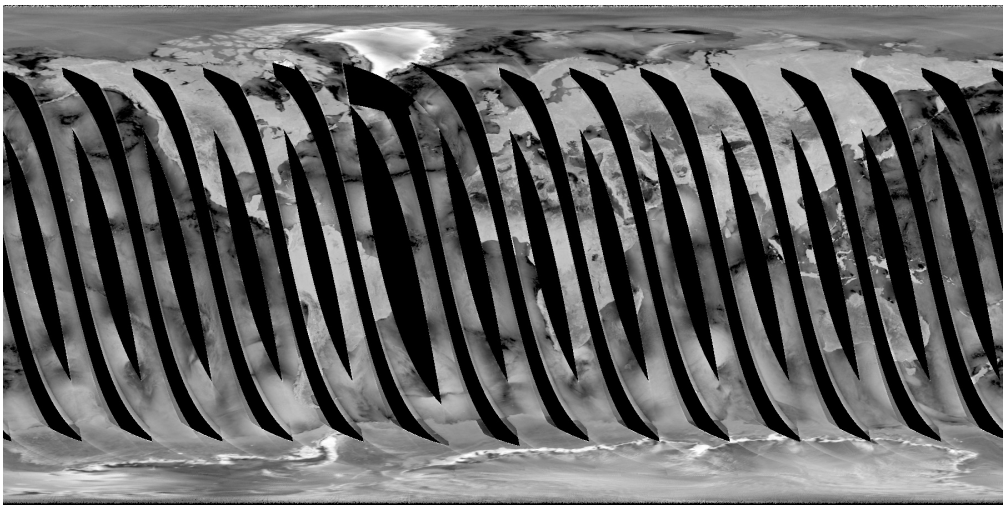

Figure B.3: Global image incorporating descending passes for DOY 200, 2013.

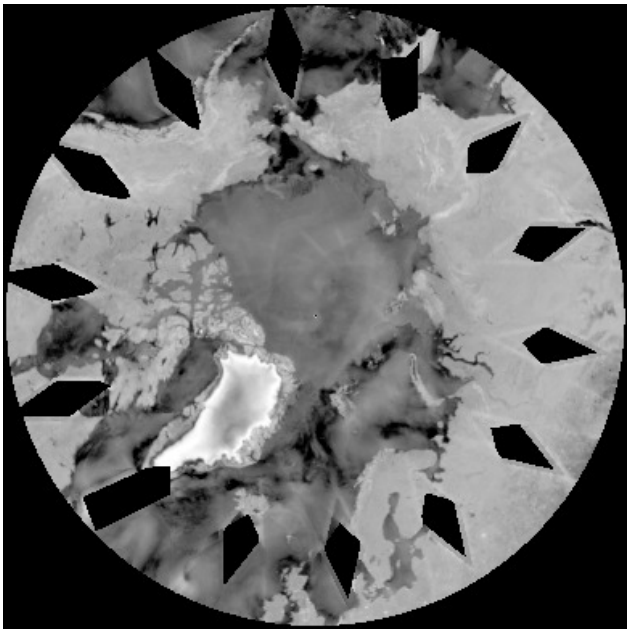

Figure B.4: Northern Hemisphere image incorporating all passes for DOY 200, 2013.

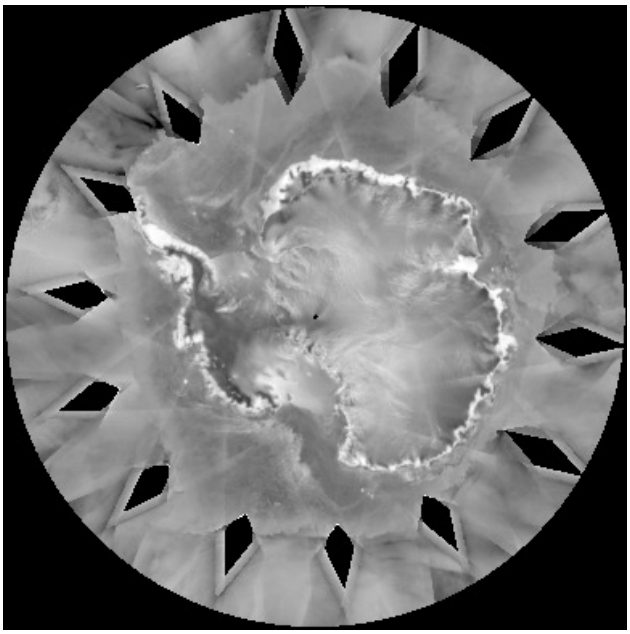

Figure B.5: Southern Hemisphere image incorporating all passes for DOY 200, 2013.